UNIVERSITAT DE BARCELONA

Modeling and observations of relativistic outflows in high-energy binary systems

Edgar Molina Lumbreras

TESI DOCTORAL

MODELING AND OBSERVATIONS OF RELATIVISTIC OUTFLOWS IN HIGH-ENERGY BINARY SYSTEMS

EDGAR MOLINA LUMBRERAS

DIRECTORS
Dr. Valentí Bosch i Ramon
Dr. Marc Ribó Gomis

Universitat de
BARCELONA

Modeling and observations of relativistic outflows in high-energy binary systems

Memòria presentada per optar al grau de
doctor per la Universitat de Barcelona

Programa de doctorat en Física

AUTOR
Edgar Molina Lumbreras

DIRECTORS
Dr. Valentí Bosch i Ramon
Dr. Marc Ribó Gomis

TUTOR
Dr. Alberto Manrique Oliva

DEPARTAMENT DE FÍSICA QUÀNTICA I ASTROFÍSICA
Barcelona, 21 Juny 2021

UNIVERSITAT DE
BARCELONA

DECLARATION

This thesis is presented following the regulations of the University of Barcelona (Approved by the CdG in the session of 16 March 2012 and modified by the CdG on 9 May and 19 July 2012, 29 May and 3 October 2013, 17 July of 2014, 16 July 2015, 15 June and 21 November 2016, 5 December 2017, 4 May 2018, 15 May and 22 July 2019, and 7 of October 2020). The listed regulations allow for the presentation of a PhD thesis as a compendium of published articles. According to the regulations, the thesis must contain a minimum of three published or accepted articles. This thesis contains the published version of three articles, which is sufficient to allow its presentation.

Barcelona, 21 Juny 2021

Edgar Molina Lumbreras

ACKNOWLEDGMENTS

Primer de tot vull agrair als meus directors, els Drs. Valentí Bosch i Marc Ribó, la seva guia i ajuda durant aquests últims anys. Pot sonar a clixé, però em sento molt afortunat d'haver realitzat la meva tesi sota la seva supervisió, no només des d'un punt de vista científic, sinó també personal. Faig extensiu el meu agraïment a tot el grup d'altes energies de la UB, en el que m'he sentit molt ben acollit. Gràcies Josep Maria, Pol, Kazushi, Matteo. Una menció especial va per al JR i la seva màgia a l'hora de solucionar els tràmits burocràtics, o en general qualsevol cosa que afecti el departament.

Quiero agradecer a los Dres. Gustavo Romero y Santiago del Palacio por su hospitalidad durante mi estancia en el IAR. Fueron 2 meses en los que aprendí mucho, y además pude conocer de buena mano la vida en un país como Argentina. Me quedan muy buenos recuerdos de esa estancia, y una afición por el mate que aún perdura. També vull agrair el Dr. Manel Perucho per fer-me sentir molt a gust durant la meva estada a València, tot i que ens guanyéssiu la final de Copa i jo no sabés on ficar-me amb tant valencianista pels voltants.

I would also like to thank Dr. Jean-Pierre Ernenwein, Dr. Denys Malyshev and Sebastien Le Stum for performing some data analyses and producing a plot for a chapter of this thesis, and kindly allowing me to use them. Considering that La Palma has been almost my second home during the last 4 years, I could not forget to thank everyone in MAGIC and LST with whom I was on a shift. This is over 30 people sharing a passion for barraquitos, cabrito, arepas and, especially, ronmiel. After-shift nights are experiences that everyone should try at least once.

Per suposat, he d'agrair a tots els companys de batalles del departament que m'han acompanyat durant part o la totalitat de la tesi. A la Núria per ser la meva predecessora més directa i introduir-me en els secrets del departament, al Nico com a organitzador oficial d'activitats extra-laborals, a l'Alfred, tot i la nostra relació fallida "per 5 cm", i a la Laia, que el va enganxar després. Vull agrair al Dani el seu suport i la meva culturització en el món dels jocs de taula, al Pau pels seus estats de Whatsapp que tant debat generaven, i a l'Elina per la seva amabilitat infinita. No em vull quedar sense agrair a les dues incorporacions més recents al departament: a l'Òscar per la seva energia i la seva visió de futur d'un divendres sense tardes laborals, i a la Mar per ser una de les millors persones que conec i portar l'alegria sempre a sobre, fins i tot quan la FPI i el màster no li ho han posat fàcil. A tota la resta de doctoroands i postdocs amb qui he compartit aquests anys: Lluís, Jose, Sam, David, Ali, Xiying, Juan, Katie, Davide,

Héctor, Igansi, Dani Pacheco, i tots els que hem deixo, gràcies també per fer del departament un lloc al que ve de gust anar.

Finalment, vull agrair als meus pares, i a la meva família en general, el seu interès en els meus projectes, tot i no posar-ho jo fàcil a vegades. També pel seu suport no només ara, sinó durant tota la meva vida. Fins i tot en els moments difícils. Moltes gràcies.

RESUM EN CATALÀ

Alguns sistemes binaris formats per un objecte compacte, que pot ser un estel de neutrons o un forat negre, i una estrella companya típicament no degenerada s'han observat emetent en un ampli rang de freqüències, des de ràdio fins a raigs gamma. Aquests sistemes normalment es classifiquen com a binàries de raigs X o de raigs gamma, depenent de la freqüència a la qual la seva emissió és màxima. Al contrari que a les estrelles convencionals, una gran part d'aquesta emissió no pot ser explicada mitjançant processos tèrmics, i per tant és necessari que es donin mecanismes no tèrmics d'emissió de radiació. Les interaccions entre l'estrella i l'objecte compacte poden resultar en el llançament d'*outflows* de plasma originats al voltant de l'objecte compacte. Aquests *outflows* poden adquirir velocitats properes a la de la llum i poden accelerar partícules carregades fins a energies relativistes. Part de l'emissió no tèrmica que s'observa a les binàries de raigs X i gamma prové precisament del refredament radiatiu no tèrmic d'aquestes partícules. A més, quan l'estrella companya és molt massiva, aquesta genera un fort vent estel·lar que interacciona amb els *outflows* i els afecta tant dinàmicament com radiativa.

El principal objectiu d'aquesta tesi des del punt de vista teòric és l'estudi de les interaccions entre els *outflows* de binàries de raigs X i gamma i el vent estel·lar d'una companya massiva. Per això, hem desenvolupat una sèrie de models semi-analítics que donen una visió completa d'aquestes interaccions en diferents tipus d'escenaris. En ells, s'adopta una prescripció simplificada de la trajectòria que segueixen els *outflows* per tal que els càlculs es puguin realitzar en un ordinador comú. L'evolució de les partícules no tèrmiques al llarg d'aquesta trajectòria es calcula tenint en compte que es refreden mitjançant diferents processos no tèrmics, com l'expansió adiabàtica, o les pèrdues per sincrotró i Compton invers. Per tal d'obtenir l'emissió detectada per l'observador, l'emissió intrínseca dels *outflows* es corregida per l'efecte del *beaming* relativista (en cas que les velocitats involucrades siguin prou grans), i per processos d'absorció mediats pels camps estel·lars de fotons i ions.

Els resultats de la modelització teòrica inclouen distribucions espectrals d'energia i corbes de llum directament comparables amb les dades observacionals. També s'obtenen mapes ràdio per a l'emissió a gran escala dels *outflows*. Aquests últims permeten visualitzar directament l'efecte dinàmic del vent estel·lar en la trajectòria dels *outflows*, que adquireixen una forma d'hèlix o espiral. Aquesta trajectòria dona lloc a asimetries a les corbes de llum a diferents rangs d'energia, així com canvis en les distribucions espectrals d'energia deguts principalment a variacions en processos que depenen de l'angle entre l'estrella o l'observador, i l'*outflow*.

En relació a la part observacional, aquesta tesi es focalitza en l'anàlisi de l'emissió potencial de raigs gamma de molt alta energia (per sobre dels 100 GeV) de la binària de raigs X MAXI J1820+070, observada amb els telescopis MAGIC. L'anàlisi es realitza a través d'un *software* personalitzat de MAGIC, que permet reconstruir l'energia i direcció d'arribada d'un raig gamma a través de la llum Cherenkov produïda per la cascada electromagnètica que el raig gamma genera en entrar a l'atmosfera terrestre. Per tal de tenir una visió més global de la font estudiada, l'anàlisi de molt altes energies es contextualitza amb dades multifreqüència de ràdio a raigs gamma d'alta energia, per sobre de 100 MeV.

Els resultats observacionals consisteixen en un estudi multifreqüència de la font MAXI J1820+070 en forma de corbes de llum i distribucions espectrals d'energia que utilitzen dades de diferents telescopis a freqüències ràdio, òptiques, de raigs X i de raigs gamma. La font no es detecta en raigs gamma per sobre de 100 MeV, i només es poden obtenir límits superiors del flux a aquestes energies. Tanmateix, aquests límits, juntament amb els fluxos a altres freqüències, permeten acotar significativament les propietats d'un emissor potencial de raigs gamma a MAXI J1820+070, principalment la seva mida i localització.

En conclusió, aquesta tesi profunditza en el coneixement de les interaccions entre el vent estel·lar i els *outflows* de sistemes binaris d'altes energies. Es mostra que aquestes interaccions s'han de tenir en compte per tal de caracteritzar el subconjunt d'aquests sistemes amb una estrella massiva, en els quals el vent estel·lar és potent. En aquesta tesi també es mostra que les observacions de sistemes binaris en raigs gamma d'altes i molt altes energies permeten limitar de manera important les propietats dels *outflows*, fins i tot quan les fonts no son detectades i només es poden obtenir límits superiors en els fluxos.

ABSTRACT

Some binary systems consisting of a compact object, which can be either a neutron star or a black hole, and typically a non-degenerate companion star, have been shown to emit broadband radiation from radio up to gamma-ray frequencies. These systems are normally classified as X-ray or gamma-ray binaries, depending on the frequency at which their emission has its maximum. Unlike with stars, a big part of the observed emission cannot be explained by thermal radiation, and therefore non-thermal radiative processes need to be invoked. The interactions between the star and the compact object may result in the launching of outflows of plasma originating around the compact object position. These outflows can attain speeds close to the speed of light, and be an efficient site for acceleration of charged particles up to relativistic energies. A part of the non-thermal emission observed from X-ray and gamma-ray binaries comes precisely from the non-thermal radiative cooling of these accelerated particles. Additionally, when the companion star is very massive, it produces a strong stellar wind that interacts with the aforementioned relativistic outflows, modifying both their dynamical and radiative evolution.

The main theoretical objective of this thesis is the study the interactions between the outflows of X-ray and gamma-ray binary systems and the stellar wind of a massive companion star. For this purpose, we developed versatile semi-analytical models that give a complete view of these interactions for different kinds of systems. A simplified computation (although consistent with the simulations) of the trajectory followed by the outflows is adopted in order speed up the calculations and enable their performance in common computers. The evolution of the non-thermal particles is then computed along the defined trajectory, taking into account that they cool down through different non-thermal processes, like adiabatic expansion, or synchrotron and inverse Compton losses. In order to obtain the emission seen by a distant observer, the intrinsic emission of the outflows is corrected by applying relativistic beaming (when the involved speeds are high enough) and accounting for absorption processes with the stellar photon and ion fields.

The results of the theoretical modeling include broadband spectral energy distributions and light curves that are directly comparable with the observational data. Radio sky maps are also obtained for the large-scale emission of the outflows. The latter allows to directly visualize the dynamical effect of the stellar wind in the outflow trajectory, which acquires a helical or spiral-like pattern. This modified trajectory gives rise to asymmetries in the light curves at different energy ranges,

as well as changes in the spectral energy distributions mostly due to variations of angle-dependent processes influencing the outflow emission.

From the observational point of view, this thesis focuses on the analysis of the potential very high-energy gamma-ray emission above 100 GeV of the X-ray binary MAXI J1820+070, as seen by the MAGIC telescopes. The analysis is done through a custom software developed by MAGIC, which allows to reconstruct the arrival direction and energy of a gamma ray from the Cherenkov light emitted by the electromagnetic cascade that the gamma ray generates when it enters the atmosphere of the Earth. In order to have a more general picture of the studied source, the very high-energy analysis is contextualized with multiwavelength data from radio to high-energy gamma rays above 100 MeV.

The observational results consist on a multiwavelength study of MAXI J1820+070 in the form of light curves and spectral energy distributions that use data from a number of telescopes at radio, optical, X-ray and gamma-ray frequencies. The source is not detected in gamma-rays above 100 MeV, and only flux upper limits can be given for those energies. Nevertheless, the obtained upper limits, together with the observed fluxes at other frequencies, are enough to constrain significantly the properties of a potential gamma-ray emitter in MAXI J1820+070, mainly in terms of its size and location.

In conclusion, this thesis deepens in our understanding of the interactions between the stellar wind and the outflows of high-energy binary systems. It shows that these interactions must be taken into account in order to properly characterize the subset of those binary systems hosting a massive companion star, in which a powerful stellar wind is present. In this thesis, it is also shown that observations in high-energy and very high-energy gamma rays of binary systems allow to set meaningful limits to the outflow properties, even when the sources are not detected and only upper limits in the flux are obtained.

PUBLICATIONS

Complete list of publications at the moment of thesis deposit.

Published articles in this thesis

Molina, E. and V. Bosch-Ramon (2018). "Nonthermal emission from high-mass microquasar jets affected by orbital motion." In: *A&A* 618, A146, A146.

Molina, E. and V. Bosch-Ramon (2020). "A dynamical and radiation semi-analytical model of pulsar-star colliding winds along the orbit: Application to LS 5039." In: *A&A* 641, A84, A84.

Molina, E., S. del Palacio, and V. Bosch-Ramon (2019). "A model for high-mass microquasar jets under the influence of a strong stellar wind." In: *A&A* 629, A129, A129.

Collaboration articles

Abdalla, H. et al. (2021). "Sensitivity of the Cherenkov Telescope Array for probing cosmology and fundamental physics with gamma-ray propagation." In: *J. Cosmology Astropart. Phys.* 2021.2, 048, p. 048.

Abeysekara, A. U. et al. (2018). "Periastron Observations of TeV Gamma-Ray Emission from a Binary System with a 50-year Period." In: *ApJ* 867.1, L19, p. L19.

Abeysekara, A. U. et al. (2020). "The Great Markarian 421 Flare of 2010 February: Multiwavelength Variability and Correlation Studies." In: *ApJ* 890.2, 97, p. 97.

Acciari, V. A. et al. (2018). "Constraining dark matter lifetime with a deep gamma-ray survey of the Perseus galaxy cluster with MAGIC." In: *Physics of the Dark Universe* 22, pp. 38–47.

Acciari, V. A. et al. (2019a). "Constraints on Gamma-Ray and Neutrino Emission from NGC 1068 with the MAGIC Telescopes." In: *ApJ* 883.2, 135, p. 135.

Acciari, V. A. et al. (2019b). "Measurement of the extragalactic background light using MAGIC and Fermi-LAT gamma-ray observations of blazars up to z = 1." In: *MNRAS* 486.3, pp. 4233–4251.

Acciari, V. A. et al. (2020a). "A search for dark matter in Triangulum II with the MAGIC telescopes." In: *Physics of the Dark Universe* 28, 100529, p. 100529.

Acciari, V. A. et al. (2020b). "Bounds on Lorentz Invariance Violation from MAGIC Observation of GRB 190114C." In: *Phys. Rev. Lett.* 125.2, 021301, p. 021301.

Acciari, V. A. et al. (2020c). "Multiwavelength variability and correlation studies of Mrk 421 during historically low X-ray and γ-ray activity in 2015-2016." In: *MNRAS*.

Acciari, V. A. et al. (2020d). "New Hard-TeV Extreme Blazars Detected with the MAGIC Telescopes." In: *ApJS* 247.1, 16, p. 16.

Acciari, V. A. et al. (2020e). "Unraveling the Complex Behavior of Mrk 421 with Simultaneous X-Ray and VHE Observations during an Extreme Flaring Activity in 2013 April." In: *ApJS* 248.2, 29, p. 29.

Acciari, V. A. et al. (2021a). "MAGIC Observations of the Nearby Short Gamma-Ray Burst GRB 160821B." In: *ApJ* 908.1, 90, p. 90.

Acciari, V. A. et al. (2021b). "Multiwavelength variability and correlation studies of Mrk 421 during historically low X-ray and γ-ray activity in 2015-2016." In: *MNRAS* 504.1, pp. 1427–1451.

Acharyya, A. et al. (2021). "Sensitivity of the Cherenkov Telescope Array to a dark matter signal from the Galactic centre." In: *J. Cosmology Astropart. Phys.* 2021.1, 057, p. 057.

MAGIC Collaboration et al. (2018a). "Constraining very-high-energy and optical emission from FRB 121102 with the MAGIC telescopes." In: *MNRAS* 481.2, pp. 2479–2486.

MAGIC Collaboration et al. (2018b). "Detection of persistent VHE gamma-ray emission from PKS 1510-089 by the MAGIC telescopes during low states between 2012 and 2017." In: *A&A* 619, A159, A159.

MAGIC Collaboration et al. (2019a). "A fast, very-high-energy γ-ray flare from BL Lacertae during a period of multi-wavelength activity in June 2015." In: *A&A* 623, A175, A175.

MAGIC Collaboration et al. (2019b). "Deep observations of the globular cluster M15 with the MAGIC telescopes." In: *MNRAS* 484.2, pp. 2876–2885.

MAGIC Collaboration et al. (2019c). "Discovery of TeV γ-ray emission from the neighbourhood of the supernova remnant G24.7+0.6 by MAGIC." In: *MNRAS* 483.4, pp. 4578–4585.

MAGIC Collaboration et al. (2019d). "Observation of inverse Compton emission from a long γ-ray burst." In: *Nature* 575.7783, pp. 459–463.

MAGIC Collaboration et al. (2019e). "Teraelectronvolt emission from the γ-ray burst GRB 190114C." In: *Nature* 575.7783, pp. 455–458.

MAGIC Collaboration et al. (2019f). "Testing emission models on the extreme blazar 2WHSP J073326.7+515354 detected at very high energies with the MAGIC telescopes." In: *MNRAS* 490.2, pp. 2284–2299.

MAGIC Collaboration et al. (2020a). "An intermittent extreme BL Lac: MWL study of 1ES 2344+514 in an enhanced state." In: *MNRAS* 496.3, pp. 3912–3928.

MAGIC Collaboration et al. (2020b). "Broadband characterisation of the very intense TeV flares of the blazar 1ES 1959+650 in 2016." In: *A&A* 638, A14, A14.

MAGIC Collaboration et al. (2020c). "Detection of the Geminga pulsar with MAGIC hints at a power-law tail emission beyond 15 GeV." In: *A&A* 643, L14, p. L14.

MAGIC Collaboration et al. (2020d). “MAGIC observations of the diffuse γ-ray emission in the vicinity of the Galactic center.” In: *A&A* 642, A190, A190.

MAGIC Collaboration et al. (2020e). “MAGIC very large zenith angle observations of the Crab Nebula up to 100 TeV.” In: *A&A* 635, A158, A158.

MAGIC Collaboration et al. (2020f). “Monitoring of the radio galaxy M 87 during a low-emission state from 2012 to 2015 with MAGIC.” In: *MNRAS* 492.4, pp. 5354–5365.

MAGIC Collaboration et al. (2020g). “Study of the variable broadband emission of Markarian 501 during the most extreme Swift X-ray activity.” In: *A&A* 637, A86, A86.

MAGIC Collaboration et al. (2020h). “Studying the nature of the unidentified gamma-ray source HESS J1841-055 with the MAGIC telescopes.” In: *MNRAS* 497.3, pp. 3734–3745.

MAGIC Collaboration et al. (2020i). “Testing two-component models on very high-energy gamma-ray-emitting BL Lac objects.” In: *A&A* 640, A132, A132.

MAGIC Collaboration et al. (2021). “VHE gamma-ray detection of FSRQ QSO B1420+326 and modeling of its enhanced broadband state in 2020.” In: *A&A* 647, A163, A163.

Conference proceedings

Hoang, J., **Molina, E.**, and et al. (2019). “Multiwavelength observation of MAXI J1820+070 with MAGIC, VERITAS and H.E.S.S.” In: *36th International Cosmic Ray Conference (ICRC2019)*. Vol. 36. International Cosmic Ray Conference, p. 696.

Molina, E. and V. Bosch-Ramon (2019). “The influence of the optical star on the jets of high-mass microquasars.” In: *Frontier Research in Astrophysics - III. 28 May - 2 June 2018. Mondello (Palermo)*, p. 63.

CONTENTS

1

INTRODUCTION

A significant fraction of the stars are formed in gravitationally bound systems with two or more members. This fraction increases steadily with the stellar mass, being more than 60% for high-mass stars above 8 $M_\odot$ (Duchêne and Kraus 2013; Moe and Di Stefano 2017). In binary systems with at least one high-mass star, the most massive star will evolve faster, typically exploding as a supernova and leaving a compact object (CO) behind, which may be either a black hole (BH) or a neutron star (NS). In those cases for which the two components of the binary system are close enough, important interactions between the CO and the companion star take place. These interactions may be in the form of matter accretion by the CO and subsequent launching of bipolar outflows (microquasar scenario), or, when the CO is a non-accreting pulsar, in the form of strong collisions between the pulsar and stellar winds (pulsar-wind scenario).

The systems described above have been shown to emit radiation in a broad frequency range, from radio to X-rays and (in some cases) even gamma rays. Depending on the energy at which their spectral energy distribution (SED) peaks, they are known as either X-ray or gamma-ray binaries. Such an emission spectrum cannot be explained by thermal processes alone, and therefore non-thermal mechanisms need to be invoked. This implies the existence of a population of charged particles that are accelerated up to relativistic energies, and which are the responsible of the observed non-thermal emission through their cooling via radiative processes. In many astrophysical scenarios, charged particles are thought to be accelerated mainly via the diffusive shock acceleration mechanism. In this process, particles gain energy by multiple crossings of a shock wave, enabled by reflections on magnetic inhomogeneities both upstream and downstream of the shock (see, e.g., Drury 1983, for the details). This mechanism is also known as first-order Fermi acceleration, named after Enrico Fermi, and due to the particle energy gain being directly proportional to the shock speed. Other processes, like second-order Fermi acceleration, the converter mechanism or magnetic reconnection, can also lead to efficient particle acceleration in binary systems (e.g. Bosch-Ramon and Rieger 2012). Once particles are accelerated to relativistic energies, they are also cooled down by a number of non-thermal radiative and non-radiative processes, the relative importance of each of them depending on the exact conditions in the region. In general terms, we can highlight synchrotron and inverse Compton (IC) as dominant mechanisms for the radiative cooling of particles, especially leptons. For hadrons, proton-

proton interactions seem to be the most efficient cooling processes. We refer the reader to Bosch-Ramon and Khangulyan 2009; Dubus 2013 for reviews on the different radiative processes taking place in X-ray and gamma-ray binary systems.

In this thesis, we focus (although not exclusively) on the study of binary systems hosting a CO and a massive companion star above $\sim 8\ \mathrm{M}_{\odot}$. In particular, we pay attention on the influence of the stellar wind on the non-thermal emitter morphology and radiative output. We begin by exploring in more detail the two main scenarios proposed to explain the observed emission of X-ray and gamma-ray binaries.

1.1 MICROQUASAR SCENARIO

Microquasars are binary systems made of a CO that accretes matter from a typically non-degenerate companion star, and launches relativistic outflows (see Fig. 1.1 for an artistic representation). In low-mass systems, matter accretion typically takes place when the star overflows its Roche lobe in late evolutionary stages of its life (e.g., Paczyński 1971). In high-mass microquasars (HMMQs) the CO can also accrete matter by capturing a fraction of the intense stellar wind (e.g., El Mellah et al. 2019). A particular case of wind capture happens in systems with a Be companion, in which matter accretion suffers periodic enhancements when the CO crosses the dense decretion disk of the star (e.g., Reig 2011).

In Roche lobe overflow scenarios, and in some wind-capturing cases, an accretion disk is formed around the CO in which the material spirals inwards due to viscous forces (see Shakura and Sunyaev 1973, for the classical α-disk model). Accretion disks typically feature a multi-color blackbody spectrum, with the inner regions being at temperatures of a few million Kelvin and emitting mostly in (soft) X-rays, and the outer regions being progressively cooler and emitting at lower frequencies. In some accretion states, a region of hot material forms around the CO, the so-called corona. This corona is believed to be the responsible for most of the emission of the hard X-rays through IC with the low-energy disk photons. Classical reviews on microquasars can be found in Mirabel and Rodríguez 1999; Fender and Muñoz-Darias 2016.

Periodically through the life of a microquasar, a part of the material surrounding the CO (either from the disk or the corona) is ejected perpendicularly to the disk in the form of collimated and relativistic bipolar outflows, known as jets. The mechanisms by which jets are accelerated and collimated are not fully understood, although they may be powered by (a combination of) the accretion process, the CO rotation or the magnetic field (e.g., Romero et al. 2017), and can be efficient sites for particle acceleration up to TeV energies. Jets are typically observed at radio frequencies at scales much larger than

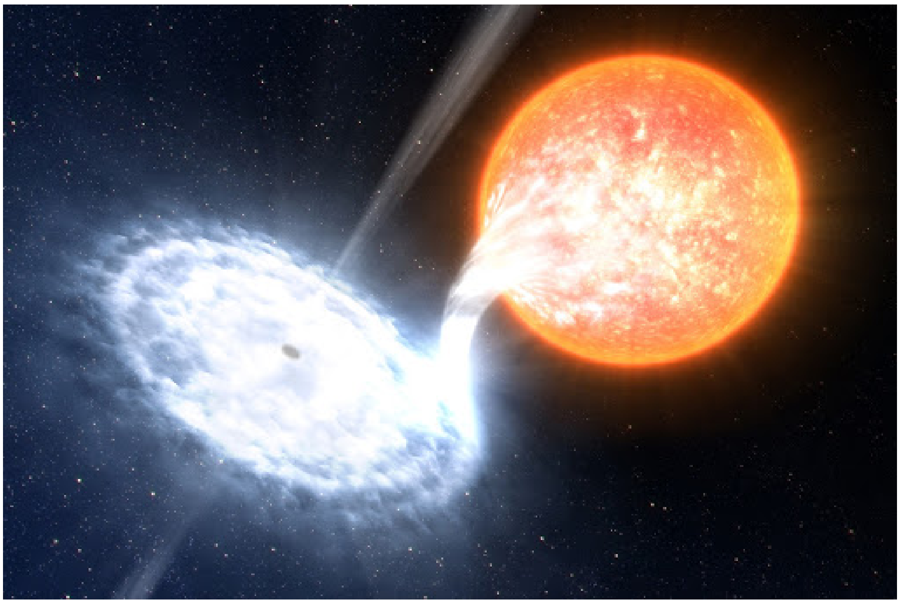

Figure 1.1: Artist impression of a microquasar. Credit: L. Calçada / ESO.

the binary system, where this radiation is not absorbed by the stellar wind ions through free-free absorption. Radio emission indicates the presence of a non-thermal population of particles, which may also radiate significantly at other frequencies up to gamma rays (see Bosch-Ramon and Khangulyan 2009, for a review on the different radiation processes potentially taking place in microquasars). Most X-ray binaries hosting a BH or a weakly magnetized NS are thought to be microquasars, although jets may be too dim and are not always detected. For highly magnetized NSs, the strong magnetic field of the latter may truncate the inner parts of the accretion disk, and channel the material on to the magnetic poles of the NS. This gives rise to an X-ray pulsar instead of a microquasar (e.g., Nagase 1989).

In HMMQs, the strong wind from the massive companion star, with a typical speed of 2000 – 3000 km s^{-1} and a mass-loss rate of 10^{-6} – 10^{-5} $M_{\odot}$ yr^{-1} (e.g., Muijres et al. 2012), can have an important effect on the propagation of the jets. This is so both because the jets have to propagate through a dense medium filled with wind material, and because the lateral impact of the stellar wind may deviate them and alter their shape significantly with respect to a windless scenario (as it is thought to be the case in typical low-mass microquasars).

Perhaps the most likely effect that the stellar wind has on the jets is the bending of the latter away from the star, relative to their initial direction perpendicular to the plane of the accretion disk. For a given stellar wind, the bending becomes more prominent the less powerful the jets are. For sufficiently weak jets, the interaction with the stellar wind can result in their disruption within the binary system scales (see simulations in Perucho and Bosch-Ramon 2008; Yoon and Heinz 2015). For significant jet bending (i.e., when the bending angle is larger than the half-opening angle of the jets), the orbital motion of the system and the Coriolis force associated to it, may result in helical-shaped jets at large scales (e.g., Bosch-Ramon and Barkov 2016). This helix-like path may last up to a distance of several times the orbital separation, where instabilities associated with the jet-wind interaction grow significantly and break the defined trajectory.

Another important effect to take into account when studying the jet-wind interaction is the eventual recollimation of the jets at the binary system scales (Perucho et al. 2010; Yoon et al. 2016). This happens when the jet lateral pressure, which decreases as the jet propagates away from the CO and expands, is overcome by the wind ram pressure, which remains approximately constant within the binary system scales. At this point a recollimation shock develops, which can trigger particle acceleration via the first-order Fermi mechanism. This shock is necessarily asymmetric given the geometry of the jet-wind interaction, meaning that the regions of the jets facing the star are more compressed than those away from it. We note that jet recollimation only happens for sufficiently low jet powers, since for powerful jets the jet-wind pressure balance is never reached and the jets do not suffer a strong recollimation shock.

There are two main known systems in which the aforementioned interactions should be very relevant (although not necessarily easy to observe): Cygnus X-1 and Cygnus X-3. The former consists of a BH and an O-type star with masses of ~ 21 and ~ 41 $M_{\odot}$, respectively, according to the latest measurements (Miller-Jones et al. 2021). Cygnus X-3 may have either a BH or NS with ~ 2.4 $M_{\odot}$ as a compact object, with a companion Wolf-Rayet star of ~ 10 $M_{\odot}$ (Zdziarski et al. 2013; Koljonen and Maccarone 2017). Both sources display non-thermal emission from radio up to high-energy (HE) gamma rays above 100 MeV (see Zanin et al. 2016; Zdziarski et al. 2018, respectively, and references therein). Helical radio jets have been observed on scales of tens of microarcseconds in Cygnus X-3 during two flares in 1997 and 2001 (Mioduszewski et al. 2001; Miller-Jones et al. 2004), although the causes for this shape are not firmly established.

1.2 PULSAR-WIND SCENARIO

The second scenario invoked to explain the emission observed in gamma-ray binaries involves the presence of a young, non-accreting pulsar orbiting around a massive star. In this scenario, the relativistic outflow consists of (mainly shocked) pulsar wind that is confined and collimated by the stellar wind, and flows away from the binary in the star-pulsar direction (see Fig. 1.2 for an artist impression). Shocks are created as the result of the wind-wind interaction, which leads to the acceleration of non-thermal particles (see Bosch-Ramon and Barkov 2011, for a detailed study on the interaction between the stellar

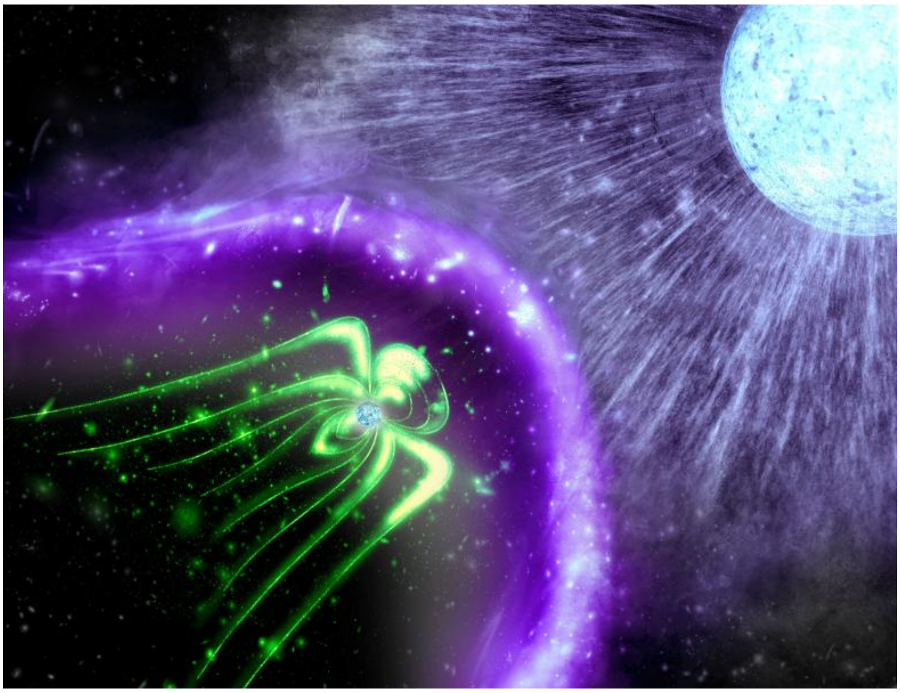

Figure 1.2: Impression of a pulsar-wind binary system. Credit: Kavli IPMU.

and pulsar winds). The aperture of the contact discontinuity (CD), i.e., the surface where the wind pressures are equal, between the shocked pulsar and stellar winds depends on the pulsar-to-star wind momentum-rate ratio, with lower ratios resulting in a more collimated outflow (see Bogovalov et al. 2008, for an analytical estimation of this aperture angle consistent with the numerical simulations).

Similarly as with helical microquasar jets, orbital motion results in the formation of a spiral structure for the shocked pulsar wind, with the difference that now the flow mainly propagates in the orbital plane, rather than perpendicularly to it. According to the simulations (Bosch-Ramon et al. 2015) the spiral pattern may survive for distances of a few dozen times the orbital separation, until instability growth and mixing with the stellar wind dissolve the pattern. For highly eccentric systems, even at the binary scales, the spiral shape is disrupted around the direction of the apastron, where the pulsar and stellar winds are quickly mixed and move roughly in a straight line (Barkov and Bosch-Ramon 2016; Bosch-Ramon et al. 2017).

In those pulsar-wind binaries hosting a Be star, the presence of an anisotropic wind typical of this kind of stars (e.g., Porter and Rivinius 2003) should be taken into account for a proper characterization of the system. In particular, the interaction of the pulsar wind and the decretion disk of the Be star should have a significant influence on the properties of the shocked outflow, both from a hydrodynamical and a radiative point of view. This effect is especially important for those systems in which the orbital separation is only of a few stellar radii close to periastron, and it can be strongly dependent on the orbital inclination with respect to the disk. On the other side of the orbit, far from the star, the "shadow" of the disk may create a region free of polar stellar wind where the pulsar wind could propagate without encountering much resistance by the already diluted disk. Therefore, the presence of a decretion disk in gamma-ray binaries must significantly change the outflow properties with respect to the case of an isotropic stellar wind (see, e.g., the hydrodynamical simulations performed in Okazaki et al. 2011).

Given that the properties of the non-thermal emitter and its environment in a pulsar-wind scenario are similar to those in a microquasar scenario (e.g., Dubus 2013), the radiative outputs of these two cases are also expected to be alike. As a consequence of this, it is often not possible to firmly establish the nature of a gamma-ray binary system from its non-thermal emission only. Among the key features that would allow for a discrimination between the two scenarios are the observational signatures of accretion (in the form of quasi-periodic oscillations or thermal X-ray emission, for example), which only takes place in microquasars, or the detection of pulsed radio or gamma-ray emission, which indicates the presence of a non-accreting pulsar and therefore points towards a pulsar-wind scenario.

It was precisely the detection of pulsed emission what confirmed PSR B1259-63 and PSR J2032+4127 to be pulsar-wind binaries, with the former detected in radio (Johnston et al. 1992) and the latter in gamma rays (Abdo et al. 2009). Both sources host a young non-accreting pulsar orbiting a massive Be star with ~ 30 and ~ 15 $M_\odot$, respectively (Negueruela et al. 2011; Lyne et al. 2015). The pulsar-wind scenario has also been proposed for other gamma-ray binaries such as HESS J0632+057 (Moritani et al. 2015; Barkov and Bosch-Ramon 2018) and LS 5039 (Takahashi et al. 2009; Moldón et al. 2012; Zabalza et al. 2013; Dubus et al. 2015), although the microquasar scenario cannot be ruled out for these sources.

1.3 OBSERVATIONS OF VERY HIGH-ENERGY GAMMA RAYS

Some of the sources mentioned in the previous section have been detected at very high-energy (VHE) gamma rays above 100 GeV. Photons of such high energies only reach the Earth with very low fluxes (e.g., a very bright VHE source like the Crab Nebula has a flux of about 10 photons $\mathrm{km}^{-2}\ \mathrm{s}^{-1}$ at 100 GeV, and even less at higher energies), which makes necessary the use of large collection areas for their detection. This effectively prevents observations of VHE gamma rays from space due to the large sizes required for the potential satellites. On the other hand, the Earth atmosphere is opaque to gamma rays, and therefore they cannot be directly detected from the surface of our planet.

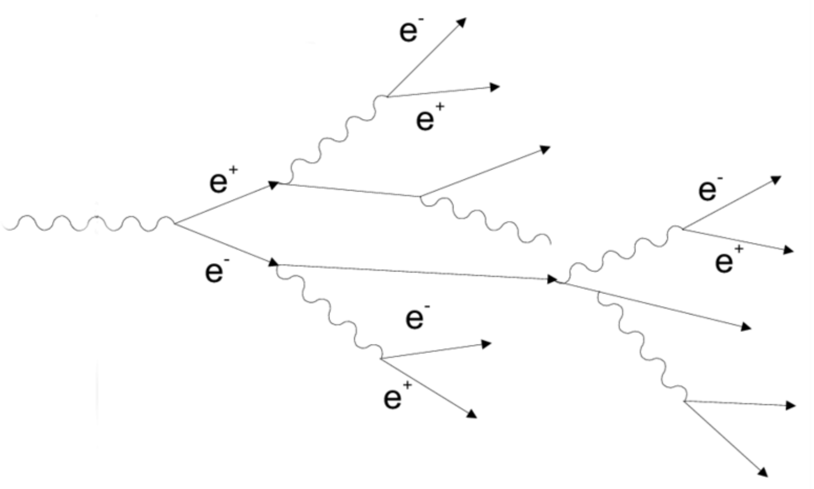

Figure 1.3: Schematic representation of an electromagnetic shower triggered by a gamma-ray photon. Original image from Roldan and Lecoq 2021.

The absorption of VHE gamma rays by the atmosphere comes, however, with a convenient advantage: the development of electromagnetic showers (or cascades). When a VHE photon reaches the upper layers of the atmosphere, it creates an electron-positron pair by interacting with an air nucleus. The generated electron and positron in turn emit high-energy photons by bremsstrahlung, each of which produces electron-positron pairs, repeating the process. Each step of this process results in lower average energy particles, and the procedure continues until the average electron/positron energy drops below a critical value at which ionization losses become dominant over bremsstrahlung. Also, as lower energy photons are produced, other processes besides pair production become important for them, such as Compton scattering or photoelectric absorption, which also halt the shower development. The total number of particles produced by a gamma-ray photon (also called size of the cascade), and the height at which the shower is maximally developed, i.e. where the number of particles is highest, are therefore dependent on the initial gamma-ray energy. Higher energy photons result in a larger particle production and a lower height of maximum development. A sketch of the production of an atmospheric cascade is shown in Fig. 1.3. We refer the reader to Longair 1981 for a thorough description of the mechanisms that come into play in the production of electromagnetic showers in the Earth atmosphere.

As stated above, we cannot directly detect the original VHE photon, but we can nonetheless detect the products of the shower that it triggers. This can be done through different methods, although in this thesis we will focus on the observation of Cherenkov radiation emitted by shower electrons and positrons propagating in the atmosphere, i.e.

the radiation they emit as a consequence of moving faster than the speed of light in the air (e.g., Watson 2011). This Cherenkov light, emitted mainly in the optical and near ultraviolet, is collected by large mirror dishes and focused on a camera consisting of fast and sensitive photo-multiplying devices. The latter are needed due to the faint and short (a few nanosecond long) nature of the Cherenkov light flash triggered by a VHE gamma ray, and allow the discrimination of these flashes from the night sky background fluctuations (e.g., Hinton 2009; Lorenz and Wagner 2012). Moreover, one needs to have some process (normally at a software level) to discriminate gamma-ray photons from cosmic rays, which also produce atmospheric cascades with a similar pattern of Cherenkov light emission. The detection of the Cherenkov light produced by showers is done by imaging atmospheric Cherenkov telescopes (IACTs), the current generation of which consists of the MAGIC, H.E.S.S. and VERITAS telescopes (see Aleksić et al. 2016a,b; Aharonian et al. 2006; Bolmont et al. 2014; Weekes et al. 2002; Park et al. 2015, for a description of these instruments). These telescopes can detect the product Cherenkov photons of gamma rays with energies from ~ 50 GeV up to ~ 100 TeV. The lower limit of this range comes from the fact that showers generated by those gamma rays only produce a small number of particles, and therefore few Cherenkov photons. The upper limit arises mainly from the low photon rates at such high energies. The increased sensitivity of the next generation of IACTs in the CTA North and CTA South observatories (Cherenkov Telescope Array Consortium 2019) will allow to widen the effective energy range of the observations from ~ 20 GeV up to ~ 300 TeV. This new generation of telescopes will become fully operational within the next decade.

Another method to infer the arrival of a VHE gamma ray is the detection of its charged particle products at ground level. This is done through the Cherenkov light emitted by these particles when they interact with a liquid medium (typically water) located inside of large tanks. This technique requires longer exposure times to detect a source than IACTs (months or years versus hours), but has the advantage of covering a larger field of the sky, and a higher duty cycle owing to the fact that it also works during daytime. It becomes especially useful for gamma rays with energies above ~ 10 TeV for which showers can be more efficiently separated from those produced by cosmic rays, and the sensitivity of IACTs worsens significantly due to low statistics. The HAWC observatory (Abeysekara et al. 2013) and the recent LHAASO experiment (Bai et al. 2019) represent the main current facilities for the detection of gamma rays in water Cherenkov tanks.

1.4 OVERVIEW OF THIS THESIS

The main purpose of this thesis is to deepen in our understanding of the physical mechanisms leading to the observed non-thermal emission in binary systems, and especially in the interaction between stellar winds and relativistic outflows. On the one hand, this is done through semi-analytical modeling of these sources in the two scenarios described above: microquasars and pulsar-wind binaries. On the other hand, VHE gamma-ray observations with the MAGIC telescopes are also performed, and accompanied with multiwavelength data, so that the physical properties of the outflows producing such emission can be constrained. This thesis is divided in three distinct parts with a number of chapters, each of them corresponding to a published article (or in advanced stage of preparation).

Part i focuses on the theoretical modeling of binary systems with relativistic outflows. In Chapter 2, a non-relativistic semi-analytical model is presented to study the hydrodynamics and non-thermal emission of HMMQ jets in regions far from the binary system. Chapter 3 improves this model by including a fully relativistic approach, which allows for its application in regions close to the binary, where the jets propagate at a significant fraction of the speed of light. Finally, Chapter 4 studies the hydrodynamics and radiation in a pulsar-wind scenario, with a specific application to LS 5039.

Part ii of this thesis, consisting of a single chapter, is centered on the observational results obtained with the MAGIC telescopes for the microquasar MAXI J1820+070. This source is an X-ray binary discovered in 2018 after an exceptionally bright X-ray flare. Data at VHE is complemented with other observations down to radio frequencies to show a more complete picture of the source.

In Part iii, a summary of all the work done is presented, together with the main conclusions that can be extracted from each chapter. Also, future work perspectives on the field of X-ray and gamma-ray binaries are also given.

Additionally, this work also contains one appendix describing the monitoring of the HE emission from Cygnus X-3 since the start of this thesis, as well as the VHE observations performed during several outbursts undergone by this source in the same period.

Part I

MODELING OF RELATIVISTIC OUTFLOWS

2

LARGE-SCALE NON-THERMAL EMISSION IN HIGH-MASS MICROQUASAR JETS AFFECTED BY ORBITAL MOTION

This Chapter contains the published version of Molina and Bosch-Ramon (2018, A&A, 618, A146).

We describe a non-relativistic semi-analytical code developed to model jets in HMMQs accounting for both hydrodynamical and radiative effects. In these systems, the powerful wind from the companion star has a strong influence on the jet propagation, and can significantly change the jet trajectory with respect to a windless scenario. The work presented here focuses on the jet regions far from the binary system, where the jet flow is expected to have been slowed down by interactions with the environment, and relativistic effects can be neglected. We obtain the jet and counter-jet trajectories in these regions by applying numerical methods together with some analytical estimates taken mainly from Bosch-Ramon and Barkov 2016, which take into account the influence of the stellar wind and orbital motion.

The applied procedure defines a helical-shaped path for a one-dimensional leptonic emitter, which produces non-thermal radiation from radio to gamma rays through the synchrotron and IC mechanisms. Gamma-ray absorption by electron-positron pair production with the stellar photons (gamma-gamma absorption) is also accounted for, although its effects are mild due to the large distances to the star considered. In order to have a more general picture of the radiative outputs of HMMQ jets affected by the stellar wind, different values of the jet magnetic field and the system inclination are explored. Assuming that particle acceleration is important at scales larger than the binary system, the model predicts significant broadband emission from the helical jets, including an extended radio structure tracing a fraction of the first turn of the helix.

A&A 618, A146 (2018)
https://doi.org/10.1051/0004-6361/201833681

Astronomy & Astrophysics

Nonthermal emission from high-mass microquasar jets affected by orbital motion

E. Molina and V. Bosch-Ramon

Departament de Física Quàntica i Astrofísica, Institut de Ciències del Cosmos (ICCUB), Universitat de Barcelona (IEEC-UB), Martí i Franquès 1, 08028 Barcelona, Spain
e-mail: `emolina@fqa.ub.edu`

Received 20 June 2018 / Accepted 26 July 2018

ABSTRACT

Context. The stellar wind in high-mass microquasars should interact with the jet. This interaction, coupled with orbital motion, is expected to make the jet follow a helical, nonballistic trajectory. The jet energy dissipated by this interaction, through shocks for example, could lead to nonthermal activity on scales significantly larger than the system size.

Aims. We calculate the broadband emission from a jet affected by the impact of the stellar wind and orbital motion in a high-mass microquasar.

Methods. We employ a prescription for the helical trajectory of a jet in a system with a circular orbit. Subsequently, assuming electron acceleration at the onset of the helical jet region, we compute the spatial and energy distribution of these electrons, and their synchrotron and inverse Compton emission including gamma-ray absorption effects.

Results. For typical source parameters, significant radio, X- and gamma-ray luminosities are predicted. The scales on which the emission is produced may reduce, but not erase, orbital variability of the inverse Compton emission. The wind and orbital effects on the radio emission morphology could be studied using very long baseline interferometric techniques.

Conclusions. We predict significant broadband emission, modulated by orbital motion, from a helical jet in a high-mass microquasar. This emission may be hard to disentangle from radiation of the binary itself, although the light curve features, extended radio emission, and a moderate opacity to very high-energy gamma rays, could help to identify the contribution from an extended (helical) jet region.

Key words. X-rays: binaries – radiation mechanisms: non-thermal – stars: winds, outflows – stars: massive

1. Introduction

High-mass microquasars (HMMQ) are X-ray binaries that host a massive star and a compact object (CO) from which jets are produced. The stellar wind can strongly influence the jet propagation, both because the jet has to propagate surrounded by wind material, and because the wind lateral impact may significantly bend the jet away from the star. Several authors have used numerical and analytical methods to study, on the scales of the binary, the interaction of HMMQ jets with stellar winds and their radiative consequences (e.g., Romero et al. 2003; Romero & Orellana 2005; Perucho & Bosch-Ramon 2008, 2012; Owocki et al. 2009; Araudo et al. 2009; Perucho et al. 2010; Yoon & Heinz 2015; Bosch-Ramon & Barkov 2016; Yoon et al. 2016).

On scales larger than the binary system, orbital motion should also affect the dynamics of the jet, making it follow a helical trajectory (e.g., Bosch-Ramon 2013; Bosch-Ramon & Barkov 2016). There are a few well-established microquasars in which evidence of a helical jet has been observed; for example, SS 433, 1E 1740.7−2942 and Cygnus X-3 (Abell & Margon 1979; Mioduszewski et al. 2001; Stirling et al. 2002; Miller-Jones et al. 2004; Luque-Escamilla et al. 2015; see also Sell et al. 2010 for the possible case of Circinus X-1). In the case of SS 433, the jet helical geometry likely originates in the accretion disk (e.g., Begelman et al. 2006); in the case of 1E 1740.7−2942, the system likely hosts a low-mass star and the role of its wind could be minor; in the case of Cygnus X-3, the apparent jet helical shape has an unclear origin. Bosch-Ramon & Barkov (2016) proposed that Cygnus X-1 and Cygnus X-3 could be affected by orbital motion and the stellar wind, although the uncertainties on the jet and wind properties make quantitative predictions difficult. Unlike the case of Cygnus X-3, no clear evidence of a helical or bent jet has yet been found for Cygnus X-1 (Stirling et al. 2001).

In this work we study the implications of the impact of the stellar wind and orbital motion for the nonthermal emission of a HMMQ, from radio to gamma rays. Using an analytical prescription for the jet dynamics based on the results of Bosch-Ramon & Barkov (2016), the nonthermal radiation from a helical jet (spectra, light curves, and morphology) is computed numerically, considering a leptonic model with synchrotron and inverse Compton (IC) emission.

The paper is organized as follows: in Sect. 2, the interaction between the stellar wind and the jet is described. The technical aspects of the model are explained in Sect. 3. The results of the calculations are presented in Sect. 4 and a discussion is provided in Sect. 5. Unless stated otherwise, the convention $Q_x = Q/10^x$ is used throughout the paper, with Q in cgs units.

2. Jet-wind interaction

The physical scenario considered in this work consists of a massive star with a strong stellar wind and an accreting CO from which two jets are launched in opposite directions perpendicular to the orbital plane. The binary has a relatively compact orbit, taken circular for simplicity, with a period of $P = 5$ days and a separation of $d_\mathrm{O} = 3 \times 10^{12}$ cm ($M_1 + M_2 \approx 43\,M_\odot$).

The luminosity of the star is taken to be $L_\star = 10^{39}\,\mathrm{erg\,s^{-1}}$, and its temperature $T_\star = 4\times10^4\,\mathrm{K}$ ($R_\star \approx 10\,R_\odot$). The stellar wind is assumed to be spherically symmetric, with a mass-loss rate and a velocity of $\dot M_\mathrm{w} = 10^{-6}\,M_\odot\,\mathrm{yr^{-1}}$ and $v_\mathrm{w} = 2\times10^8\,\mathrm{cm\,s^{-1}}$, respectively (typical for O-type stars; e.g., Muijres et al. 2012). Such a system would have similar parameters to those of Cygnus X-1, although it would be significantly wider and with a weaker wind than Cygnus X-3 (but the adopted wind and jet momentum rate relation will be similar; see below).

The orbit is assumed to lie on the xy-plane, with the star at the center of coordinates. The CO would be on the x-axis, orbiting the star counter clockwise, and the jet (counter jet) would initially point along $\hat z$ ($-\hat z$). The axes are defined in a frame corotating with the CO around the companion star. The jets are assumed to have a conical shape, with an initial half-opening angle $\theta_{j0} = 0.1\,\mathrm{rad} \approx 5.7°$. In this work, we do not need to adopt a specific value for θ_{j0}, although to make our predictions qualitatively valid, it should be smaller than the jet deflection angle imposed by the wind impact (see below). We take an initial jet Lorentz factor of $\gamma_\mathrm{j} = 2$, although the final results are not sensitive to this parameter as long as the jet is strongly supersonic and mildly relativistic. The jet power is taken as $L_\mathrm{j} = 3\times10^{36}\,\mathrm{erg\,s^{-1}}$.

Figure 1 sketches the scenario under study. The jet goes through three stages, the first of which is not present in the figure: Initially, the jet moves perpendicularly to the orbital plane. Then, the wind impact produces an asymmetric recollimation shock on the jet, which gets inclined away from the star (stage 2). Further from the binary, the combined effect of the stellar wind and orbital motion leads to a (orbit-related) force that bends the already inclined jet, now against orbital motion (clockwise in Fig. 1). In this way, the jet becomes helical, with asymmetric shocks being expected because of the orbit-related force (stage 3). Here it is assumed that electrons are efficiently accelerated in those shocks, ascribed here to one specific point: the onset of the helical jet, which neglects the fact that acceleration may occur along the helical jet region. Relativistic protons may also be generated in those shocks, but their radiation efficiency would be much lower in general, and therefore they are not considered in our calculations (see e.g., Bosch-Ramon & Khangulyan 2009, for a discussion of the different electron and proton cooling timescales in HMMQ).

For the radiation calculations, a fraction $\eta_\mathrm{NT} = 10^{-2}$ of L_j is injected in the form of nonthermal electrons right where the jet starts its helical path. This fraction is only constrained by $\eta_\mathrm{NT} < 1$, although the predicted luminosities are proportional to its value and easy to translate if a different fraction is adopted. Nevertheless, adopting $\eta_\mathrm{NT} = 10^{-2}$ does not require particularly efficient acceleration processes. The inclination of the system with respect to the line of sight of the observer, assumed to be at a reference distance of $d = 3\,\mathrm{kpc}$, is characterized by the angle i. The values for the different fixed parameters of our model are listed in Table 1.

2.1. Wind impact: jet bending

Interaction between the stellar wind and the jet can lead to bending of the latter in the x-axis direction (stage 2 above). This bending can be characterized by an angle ϕ with respect to the jet initial direction (i.e., the z-axis; see Fig. 1). Following Bosch-Ramon & Barkov (2016) we introduce a nondimensional parameter, χ_j, which corresponds to the ratio between the wind momentum rate intercepted by the jet, and the jet momentum rate:

$$\chi_\mathrm{j} \approx \frac{\theta_{j0}\dot P_\mathrm{w}}{4\pi \dot P_\mathrm{j}} = \frac{\theta_{j0}\dot M_\mathrm{w}\, v_\mathrm{w}(\gamma_\mathrm{j}-1)c}{4\pi L_\mathrm{j}\gamma_\mathrm{j}\beta_\mathrm{j}} \approx 0.9\,\frac{\theta_{j0,-1}\dot M_{\mathrm{w},-6}\, v_{\mathrm{w},8.3}}{L_{\mathrm{j},36.5}\beta_\mathrm{j}}\,\frac{(\gamma_\mathrm{j}-1)}{\gamma_\mathrm{j}}, \quad (1)$$

where $\dot M_\mathrm{w}$ is in units of $M_\odot\,\mathrm{yr^{-1}}$ in the rightmost expression, $\dot P_\mathrm{w} = \dot M_\mathrm{w} v_\mathrm{w}$ is the stellar wind momentum rate, and $\dot P_\mathrm{j}$ is the jet momentum rate, which can be expressed in terms of L_j, γ_j, and the initial jet velocity in c units β_{j0}:

$$\dot P_\mathrm{j} = \frac{L_\mathrm{j}\gamma_\mathrm{j}\beta_{j0}}{c(\gamma_\mathrm{j}-1)}. \quad (2)$$

An approximate computation of the bending angle ϕ, with a discrepancy of less than 10% with respect to the numerical case, yields the following expression (for more details, see the Appendix in Bosch-Ramon & Barkov 2016):

$$\phi = \frac{\pi^2\chi_\mathrm{j}}{2\pi\chi_\mathrm{j} + 4\chi_\mathrm{j}^{1/2} + \pi^2}. \quad (3)$$

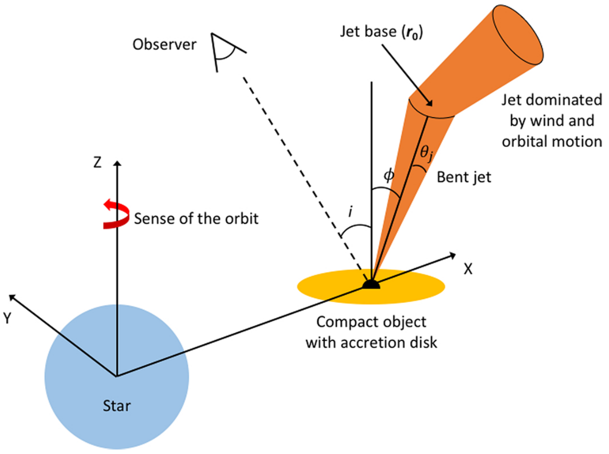

Fig. 1. Schematic representation of the onset of the helical jet. The position, with respect to the star, of the change in the jet initial (bent) direction is $\boldsymbol{r_0}$, where the jet bending starts to be dominated by the added effects of the stellar wind and orbital motion. The axes are defined in a frame corotating with the CO.

Table 1. Fixed parameters used in this work.

Parameter		Value
Star temperature	$T_\star$	4×10^4 K
Star luminosity	$L_\star$	10^{39} erg s^{-1}
Wind speed	v_w	2×10^8 cm s^{-1}
Wind mass-loss rate	$\dot M_\mathrm{w}$	10^{-6} $M_\odot$ yr^{-1}
Jet luminosity	L_j	3×10^{36} erg s^{-1}
Initial jet Lorentz factor	γ_j	2
Half-opening angle	θ_j	0.1 rad
Nonthermal energy fraction	η_NT	10^{-2}
Effective flow velocity	v_j	5×10^9 cm s^{-1}
Radial flow velocity	v_r	2×10^9 cm s^{-1}
Orbital separation	d_O	3×10^{12} cm
Period	P	5 days
Distance to the observer	d	3 kpc
Radio interferometer resolution	$FWHM$	1 mas

For bending angles $\phi < \theta_{j0}$, the lateral impact of the stellar wind may produce a weak recollimation shock or a sound wave in the jet, and the large-scale jet evolution should not be strongly affected (although the role of instability growth may still be important; see, e.g., Perucho & Bosch-Ramon 2008, 2012; Perucho et al. 2010 under uniform and clumpy stellar winds). However, when ϕ is significantly larger than θ_{j0}, a strong asymmetric recollimation shock is expected, with the jet substantially deviating from its initial direction. In such a case, the jet is likely to turn into a helical-shaped structure at larger scales (stage 3, above). Consequently, bending due to stellar wind impact becomes important for the jet evolution when $\phi > \theta_{j0}$.

2.2. Orbital effects: helical jet

The orbital motion of the system combined with a jet inclined by the stellar wind (stage 2) leads, through the orbit-related force, to a jet helical pattern. This effect becomes clearer for significant bending angles. Otherwise, for $\phi < \theta_{j0}$, the conical jet expansion will dominate the geometry of the resulting structure. We note that a helical pattern would be expected from an inclined jet even under ballistic jet propagation, but the presence of the stellar wind makes jet propagation nonballistic. Instability growth should also play a role, but here we consider its effects only phenomenologically through a slower jet flow, caused by the wind mass entrainment and hence deceleration associated to instabilities.

One can estimate the distance $x_{\rm turn}$ that a nonballistic jet travels in the x-axis direction before acquiring a negative velocity y-component, i.e., bending against the orbital motion. With the additional assumptions that the half-opening angle of the jet remains constant after being bent (see below), and that $x_{\rm turn}$ is much larger than the orbital separation, we get (see Bosch-Ramon & Barkov 2016, for the derivation of this expression)

$$x_{\rm turn} = \frac{K}{\sqrt{2\chi_{\rm j}}}\frac{v_{\rm w}}{\omega} \approx 1.3\times10^{13}\frac{K}{\sqrt{\chi_{\rm j}}}\frac{v_{\rm w,8.3}}{\omega_{-5}}\ {\rm cm}, \quad (4)$$

where ω is the orbital angular velocity, with the normalization corresponding to a period of several days (e.g., $\omega = 2\pi/5$ days $\approx 1.4\times10^{-5}$ rad s^{-1}), and K is a constant of $O(1)$, introduced to account for the specific details of the wind–jet interaction. Here we fix $K = 1$.

Knowing $x_{\rm turn}$ and ϕ, we can compute the height z at which the jet starts forming the helical structure: $z_{\rm turn} = x_{\rm turn}/\tan\phi$. For the parameters given above, and following Eqs. (3) and (4), the location vector of the beginning of the helical structure is $\boldsymbol{r_0} = (1.58, 0, 3.56)\times10^{13}$ cm, with $\phi = 19.8°$. We note that $x_{\rm turn} = 1.28\times10^{13}\,{\rm cm} \gg d_{\rm O}$, as required. The distance from $\boldsymbol{r_0}$ to the star is $D_\star = 3.88\times10^{13}$ cm and to the CO is $l_0 = 3.77\times10^{13}$ cm. The jet curvature due to orbital motion for distances smaller than l_0 is neglected, that is, $y_{\rm turn} = 0$.

The point $\boldsymbol{r_0}$ (the -helical- jet base hereafter) is the position where nonthermal electrons are injected. The evolution of these electrons is followed from this point onwards along the helical jet assuming that no more significant electron acceleration happens further downstream in the jet[1]. Electron acceleration may also happen closer to the binary system (see Sect. 5), but here we focus specifically on the nonthermal emission produced in the helical jet region.

From $\boldsymbol{r_0}$ onwards along the jet, the stellar wind should have a very important dynamical role. As the jet becomes helical due to the presence of wind plus orbital motion, the former is also pushing the latter in the radial direction. Therefore, the radial velocity ($v_{\rm r}$) of the jet flow may be as slow as the stellar wind itself, or higher if the shocked stellar wind is effectively accelerated radially by the jet. In addition, effects of wind entrainment are likely to affect the jet flow itself, slowing the latter down to an effective velocity $v_{\rm j} < \beta_{\rm j0}c$. We adopt here $v_{\rm r}$ and $v_{\rm j}$ as phenomenological parameters that fulfill $v_{\rm w} \lesssim v_{\rm r} \lesssim v_{\rm j}$. They provide a simplified prescription for the helical jet geometry, defining the pitch of the helical jet trajectory. It is also assumed that this trajectory is confined to the conical surface, characterized, in the nonrotating frame, by the direction determined by the vector $\boldsymbol{r_0}$ along the orbit in that frame (i.e., a ring traced by the points $\boldsymbol{r_0}$, plus the radial direction from the star), which should be a relatively good approximation as long as $l_0 \gg d_{\rm O}$.

The half-opening angle of the helical jet flow ($\theta_{\rm j}$) need not be constant, as the nonballistic nature of the jet trajectory, with weak-shock heating, rarefaction waves, wind (re)confinement, and mass-loading, may lead to (re)collimation or (re)widening of the helical jet, depending on the details of the jet and wind interaction. For simplicity, at this stage we assume $\theta_{\rm j} = \theta_{\rm j0}$. In addition, we also take $v_{\rm j} = 5\times10^9$ cm s^{-1} and $v_{\rm r} = 2\times10^9$ cm s^{-1}; this is somewhat arbitrary, but except for the radio morphology (see Sect. 5) their actual values do not qualitatively change the results. Hydrodynamical simulations are required to properly characterize $v_{\rm r}$, $v_{\rm j}$, $\theta_{\rm j}$, the role of instability growth, mass-loading, and so on. Nevertheless, we consider our dynamical model realistic on scales of a few $D_\star$, as large-scale perturbations should grow up to a size $\gtrsim D_\star$ to disrupt the helical structure.

3. Model description

We use a semi-analytical code to compute the energy and spatial distribution of the accelerated electrons. As the orbital period is significantly longer than the crossing time of the helical jet length ($l_{\rm max}/v_{\rm j}$), the nonthermal electrons are assumed to be in the steady state at each orbital phase.

3.1. Energy losses

Analytical expressions for the energy losses are used in this work. For synchrotron cooling, assuming, for simplicity, an isotropic magnetic field B in the flow frame, one obtains, in cgs units (Longair, 1981):

$$\dot{E}_{\rm sync} \approx -\frac{4}{3}c\sigma_{\rm T}\omega_{\rm mag}\gamma^2 \approx 1.6\times10^{-5}B_{-2}^2E^2\ {\rm erg\,s^{-1}}, \quad (5)$$

where $\sigma_{\rm T}$ is the Thomson cross-section, $\omega_{\rm mag} = B^2/8\pi$, and γ is the Lorentz factor of an electron with energy E. The magnetic field at the jet base is parametrized through the ratio of magnetic pressure to stellar photon energy density, $\eta_{\rm B}$, as

$$\frac{B^2}{8\pi} = \eta_{\rm B}\frac{L_\star}{4\pi c D_\star^2}. \quad (6)$$

This way of normalizing B allows an easy comparison between the expected luminosity of synchrotron and IC emission; for IC in the Thomson regime, the two processes contribute similarly for electrons of the same energy if $\eta_{\rm B} \sim 1$. However, for electrons of energy $\gtrsim m_e\,c^2/3k_{\rm B}T_\star$ (with $k_{\rm B}$ being the Boltzmann

---

[1] We note that as the jet propagation is nonballistic, (weak) acceleration regions may also exist all along the jet due to jet kinetic energy dissipation.

constant), which scatter photons in the IC Klein-Nishina regime, $\eta_{\rm B} \gtrsim 0.1$ already leads to global strong synchrotron dominance, which is corroborated by our calculations. One can relate $\eta_{\rm B}$ with the ratio of magnetic pressure to jet energy density ($\bar{\eta}_{\rm B}$) for the same B via: $\bar{\eta}_{\rm B} = \theta_{\rm j}^2(\eta_{\rm B}/4)(L_\star/L_{\rm j})(v_{\rm j}/c)$ ($\approx 0.14\,\eta_{\rm B}$ for the values adopted here).

Losses due to IC are computed as in Khangulyan et al. (2014) for an isotropic electron population embedded in the stellar photon field taken as a black body of temperature $T_\star$. This expression is valid in both the Thomson and the Klein-Nishina regimes and has an accuracy of $\sim 5\%$:

$$\dot{E}_{\rm IC} \approx -\frac{3\sigma_{\rm T}\pi m_e^2 c^2 R_\star^2 k_{\rm B}^2 T_\star^2}{2R^2 h^3} G(t)$$
$$\approx -3.8\times 10^{-3}\,\frac{R_{\star,12}^2 T_{\star,4.6}^2}{R_{14}^2}\,\frac{E\ln(1+5.3E)}{1+183E}\ {\rm erg\,s^{-1}}, \tag{7}$$

with $R_\star$ being the radius of the star, R the distance from the star to the emitter, $t = 4Ek_{\rm B}T_\star/m_e^2c^4$, and

$$G(t) = \frac{4.62t\ln(1+0.156t)}{1+5.62t}. \tag{8}$$

For a conical jet, adiabatic losses are

$$\dot{E}_{\rm ad} = -\frac{2}{3}\frac{v_\perp}{r_{\rm j}}E \approx -6.7\times 10^{-6}\frac{v_{\perp,8}}{r_{\rm j,13}}E\ {\rm erg\,s^{-1}}, \tag{9}$$

where $v_\perp \approx v_{\rm j}\theta_{\rm j}$ is the jet expansion velocity and $r_{\rm j}$ is the helical jet radius.

The total energy-loss rate is

$$\dot{E} = \dot{E}_{\rm sync} + \dot{E}_{\rm IC} + \dot{E}_{\rm ad}. \tag{10}$$

3.2. Electron distribution

The nonthermal electrons are injected in the jet base with an energy distribution that follows a power law of index -2, typical for efficient nonthermal sources (and for acceleration in nonrelativistic strong shocks; Drury 1983), plus a cutoff at high energies set by energy and escape losses:

$$Q(E) \propto E^{-2}\exp\left(-\frac{E}{E_{\rm cut}}\right). \tag{11}$$

We note that a much steeper $Q(E)$ would mean inefficient electron acceleration, whereas a much harder one would imply exceptionally efficient acceleration in which most of energy is in the highest-energy electrons.

The normalization of the electron injection is taken as a fraction of the jet power available for the acceleration of nonthermal electrons, $L_{\rm NT} = \eta_{\rm NT}L_{\rm j}$:

$$\int_{E_{\rm min}}^{E_{\rm max}} E\,Q(E)\,{\rm d}E = L_{\rm NT}. \tag{12}$$

The value of $E_{\rm min}$ is fixed here to 1 MeV for simplicity, although a very high $E_{\rm min}$, greater than 0.1−1 GeV for example, would affect the more compact radio emission. The value of $E_{\rm max}$ is obtained from electron acceleration constraints.

Electrons are accelerated gaining energy at a rate $\dot{E}_{\rm acc} = \eta_{\rm acc}eBc$, where $\eta_{\rm acc}$ is the acceleration efficiency, and e the electron charge. We take $\eta_{\rm acc} = 0.01$, which would correspond, for example, to acceleration by a high-velocity (nonrelativistic) shock under Bohm diffusion (Drury 1983). Low acceleration efficiencies would reduce the maximum energy of synchrotron photons, for which the photon energy is $\varepsilon \propto E^2$, much more than that of IC photons, produced in the Klein-Nishina regime at the highest spectral end, for which $\varepsilon \sim E$ (for IC in Thomson: $\varepsilon \propto E^2$).

Equating $\dot{E}_{\rm acc} = |\dot{E}|$ yields the maximum energy that electrons can reach in the accelerator (at $\boldsymbol{r_0}$): $E_{\rm acc}$. However, electrons can diffuse away from the accelerator before they reach $E_{\rm acc}$. Therefore, the diffusion timescale, $t_{\rm d} = r_{\rm j0}^2/2D_{\rm B}$, is also to be compared with the acceleration timescale, $t_{\rm acc} = E_{\rm d}/\dot{E}_{\rm acc}$, where $r_{\rm j0}$ is the characteristic jet base radius, and $D_{\rm B} = E_{\rm d}c/3qB$ is the diffusion coefficient assuming it proceeds in the Bohm regime. This gives a maximum energy value $E_{\rm d} = qBr_{\rm j}\sqrt{3\eta_{\rm acc}/2}$; for a larger diffusion coefficient D (still $\propto E$), $E_{\rm d} \propto \sqrt{D_{\rm B}/D}$. The $E_{\rm cut}$ value is obtained as the smallest among $E_{\rm acc}$ and $E_{\rm d}$, whereas $E_{\rm max}$ can be taken as several times $E_{\rm cut}$.

To compute the electron energy distribution along the jet, the latter is divided in cylindrical segments with increasing radius. The segment lengths are determined (with some exception; see below) by $v_{\rm j}$ multiplied by one fifth of the local shortest cooling time, which is derived from $t_{\rm loss} = E_{\rm max}/|\dot{E}(E_{\rm max})|$. In this way, the energy and spatial evolution of the fastest evolving electrons is reasonably well sampled. The magnetic field is assumed to be mostly perpendicular to the flow motion, typical for jets far from their origin, and therefore $B \propto r_{\rm j0}/r_{\rm j}$ under frozen conditions and constant $v_{\rm j}$. Each individual jet division is treated as a homogeneous emitter, which in the worse case is correct within a ∼3% error (spatial scales grow segment by segment by a factor $1 + l_{\rm max}/N/l_0 \sim 1.03$, where N is the number of segments).

For $\eta_{\rm B} \to 1$, synchrotron cooling times become very short ($t_{\rm loss} \ll t_{\rm adv}$, with $t_{\rm adv}$ being the advection timescale), and the large N makes calculations very long. In those extreme cases, we have adopted an approximation which consists in limiting N and then introducing a correction factor, $\times t_{\rm loss}/t_{\rm adv}$, to the injected population at the first segment. This simplified approach can overestimate the high energy part of the electron distribution by a factor around two, but speeds up calculations by several orders of magnitude for extreme B cases. Nevertheless, we indicate that $\eta_{\rm B} \to 1$ is too high, as in the region of interest the jet power is likely largely dominated by kinetic energy, and is considered here for illustrative purposes only.

To find the energy evolution up to a given segment, one computes the initial energy E_0 that electrons of energy E had when they were injected at the jet base. This is done iteratively by making small time steps back in time (and in space) to sample the energy evolution of electrons backwards from a given segment:

$$E_{i-1} = E_i - \dot{E}(E_i){\rm d}t. \tag{13}$$

Here, E_{i-1} is the energy that an electron had at a time $t - {\rm d}t$, and E_i is the electron energy at time t. We note that $E_{i-1} > E_i$ due to the negative sign of $\dot{E}$. The linear approximation used in Eq. (13) is only valid as long as $E_{i-1} - E_i \ll E_i$.

Once E_0 is known, the electron energy distribution at the jet base, $N_0(E_0)$, of a segment k with length dl_k, is computed as

$$N_0(E_0) = Q(E_0)\,t_k^{\rm adv}, \tag{14}$$

with $t_k^{\rm adv} = dl_k/v_{\rm j}$ (if small enough; otherwise $t_k^{\rm adv} \to t_{\rm loss}$). The electron energy distribution at a segment k is computed from the distribution when at the segment k–1:

$$N_k(E_k) = N_{k-1}(E_{k-1})\frac{\dot{E}_k(E_{k-1})}{\dot{E}_k(E_k)}, \tag{15}$$

where E_k and E_{k-1} are energies related by Eq. (13) in segments k and k–1, respectively[2]. By applying this procedure down to the jet base, one gets the general expression for the electron energy distribution at each jet segment:

$$N_k(E_k) = N_0(E_0)\prod_{i=k}^{1}\frac{\dot{E}_i(E_{i-1})}{\dot{E}_i(E_i)}, \tag{16}$$

keeping in mind that $E_k \gtrsim m_e c^2$ and $E_0 < E_{\max}$.

3.3. Emission of radiation

The power per photon energy unit radiated by an electron of energy E via synchrotron emission is computed following (Pacholczyk 1970)

$$P_\varepsilon(E) = \frac{\sqrt{3}e^3 B\sin\theta}{hm_{\rm e}c^2}F(x), \tag{17}$$

where θ is the pitch angle between the electron velocity and B vectors, and $x = \varepsilon/\varepsilon_{\rm c}$, with $\varepsilon_{\rm c}$ being the characteristic synchrotron photon energy defined as

$$\varepsilon_{\rm c} = \frac{3}{4\pi}\frac{ehB\sin\theta}{m_e^3c^5}E^2. \tag{18}$$

The function $F(x)$ includes an integral of the $K_{5/3}(\zeta)$ Bessel function, but in this work we adopt an approximation valid within a few percent error in the range $0.1 < x < 10$ (e.g., Melrose, 1980; Aharonian 2004):

$$F(x) = x\int_x^\infty K_{5/3}(\zeta)\mathrm{d}\zeta \approx 1.85x^{1/3}e^{-x}. \tag{19}$$

The geometry of $\boldsymbol{B}$ is not well known, so an isotropic distribution in the fluid frame is assumed, taking for simplicity $B\sin\theta \approx \sqrt{< B^2 >} = B\sqrt{2/3}$. The synchrotron spectral energy distribution (SED) for an isotropic population of electrons with distribution $N(E)$ is:

$$\varepsilon\, L_\varepsilon^{\rm sync} = \varepsilon\int_0^\infty P_\varepsilon(E)N(E)\mathrm{d}E. \tag{20}$$

The IC emission is computed considering that relativistic electrons interact with a beam of photons with energy ε_0. The IC kernel for an angle θ with respect to the initial beam direction is (Aharonian & Atoyan 1981):

$$\frac{\mathrm{d}^2N(\theta,\varepsilon)}{\mathrm{d}\varepsilon\,\mathrm{d}\Omega} = \frac{3\sigma_T m_e^2c^4}{16\pi\varepsilon_0E^2}\left[1+\frac{z^2}{2(1-z)}-\frac{2z}{b_\theta(1-z)}+\frac{2z^2}{b_\theta^2(1-z)^2}\right], \tag{21}$$

where $b_\theta = 2(1-\cos\theta)\varepsilon_0E/m_e^2c^4$, $z = \varepsilon/E$, and ε can vary in the limits $\varepsilon_0 < \varepsilon < Eb_\theta/(1+b_\theta)$. The (apparent) IC SED at a given direction is obtained by convolving Eq. (21) with the electron energy distribution $N(E)$ and the energy distribution density of stellar photons $n(\varepsilon_0)$:

$$\varepsilon\, L_\varepsilon^{\rm IC} = 4\pi c\varepsilon^2\int_0^\infty \mathrm{d}E\int_0^\infty \mathrm{d}\varepsilon_0\frac{\mathrm{d}^2N(\theta,\varepsilon)}{\mathrm{d}\varepsilon\,\mathrm{d}\Omega}N(E)n(\varepsilon_0). \tag{22}$$

Target photons other than those of stellar origin, like those coming from an accretion disk, are unimportant for the jet regions studied in this work. Synchrotron self-Compton is also negligible even when one assumes that most of the nonthermal energy is released as synchrotron radiation.

3.4. Absorption of radiation

The main absorption mechanism considered in this work is electron-positron pair production from gamma rays interacting with stellar photons. The cross section for this process is (Gould & Schréder 1967)

$$\sigma_{\gamma\gamma} = \frac{3}{16}\sigma_{\rm T}(1-\beta^2)\left[(3-\beta^4)\ln\left(\frac{1+\beta}{1-\beta}\right)-2\beta(2-\beta^2)\right], \tag{23}$$

where

$$\beta = \sqrt{1-\frac{2m_e^2c^4}{\varepsilon\varepsilon_0(1-\cos\theta_{\gamma\gamma})}}, \tag{24}$$

ε and ε_0 are the energies of the high-energy and stellar photons, respectively, and $\theta_{\gamma\gamma}$ is the angle between their propagation directions.

The optical depth of gamma-ray absorption is (Gould & Schréder 1967)

$$\tau_{\gamma\gamma}(\varepsilon) = \int_0^l \mathrm{d}l\,[1-\cos\theta_{\gamma\gamma}(l)]\int_{\varepsilon_{0,\min}}^\infty \mathrm{d}\varepsilon_0\, n(\varepsilon_0,l)\sigma_{\gamma\gamma}(\varepsilon_0,\varepsilon,\theta_{\gamma\gamma}), \tag{25}$$

where l is the distance to the observer covered by the gamma ray, and $\varepsilon_{0,\min} = 2m_e^2c^4/\varepsilon(1-\cos\theta_{\gamma\gamma})$ is the minimum energy of the gamma rays absorbed by the target stellar photons.

For the cases studied here, synchrotron self-absorption is estimated in radio by computing the optically thick-to-optically thin transition frequency (e.g., Bosch-Ramon 2009), and is found to be negligible in general; it has therefore not been included in the calculations. Free-free radio absorption in the stellar wind is also negligible at the scales of the emitting region. Nonthermal ultraviolet (UV) photons are also strongly absorbed on their way to the observer, but we have not included this effect as UV photons from the star would be largely dominant in any case. In a very compact system with a very powerful stellar wind, such as, for example, Cygnus X-3, radio absorption could still be an issue at a distance $D_\star$ from the binary, although we defer specific source studies for future work.

4. Results

The results are obtained using the parameter values given in Table 1, together with the sets of values presented in Table 2 for i, the orbital phase α, and $\eta_{\rm B}$, whose variations have strong effects on the nonthermal emission. Considering the free parameters, the electron energy distribution is affected only by $\eta_{\rm B}$, whereas SEDs, light curves, and the emitter geometry are also affected by α and i. Most SEDs are calculated for $\alpha = 0.25$ as a typical example, which corresponds to one of the orbit nodes. Varying α, we also compute some SEDs and IC light curves to illustrate orbital variations of this component. A comparison of SEDs and light curves is done between the extended and the point-like (one-zone) emitter, to check which features arise when an extended (helical) jet is considered. Finally, maps at 5 GHz are computed to illustrate the expected radio morphologies from a helical jet.

4.1. Nonthermal electrons

The electron energy distribution for the jet[3], $\times E^2$ to emphasize the energy content at different energy scales, is shown in Fig. 2

---

[2] We note that Eq. (15) should be corrected for segment length and velocity if they are not constant.

[3] The jet and counter-jet electron energy distributions are equal in our model.

Table 2. Values adopted for different parameters.

Parameter	Values
η_B	10^{-4}, 10^{-2}, 1
i	30°, 60°
α	0–1

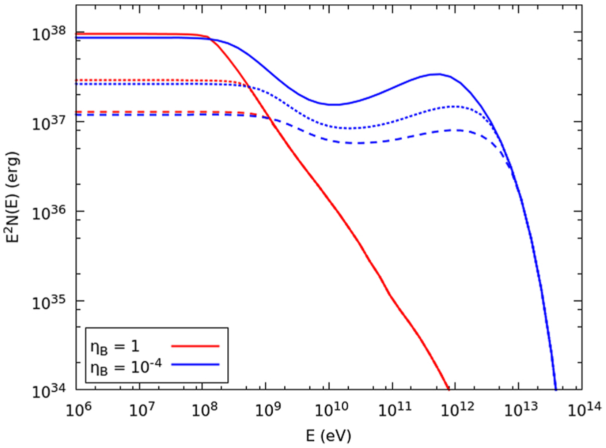

Fig. 2. Electron energy distribution of the jet $\times E^2$ up to $D_\star$ (dashed lines), $3D_\star$ (dotted lines) and $25D_\star$ (the whole jet; solid lines), for $\eta_B = 10^{-4}$ and 1.

for $\eta_B = 10^{-4}$ and 1, and up to three different jet lengths starting from $\boldsymbol{r_0}$: $D_\star$, $3D_\star$ and $25D_\star$ (whole jet). As seen in the figure, a significant fraction of electrons below ~1 GeV survive beyond $3D_\star$, and for the lowest B, TeV electrons can also reach a larger distance from the binary (see also, e.g., Khangulyan et al. 2008). As expected, the energy distribution is steep for electron energies dominated by synchrotron and Thomson IC losses. When IC dominates, the SED becomes harder at ~10 GeV because of the Thomson-to-Klein-Nishina transition of the electron distribution, getting steeper again only at the highest energies due to synchrotron losses (and the effect of $E_{\rm cut}$).

4.2. Spectral energy distribution

Figure 3 shows the SEDs of the synchrotron and the IC emission for the same cases studied in Fig. 2, showing now within each panel the jet and the counter-jet contributions separately. An inclination of $i = 60°$ is adopted, and $\alpha = 0.25$. As expected from the severe drop in radiation efficiencies, the contribution to the emission of the regions beyond $3D_\star$ is minor for all the cases studied, although radio emission is still non-negligible beyond that distance, as seen in Sect. 4.5. It is worth noting that most of the IC radiation comes from the counter-jet because of the larger IC θ-values. Doppler boosting is negligible for the adopted $v_{\rm j}$-value and is not included.

The effect of the magnetic field on the synchrotron and IC SEDs is shown in Fig. 4 for $i = 30°$ and $\alpha = 0.25$, and for the jet and the counter-jet separately. As expected, the synchrotron to IC luminosity ratio depends strongly on η_B. Figure 4 also shows the effect of gamma-ray absorption (stronger for $i = 30°$ than for 60°), which is quite modest given the relatively large distances from the star and the α-value considered in this plot.

Figure 5 shows the effect of the orbital phase on the IC spectrum. With $i = 30°$ and $\eta_B = 10^{-2}$, the SEDs for $\alpha = 0, 0.25$ and 0.5 are plotted. For $\alpha = 0.5$, which corresponds to the CO superior conjunction (i.e., the CO is behind the star), there is a drop of up to five orders of magnitude in the counter-jet emission above 10 GeV due to gamma-ray absorption, which makes the jet dominate the radiation output in this range, effectively smoothing the overall impact of gamma-ray absorption for this orbital phase.

4.3. Light curve

Figure 6 shows the IC light curves for $\eta_B = 10^{-2}$. The peak around $\alpha = 0.5$ and 0.1–100 GeV for $i = 60°$ is explained by the larger IC θ-angles, and the small dip for $i = 30°$ manifests some level of gamma-ray absorption, which starts at ~10 GeV in a relatively hard IC SED (see Fig. 5). For energies >100 GeV, absorption has a very strong impact on the fluxes by a factor of several, although the jet component smoothens somewhat the light curve around $\alpha = 0.5$ (superior conjunction of the CO) because of reduced gamma-ray absorption due to a smaller $\theta_{\gamma\gamma}$-value (see Fig. 5). On the other hand, the counter-jet still leads to significant IC fluxes around $\alpha = 0$ (inferior conjunction; see Fig. 5), unlike an emitter located very close to the CO, which would lead to stronger differences in flux.

4.4. Extended versus one-zone emitter

Figure 7 shows a comparison between the SEDs of an extended (helical) jet and a one-zone emitter, for the jet and the counter-jet, for $i = 30°$, $\alpha = 0.25$, and $\eta_B = 10^{-2}$. The one-zone emitter is assumed to be just one segment located at $\boldsymbol{r_0}$ and of length $D_\star/3$, which sets the electron escape time. Because of fast radiation losses, the one-zone approximation works well in the high-energy part of the synchrotron and IC SEDs, as expected. Qualitatively, the extended and the one-zone emitters look quite similar, although differences of up to a factor of 2 are seen, mainly but not only in the jet synchrotron and IC components at low energies, as low-energy electrons escaped from the one-zone region are still radiatively relevant. We note that inaccurate source knowledge and model simplifications imply systematic uncertainties likely larger than a factor of 2, which means that the SED alone cannot help to discriminate a helical jet model from that of a one-zone emitter.

Figure 8 compares the light curves of an extended and a one-zone emitter in the cases presented in Fig. 6. The fluxes are larger (lower) for the extended emitter for 0.1–100 GeV (>100 GeV), and are symmetric around $\alpha = 0.5$. The different behavior between the two energy bands is caused by the fact that electrons emitting >100 GeV photons via IC reach farther from the star than those emitting 0.1–100 GeV photons (see Sect. 4.1), both for the counter-jet and the jet, decreasing the IC flux as they meet a more diluted target photon field. We note that for higher jet powers, the helical jet would start further away (see Eqs. (1) and (4)), in which case the light curve would become asymmetric for the extended jet.

4.5. Radio emission

Radio sky maps at 5 GHz for $\eta_B = 10^{-2}$ and different orbital phases are shown in Figs. 9 and 10 for $i = 30°$ and $i = 60°$, respectively. These maps are obtained following three steps: first, the helical jet structure is projected into the plane of the sky. Subsequently, the emission from each segment is convolved with a Gaussian with standard deviation $\sigma = r_{\rm j}/2$ to approximately distribute the emission over the actual sky-projected area of

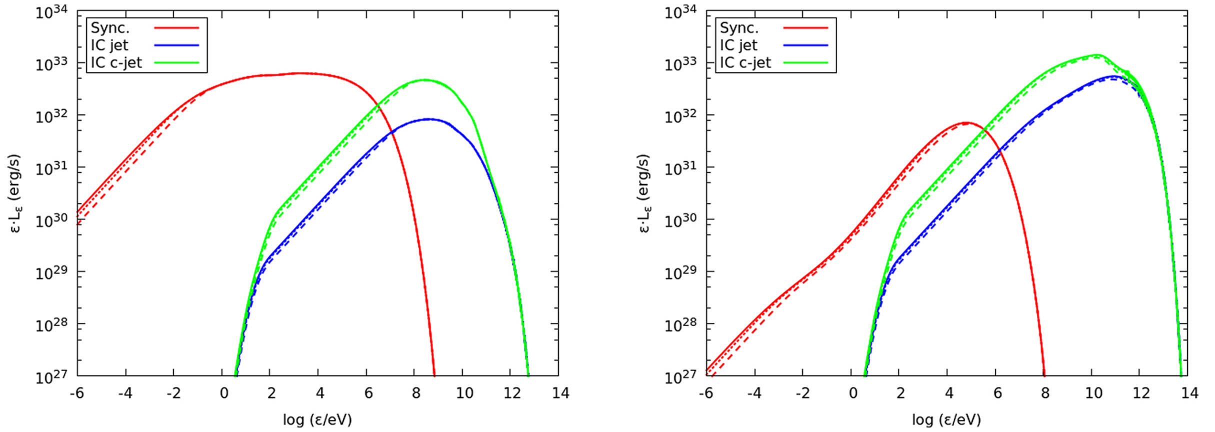

Fig. 3. Synchrotron and IC SEDs of the jet (blue) and the counter-jet (green), for $i = 60°$ and $\alpha = 0.25$, up to $D_\star$ (dashed lines), $3D_\star$ (dotted lines), and $25D_\star$ (the whole jet; solid lines), for $\eta_B = 10^{-4}$ (*right panel*) and 1 (*left panel*).

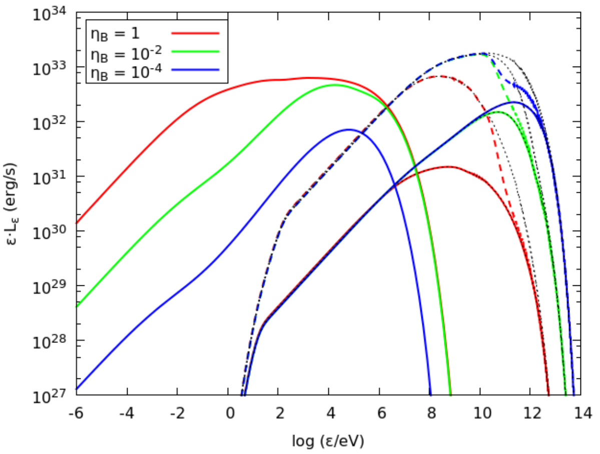

Fig. 4. Synchrotron and IC SEDs of the jet (solid lines) and the counter-jet (dashed lines), for $i = 30°$ and $\alpha = 0.25$, and $\eta_B = 10^{-4}$ (blue lines), 10^{-2} (green lines), and 1 (red lines). The unabsorbed IC emission is also shown (black dotted lines).

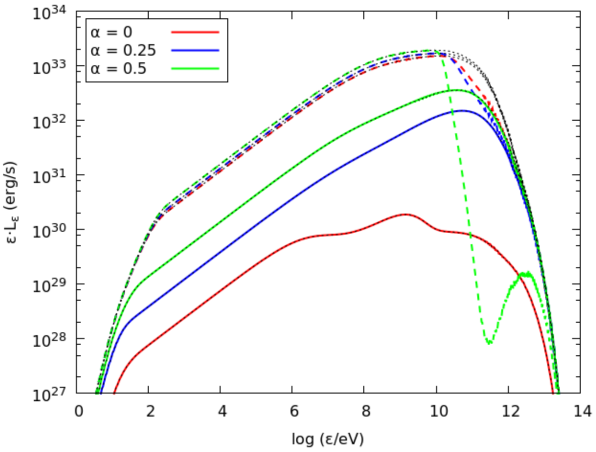

Fig. 5. IC SEDs of the jet (solid lines) and the counter-jet (dashed lines), for $i = 30°$, $\eta_B = 10^{-2}$, $\alpha = 0$ (red lines), 0.25 (blue lines) and 0.5 (green lines). The unabsorbed IC emission is also shown (black dotted lines).

each segment. Finally, this emission is convolved again with a Gaussian with *FWHM* = 1 mas in order to mimic the response of a radio, very long baseline interferometer (see, e.g., Walker 1995 for a VLBA description). With the sensitivity of current instrumentation, typically of a few tens of μJy beam^{-1}, the extended emission could be resolved, but only from the parts of the jet that are relatively close to its base. The bending of the jet appears more dramatic the smaller the inclination due to projection effects. The total received flux for each map is 7.4 mJy. As the flux increases proportionally to $\eta_{\rm NT}$, one could detect the jet up to larger distances for higher $\eta_{\rm NT}$. To illustrate this, Fig. 11 shows a comparison between two sky maps with different nonthermal energy fractions, $\eta_{\rm NT} = 10^{-2}$ and $\eta_{\rm NT} = 5 \times 10^{-2}$. We note that the radio fluxes also depend on $\eta_{\rm B}$ as $\propto \eta_{\rm B}^{3/4}$.

5. Summary and discussion

As argued by Bosch-Ramon & Barkov (2016), a nonballistic helical jet region is the likely outcome of a HMMQ jet interacting with the stellar wind under the effect of orbital motion. In the present work, we have shown that such a region is predicted to produce significant fluxes from radio to gamma rays if $L_{\rm NT} \sim \eta_{\rm NT} L_{\rm j} \gtrsim 10^{34} \eta_{\rm NT,-2}$ erg s^{-1}, for a source at a few kiloparsecs. These significant fluxes are explained by the high synchrotron and IC efficiencies at the helical jet onset location, $\boldsymbol{r_0}$, for typical HMMQ $L_\star$-values. Since realistic $\eta_{\rm B}$-values are expected to be well below equipartition with the radiation field, the IC component is likely to dominate the nonthermal emission, peaking around 10 GeV. Specific gamma-ray light curve features are also predicted: a non-negligible impact of gamma-ray absorption, combined with angular effects for this process and IC. Peculiar changing radio morphologies, which can trace the jet helical structure, are expected as well.

We note that hydrodynamical instabilities and wind-jet mixing make our results mostly valid for the inner helical jet region, say up to a few $D_\star$. Beyond that point, the jet helical geometry is likely to become blurred, eventually turning into a bipolar, relatively wide, and collimated supersonic outflow; a mixture of jet and wind material. Although the flow may still be mildly relativistic for very energetic ejections, in general the resulting "jet"

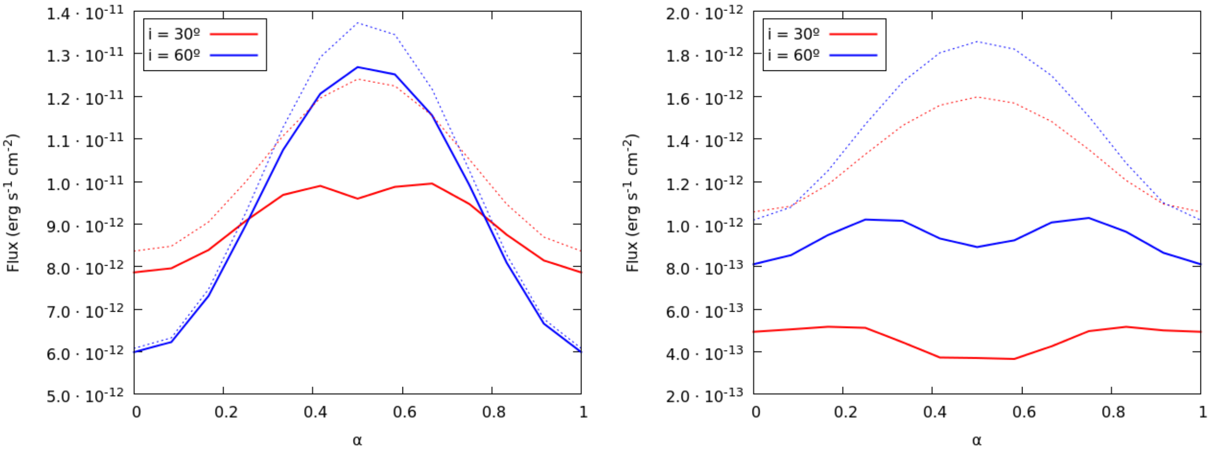

Fig. 6. Light curves of IC emission (jet + counter-jet) at 0.1–100 GeV (*left panel*) and >100 GeV (*right panel*), for $i = 30°$ (red lines) and 60° (blue lines), and $\eta_B = 10^{-2}$. The unabsorbed light curves are also shown (dotted lines). The CO is in inferior (superior) conjunction with the star when the orbital phase is 0 (0.5).

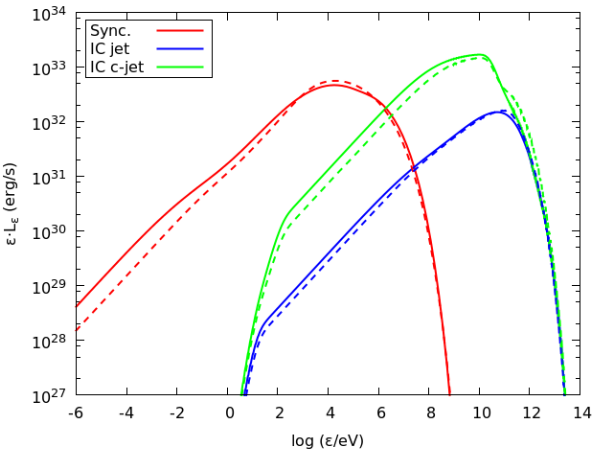

Fig. 7. Comparison of the (absorbed) SEDs of an extended (helical) jet (solid lines) and a one-zone emitter (dashed lines) for the jet and the counter-jet for $i = 30°$, $\alpha = 0.25$, and $\eta_B = 10^{-2}$.

is expected to be much faster than the stellar wind, but nonrelativistic.

Our results are based on a number of strong simplifications, in particular regarding the stability of the helical jet. Therefore, detailed numerical simulations of the jet-wind interaction on middle to large scales are necessary for more accurate predictions. Nevertheless, despite the simplifications adopted, the main features of the scenario are expected to be rather robust, at least at a semi-quantitative level. These are: non-negligible fluxes; specific light curves characterized by the value of $\boldsymbol{r_0}$, the interplay of jet and counter-jet emission, and angular IC and gamma-ray absorption effects; and curved jet radio morphologies with characteristic orbital evolution. This is so because the first- or even zeroth-order level of the dynamical, radiative, and geometrical effects involved are taken into account in our calculations.

Two important system parameters, eccentricity and $d_{\rm O}$, have been assumed constant in our calculations. Despite being difficult to ascertain the impact of eccentricity in a HMMQ without numerical calculations, simulations of pulsar-star wind colliding in eccentric binaries (Barkov & Bosch-Ramon 2016; Bosch-Ramon et al. 2017) suggest that the effect of eccentricity should be important only for rather eccentric binaries. In that case, the nature of the interaction structure may not be helical at all, being not only strongly asymmetric, and inclined towards the apastron side of the orbit, but also likely much more sensitive to disruption. The value of $d_{\rm O}$, and thus P, may also change. This would leave the helical jet geometry unaffected: both the helical vertical step and $x_{\rm turn}$ are $\propto P \propto d_{\rm O}^{3/2}$. On the other hand, the luminosity would change as $\propto P^{-1} \propto d_{\rm O}^{-3/2}$ except for emission produced under the fast radiative cooling regime of electrons (in our setup the highest-energy end of the synchrotron and IC emission), which is independent of $d_{\rm O}$. The helical jet radiation in a very wide system would be hardly detectable unless the flow is slow, which allows electrons to radiate more energy. On the other hand, in a very compact system, radio emission would be hard to resolve for a slow helical jet flow, as the source would be too small.

The emission on the scales of the binary, produced for instance by jet internal shocks or by the first wind-induced recollimation shock in the jet (stage 2), could be important. In which case: (i) assuming that the same nonthermal luminosity is injected in both regions, the radio emission from the binary scales would be strongly absorbed via synchrotron self-absorption and wind free-free absorption; and (ii) the X- and gamma-ray emission would be at a similar level if produced in the fast radiation cooling regime, and at a higher level otherwise because of the higher B-value and IC-target density. Gamma-ray absorption could however strongly attenuate the gamma-ray luminosity >100 GeV for most of the orbit. Therefore, the helical jet could contribute significantly to the overall nonthermal radiation of HMMQ, and particularly in radio and >100 GeV, even if electrons are also accelerated closer to the jet base. This was the main motivation for this work: to perform a first exploration of specific radiation features of the helical jet region, so that it could be disentangled from the other emitting sites. For the HMMQ Cygnus X-1 and Cygnus X-3, their uncertain wind and jet parameters make it difficult to make concrete predictions; for example, a non-ballistic jet region may not form at

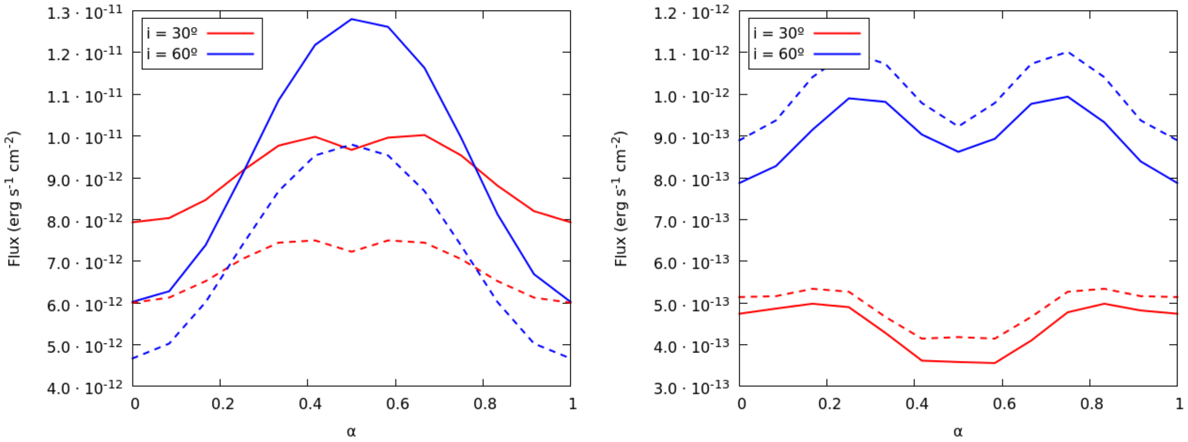

Fig. 8. As in Fig. 6 but comparing the extended jet (solid lines) and the one-zone case (dashed lines), and for the absorbed gamma-ray component only.

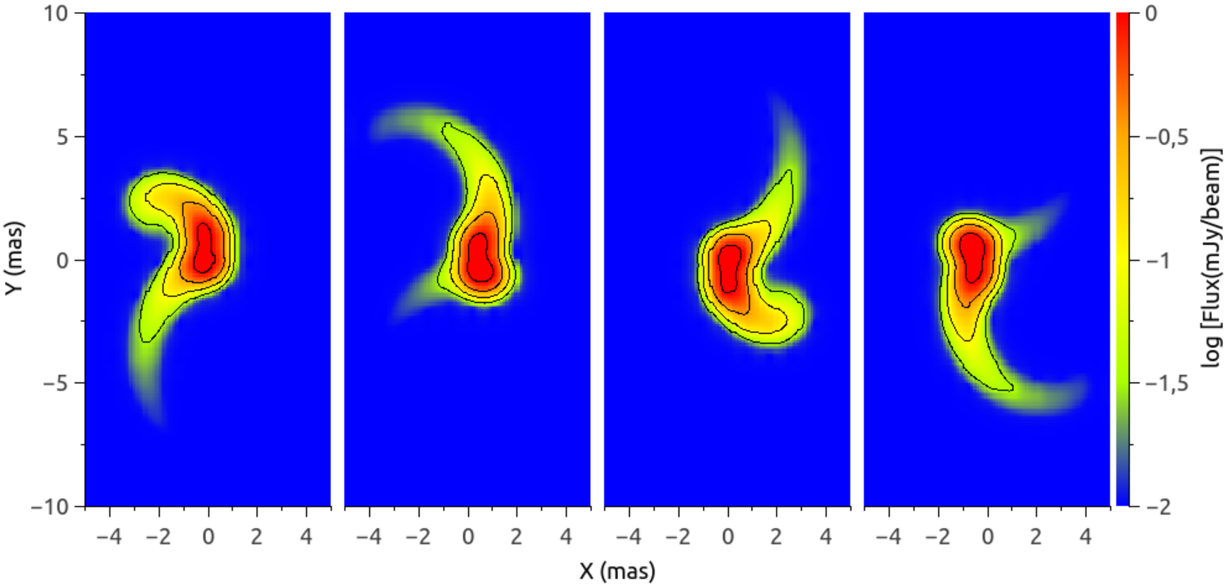

Fig. 9. Sky maps at 5 GHz for $i = 30°$, $\eta_B = 10^{-2}$, and orbital phases of 0, 0.25, 0.5 and 0.75 *from left to right*. Contour levels correspond to fluxes of 0.032, 0.1, 0.32 and 1 mJy beam^{-1}. The beam size is 1 mas.

all (Yoon et al. 2016; Bosch-Ramon & Barkov 2016 and references therein), and an individual detailed source analysis is out of the scope of this work. In spite of this, our findings are not in contradiction with the radio morphology and the gamma-ray light curves of these sources (e.g., Stirling et al. 2001; Mioduszewski et al. 2001; Miller-Jones et al. 2004; Zanin et al. 2016; Zdziarski et al. 2018). Future detailed modeling together with deep, high-resolution radio observations and the high-energy light curves could provide hints of helical jet emission.

The wind-jet interaction in HMMQ resembles, to a significant extent, the wind-wind interaction in high-mass binaries hosting young pulsars. The latter sources are probably extended mostly on the orbital plane and along the orbit semi-major axis, whereas the bipolar helical-jet structure is focused mostly in a direction perpendicular to the orbit plane (Bosch-Ramon et al. 2015, 2017; Bosch-Ramon & Barkov 2016). Nevertheless, the interactions of the stellar wind with a relativistic pulsar wind or jet, on binary, middle, and large scales, share many qualitative properties, and this may mask a fundamentally different engine accretion vs. a pulsar wind when observing sources of yet unknown CO. These similarities are: extended radio structures with orbital evolution found at mas scales; strong radio absorption on the binary scales; similar hydrodynamics, and therefore impact of instabilities, adiabatic losses, and Doppler boosting effects[4], for the shocked flows outside the binary region; and gamma-ray light curves

---

[4] The much higher energy per particle of shocked pulsar winds can lead to stronger Doppler boosting effects than in a HMMQ jet, although mass-loading smoothens this difference.

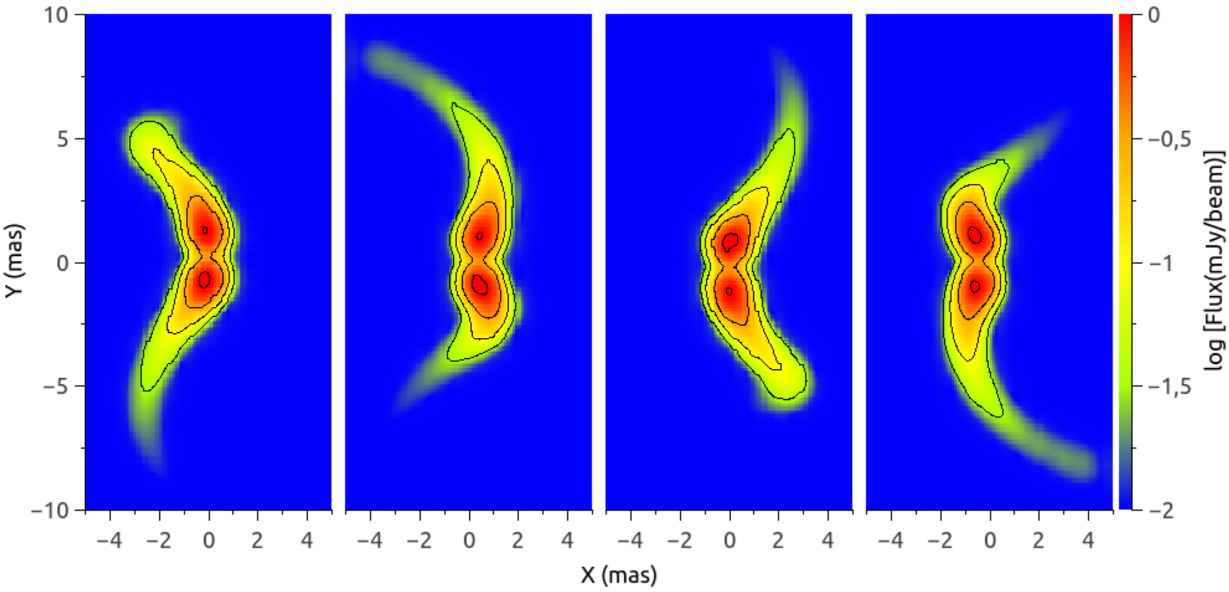

Fig. 10. As in Fig. 9 but for $i = 60°$.

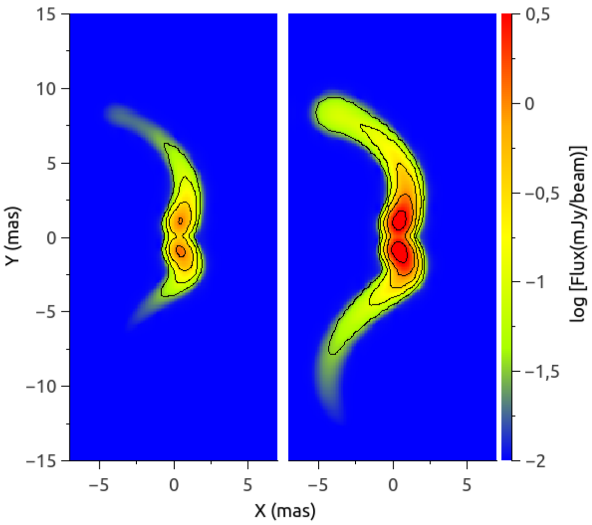

Fig. 11. Sky maps at 5 GHz for $i = 60°$, $\alpha = 0.25$, $\eta_{\rm NT} = 10^{-2}$ (*left*) and 5×10^{-2} (*right*). Contour levels are (mJy beam): 0.032, 0.1, 0.32, 1, 3.2. The beam size is 1 mas.

strongly affected by IC and gamma-ray absorption angular effects, in a likely extended/multi-zone emLitter. Radio observations, high-quality multiwavelength data, numerical simulations, and realistic radiation calculations (e.g., Aharonian et al. 2006; Perucho & Bosch-Ramon 2008, 2012; Albert et al. 2009; Fermi LAT Collaboration 2009; Perucho et al. 2010; Moldón et al. 2011b,a, 2012; Bosch-Ramon et al. 2015, 2017; Dubus et al. 2015; Zanin et al. 2016; Yoon & Heinz 2015; Yoon et al. 2016; de la Cita et al. 2017; Wu et al. 2018; Barkov & Bosch-Ramon 2018) are therefore needed to characterize radiation scenarios in high-mass binaries with unknown CO, such that empirical observables can help to disentangle the CO nature.

Acknowledgements. We would like to thank the referee for a constructive and useful report that helped to improve the manuscript. We acknowledge support by the Spanish Ministerio de Economía y Competitividad (MINECO/FEDER, UE) under grants AYA2013-47447-C3-1-P and AYA2016-76012-C3-1-P, with partial support by the European Regional Development Fund (ERDF/FEDER), MDM-2014-0369 of ICCUB (Unidad de Excelencia "María de Maeztu"), and the Catalan DEC grant 2017 SGR 643. EM acknowledges support from MINECO through grant BES-2016-076342.

References

Abell, G. O., & Margon, B. 1979, Nature, 279, 701
Aharonian, F. A. 2004, Very High Energy Cosmic Gamma Radiation: A Crucial Window on the Extreme Universe (World Scientific Publishing Co.)
Aharonian, F. A., & Atoyan, A. M. 1981, Ap&SS, 79, 321
Aharonian, F., Akhperjanian, A. G., Bazer-Bachi, A. R., et al. 2006, A&A, 460, 743
Albert, J., Aliu, E., Anderhub, H., et al. 2009, ApJ, 693, 303
Araudo, A. T., Bosch-Ramon, V., & Romero, G. E. 2009, A&A, 503, 673
Barkov, M. V., & Bosch-Ramon, V. 2016, MNRAS, 456, L64
Barkov, M. V., & Bosch-Ramon, V. 2018, MNRAS, 479, 1320
Begelman, M. C., King, A. R., & Pringle, J. E. 2006, MNRAS, 370, 399
Bosch-Ramon, V. 2009, A&A, 493, 829
Bosch-Ramon, V. 2013, Eur. Phys. J. Web Conf., 61, 03001
Bosch-Ramon, V., & Barkov, M. V. 2016, A&A, 590, A119
Bosch-Ramon, V., & Khangulyan, D. 2009, Int. J. Mod. Phys. D, 18, 347
Bosch-Ramon, V., Barkov, M. V., & Perucho, M. 2015, A&A, 577, A89
Bosch-Ramon, V., Barkov, M. V., Mignone, A., & Bordas, P. 2017, MNRAS, 471, L150
de la Cita, V. M., Bosch-Ramon, V., Paredes-Fortuny, X., Khangulyan, D., & Perucho, M. 2017, A&A, 598, A13
Drury, L. O. 1983, Rep. Prog. Phys., 46, 973
Dubus, G., Lamberts, A., & Fromang, S. 2015, A&A, 581, A27
Fermi LAT Collaboration (Abdo, A. A., et al.) 2009, Science, 326, 1512
Gould, R. J., & Schréder, G. P. 1967, Phys. Rev., 155, 1408
Khangulyan, D., Aharonian, F., & Bosch-Ramon, V. 2008, MNRAS, 383, 467
Khangulyan, D., Aharonian, F. A., & Kelner, S. R. 2014, ApJ, 783, 100
Longair, M. S. 1981, High Energy Astrophysics (Cambridge University Press)
Luque-Escamilla, P. L., Martí, J., & Martínez-Aroza, J. 2015, A&A, 584, A122
Melrose, D. B. 1980, Plasma Astrophysics. Nonthermal Processes in Diffuse Magnetized Plasmas (Gordon & Breach)
Miller-Jones, J. C. A., Blundell, K. M., Rupen, M. P., et al. 2004, ApJ, 600, 368
Mioduszewski, A. J., Rupen, M. P., Hjellming, R. M., Pooley, G. G., & Waltman, E. B. 2001, ApJ, 553, 766

Moldón, J., Johnston, S., Ribó, M., Paredes, J. M., & Deller, A. T. 2011a, ApJ, 732, L10
Moldón, J., Ribó, M., & Paredes, J. M. 2011b, A&A, 533, L7
Moldón, J., Ribó, M., & Paredes, J. M. 2012, A&A, 548, A103
Muijres, L. E., Vink, J. S., de Koter, A., Müller, P. E., & Langer, N. 2012, A&A, 537, A37
Owocki, S. P., Romero, G. E., Townsend, R. H. D., & Araudo, A. T. 2009, ApJ, 696, 690
Pacholczyk, A. G. 1970, in Radio Astrophysics. Nonthermal Processes in Galactic and Extragalactic Sources (W. H. Freeman & Company)
Perucho, M., & Bosch-Ramon, V. 2008, A&A, 482, 917
Perucho, M., & Bosch-Ramon, V. 2012, A&A, 539, A57
Perucho, M., Bosch-Ramon, V., & Khangulyan, D. 2010, A&A, 512, L4
Romero, G. E., & Orellana, M. 2005, A&A, 439, 237
Romero, G. E., Torres, D. F., Kaufman Bernadó, M. M., & Mirabel, I. F. 2003, A&A, 410, L1
Sell, P. H., Heinz, S., Calvelo, D. E., et al. 2010, ApJ, 719, L194
Stirling, A. M., Spencer, R. E., de la Force, C. J., et al. 2001, MNRAS, 327, 1273
Stirling, A. M., Jowett, F. H., Spencer, R. E., et al. 2002, MNRAS, 337, 657
Walker, R. C. 1995, in Very Long Baseline Interferometry and the VLBA, eds. J. A. Zensus, P. J. Diamond, & P. J. Napier, ASP Conf. Ser., 82, 133
Wu, Y. W., Torricelli-Ciamponi, G., Massi, M., et al. 2018, MNRAS, 474, 4245
Yoon, D., & Heinz, S. 2015, ApJ, 801, 55
Yoon, D., Zdziarski, A. A., & Heinz, S. 2016, MNRAS, 456, 3638
Zanin, R., Fernández-Barral, A., de Oña Wilhelmi, E., et al. 2016, A&A, 596, A55
Zdziarski, A. A., Malyshev, D., & Dubus, G. 2018, MNRAS, 479, 4399

3

A RELATIVISTIC MODEL FOR MICROQUASAR JETS UNDER THE INFLUENCE OF A STRONG STELLAR WIND

This Chapter contains the published version of Molina et al. (2019, A&A, 629, A129).

The work presented here generalizes what was done in Chapter 2 mainly by including relativistic effects. This allows us to study the jet-wind interaction in HMMQs at the scales of the binary system and below, where the plasma in the jets moves at a large fraction of the speed of light. The trajectory is computed considering momentum transfer from the stellar wind to the jets, which results in bent jets close to the binary system that start acquiring a helical shape at distances of a few orbital separations. Moreover, within the binary system, the jets are likely to suffer a recollimation shock where their lateral pressure is overcome by the wind pressure (e.g., Perucho et al. 2010), which may trigger efficient particle acceleration.

From the radiative point of view, given the proximity of the studied regions to the star, absorption processes involving the latter become important. This is the case of gamma-gamma absorption, which is drastic for some orbital phases, and free-free absorption of photons by the stellar wind ions, which prevents any radio emission from the inner jet regions from reaching the observer.

The results of this improved jet-wind model for HMMQs include strong orbital modulation of the gamma-ray emission owing to Doppler boosting and absorption. Since local acceleration is only assumed to happen at the recollimation shock, very close to the CO, emission is highly concentrated at the binary scales except for microwave and infrared frequencies. Even so, significant differences with respect to a scenario with a straight, unbent jet are found, especially in the form of asymmetries in the light curve (LC) around the inferior conjunction of the CO.

A&A 629, A129 (2019)
https://doi.org/10.1051/0004-6361/201935960

Astronomy & Astrophysics

A model for high-mass microquasar jets under the influence of a strong stellar wind

E. Molina[1], S. del Palacio[2], and V. Bosch-Ramon[1]

[1] Departament de Física Quàntica i Astrofísica, Institut de Ciències del Cosmos (ICCUB), Universitat de Barcelona (IEEC-UB), Martí i Franquès 1, 08028 Barcelona, Spain
e-mail: `emolina@fqa.ub.edu, vbosch@fqa.ub.edu`
[2] Instituto Argentino de Radioastronomía (CCT-La Plata, CONICET; CICPBA), C.C.5, 1894 Villa Elisa, Argentina
e-mail: `sdelpalacio@iar.unlp.edu.ar`

Received 27 May 2019 / Accepted 21 August 2019

ABSTRACT

Context. High-mass microquasars (HMMQs) are systems from which relativistic jets are launched. At the scales of several times the binary system size, the jets are expected to follow a helical path caused by the interaction with a strong stellar wind and orbital motion. Such a trajectory has its influence on the non-thermal emission of the jets, which also depends strongly on the observing angle due to Doppler boosting effects.

Aims. We explore how the expected non-thermal emission of HMMQ jets at small scales is affected by the impact of the stellar wind and the orbital motion on the jet propagation.

Methods. We studied the broadband non-thermal emission, from radio to gamma rays, produced in HMMQ jets up to a distance of several orbital separations, taking into account a realistic jet trajectory, different model parameters, and orbital modulation. The jet trajectory is computed by considering momentum transfer with the stellar wind. Electrons are injected at the position where a recollimation shock in the jets is expected due to the wind impact. Their distribution along the jet path is obtained assuming local acceleration at the recollimation shock, and cooling via adiabatic, synchrotron, and inverse Compton processes. The synchrotron and inverse Compton emission is calculated taking into account synchrotron self-absorption within the jet, free-free absorption with the stellar wind, and absorption by stellar photons via pair production.

Results. The spectrum is totally dominated by the jet over the counter-jet due to Doppler boosting. Broadband emission from microwaves to gamma rays is predicted, with radio emission being totally absorbed. This emission is rather concentrated in the regions close to the binary system and features strong orbital modulation at high energies. Asymmetric light curves are obtained owing to the helical trajectory of the jets.

Conclusions. The presence of helical shaped jets could be inferred from asymmetries in the light curves, which become noticeable only for large jet Lorentz factors and low magnetic fields. Model parameters could be constrained if accurate phase-resolved light curves from GeV to TeV energies were available. The predictions for the synchrotron and the inverse Compton radiation are quite sensitive of the parameters determining the wind-jet interaction structure.

Key words. X-rays: binaries – radiation mechanisms: non-thermal – relativistic processes – stars: winds, outflows – stars: massive

1. Introduction

Microquasars are binary systems consisting of a compact object (CO), either a black hole or a neutron star, that launches relativistic jets powered by accretion of matter from a companion star. When the companion is a massive star, these systems are called high-mass microquasars (HMMQs) and accretion onto the CO takes place as the latter captures a fraction of the stellar wind. This mechanism is compatible with the presence of an accretion disk around the CO (El Mellah et al. 2019b), which is a necessary condition for jet formation. In HMMQs, interaction between the jets and the stellar wind may play an important role in both the propagation and the radiation produced by the jet, as the combined effect of the wind and orbital motion deviates the jets from a straight trajectory. Several works study the dynamical influence of the stellar wind on the jets of HMMQs, and their expected radiative output, at the scales of the binary system (e.g., Romero & Orellana 2005; Khangulyan et al. 2008, 2018; Perucho & Bosch-Ramon 2008, 2012; Araudo et al. 2009; Owocki et al. 2009; Perucho et al. 2010; Yoon et al. 2016).

At larger scales, the effect of orbital motion becomes important and could make the jets follow a helical trajectory (see, e.g., Bosch-Ramon & Barkov 2016, for a semi-analytical study about this). Current observations allow for a detection of this kind of pattern in microquasars. The most famous case is perhaps SS433, in which the helical structure is likely caused by precession of the accretion disk (Begelman et al. 2006; Monceau-Baroux et al. 2014). Jet precession has also been observed in 1E 1740.7−2942 (Luque-Escamilla et al. 2015), even though it is a low-mass microquasar in which the stellar wind is not expected to have a strong dynamical influence. Cygnus X-3 is another system for which helix-like jets have been found (Mioduszewski et al. 2001; Miller-Jones et al. 2004), although the cause of their shape remains unclear. Finally, one may expect a strong wind-jet interaction in Cygnus X-1, given that it hosts a massive star close to the CO (e.g., Yoon et al. 2016; Bosch-Ramon & Barkov 2016). Nevertheless, observations have not shown evidence of the presence of helical jets in Cygnus X-1 so far (Stirling et al. 2001).

Article published by EDP Sciences

Since the orbital motion could leave a strong imprint on jet radiation in HMMQs, Molina & Bosch-Ramon (2018, hereafter MB18) computed the non-thermal radiative output of helical jets along the orbit using a phenomenological prescription for the jet kinematics. That work focused on a jet region rather far from the binary system, and the jet speed was taken well below the speed of light, due to a braking effect caused by instability growth and subsequent mixing of jet and wind material (Bosch-Ramon & Barkov 2016). However, closer to the launching site, within a few orbital separations from the jet base, the jet is thought to be relativistic (e.g., Fender et al. 2004). In that case, absorption processes and radiation cooling become more important, and Doppler boosting should be considered to compute the observable radiation.

The work presented here complements what was done in MB18 by studying in detail the wind-jet interaction on the scales of the binary system and its peripheral region. For that purpose, the jet trajectory is computed accounting for orbital motion and the momentum transferred by interaction with the stellar wind. The leptonic jet radiation is computed using a semi-analytical code, modeling the jets as one-dimensional emitters that radiate via the synchrotron and inverse Compton (IC) mechanisms. Absorption in radio and gamma rays is also accounted for.

The paper is organized as follows: in Sect. 2, we describe the physical system under study, as well as the the technical aspects of the dynamical and radiative models adopted. In Sect. 3, we present the main results of this work. Finally, a summary and a discussion of the results are given in Sect. 4.

2. Model description

2.1. System properties

The system studied in this work is a generic HMMQ, similar to Cygnus X-1, in which a CO is accreting matter from a massive companion star. The orbit is considered to be circular, with a period of $T = 4$ days and a separation of $a = 3 \times 10^{12}$ cm ≈ 0.2 AU. A jet and a counter-jet are ejected in opposite directions perpendicularly to the orbital plane, and progressively deviate from their initial direction by the combined effects of the stellar wind and orbital motion. The star is located at the origin of our coordinate system, which co-rotates with the CO counter-clockwise. For simplicity, we assumed that the star rotates synchronously with the coordinate system. The initial direction of the jets is taken as the z-axis. The x-axis is defined by the star-CO direction and the y-axis is perpendicular to it, in the direction of the orbital motion. The orbital phase of the CO is characterized by φ. The system is assumed to be at a distance of $d = 3$ kpc from an observer that sees the system with an inclination i with respect to the z-axis. Figure 1 illustrates this scenario.

The companion is a typical O-type star in the main sequence, with a temperature of $T_\star = 40\,000$ K and a luminosity of $L_\star = 10^{39}$ erg s^{-1} (Heap et al. 2006), which correspond to a radius of $R_\star \approx 7.4 \times 10^{11}$ cm. The stellar wind is assumed isotropic, with a velocity following the usual *β-law* form $v_\mathrm{w} = v_\infty (1 - R_\star/r)^{\hat\beta}$, where $v_\infty = 2 \times 10^8$ cm s^{-1} is the terminal wind speed, r is the distance to the star, and $\hat\beta = 0.8$ is typical for hot massive stars (e.g., Pauldrach et al. 1986). Although the $\hat\beta$-value is not tightly constrained, our results are almost insensitive to it within its usual range for O-type stars, $0.7 \lesssim \hat\beta \lesssim 1$ (Puls et al. 1996), and not very sensitive to values of $\hat\beta$ up to 3 found for some stars with different spectral types (Crowther et al. 2006). However, if a smaller a was considered, a variation of the $\hat\beta$-value would have a higher impact in our results given the proximity of the jets to the star. We also note that the adopted v_∞ is typical for O-type stars, but can be significantly lower for those with a later spectral type ($\sim$500 km s^{-1} for the B-supergiant in Vela X-1; Sander et al. 2018). The combination of a larger $\hat\beta$ and a smaller v_∞ for stars with a later spectral type would likely make their wind influence on the jets negligible. The mass-loss rate of the stellar wind is taken as $\dot M_\mathrm{w} = 10^{-6}\, M_\odot\,\mathrm{yr}^{-1}$, which is also a characteristic value for O-type stars (Lamers & Cassinelli 1999; Muijres et al. 2012).

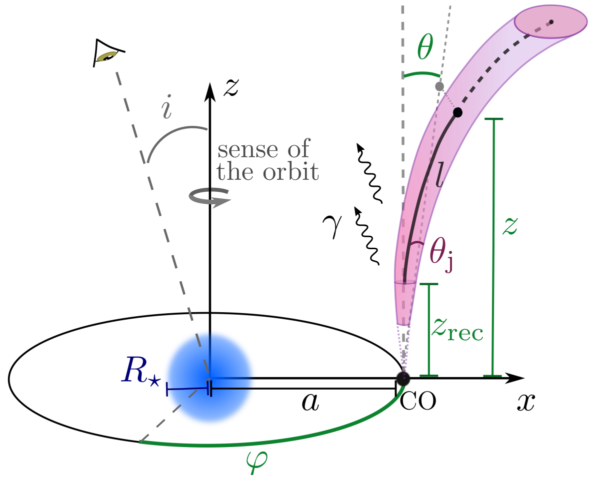

Fig. 1. Sketch of considered scenario (not to scale). We show a jet segment at a height z (black dot) and its projection in the xz-plane (grey dot). We also show the recollimation height z_rec, the length l along the jet, the jet half-opening angle θ_j, the jet bending angle with respect to the z-axis (θ), the inclination angle of the orbit i, the orbital separation a, the star radius $R_\star$, and the orbital phase φ (set to 0 and 0.5 for the inferior and superior conjunctions, respectively). The counter-jet (not shown) is symmetric to the jet with respect to the xy-plane.

As shown in Fig. 4 of Yoon et al. (2016), for a case similar to that studied here, the geometry of a jet shocked by the stellar wind departs from that of a conical jet. On the other hand, the shocked material surrounding the jet also takes part in the wind-jet momentum transfer, although this effect is difficult to capture without detailed simulations. Thus, for simplicity, we assume that the jets have a conical shape of half-opening angle $\theta_\mathrm{j} = 0.1$ rad, since they have been shown to be significantly collimated (e.g., Stirling et al. 2001). The jets are assumed to have a constant Lorentz factor γ_j from their launching to end points, the latter located at several a. Two values of γ_j are considered in order to assess the impact of this parameter in the results (e.g., due to different Doppler boosting).

Both jet and counter-jet have a kinetic power of $L_\mathrm{j} = 5 \times 10^{36}$ erg s^{-1}, a fraction η_NT of which is injected into non-thermal electrons accelerated with a rate $\dot E_\mathrm{acc} = \eta_\mathrm{acc} e c B$, where η_acc is the acceleration efficiency, and e the elementary charge. The fiducial values of η_NT and η_acc are both set to 0.1, but they are not well constrained beyond the fact that they both should be ≤ 1 (see Sect. 4). We focus here on electrons (and positrons) as hadronic radiation processes are far less efficient than leptonic ones under the conditions assumed in the emitting regions (e.g., Bosch-Ramon & Khangulyan 2009). We characterize the magnetic field at the jet base through a fraction η_B of the total jet energy density (see Sect. 2.3). Table 1 summarizes the different parameters that are used in this work.

Table 1. Jet, star, and system parameters that are used throughout this work.

Parameter		Value
Stellar temperature	$T_\star$	4×10^4 K
Stellar luminosity	$L_\star$	10^{39} erg s^{-1}
Mass-loss rate	$\dot{M}_\mathrm{w}$	$10^{-6}\,M_\odot$ yr^{-1}
Terminal wind speed	v_∞	2×10^8 cm s^{-1}
β-*law* exponent	$\hat{\beta}$	0.8
Jet luminosity	L_j	5×10^{36} erg s^{-1}
Non-thermal energy fraction	η_NT	0.1
Acceleration efficiency	η_acc	0.1
Jet half-opening angle	θ_j	0.1 rad
Orbital separation	a	3×10^{12} cm
Orbital period	T	4 days
Distance to the observer	d	3 kpc
Jet Lorentz factor	γ_j	1.2, 3
Magnetic pressure fraction	η_B	10^{-4}, 10^{-2}, 1
System inclination	i	0°, 30°, 60°

Notes. The last three are free parameters for which different values are explored.

2.2. Jet dynamics

The trajectory of the jet is computed starting from a height $z_0 = 2\times10^{10}$ cm, small enough so that wind effects are negligible. The counter-jet starts at $-z_0$. Initially the jets propagate in the $\hat{z}$ direction. However, the interaction with the stellar wind bends them away from the star in the $\hat{x}$ direction within the scales of the binary system. Additionally, at larger scales, the Coriolis force related to the orbital motion makes the jets bend in the $-\hat{y}$ direction, opposite to the sense of the orbit. We obtain the trajectory of the jets by dividing them into segments and computing iteratively how they are reoriented due to the momentum transfer by the stellar wind. In cylindrical coordinates, the first jet segment sets the following initial conditions for the position $\boldsymbol{r}$ and the momentum $\boldsymbol{P}$:

$$\begin{aligned}\boldsymbol{r}_1 &= (r,\phi,z) = (a,\varphi,z_0),\\ \boldsymbol{P}_1 &= (P_r,P_\phi,P_z) = (0,0,\dot{P}_\mathrm{j}\mathrm{d}t),\end{aligned} \tag{1}$$

where $\dot{P}_\mathrm{j} = L_\mathrm{j}\gamma_\mathrm{j}\beta_\mathrm{j}/c(\gamma_\mathrm{j}-1)$ is the total jet thrust, $\beta_\mathrm{j} = v_\mathrm{j}/c$ is the jet propagation velocity in units of the speed of light c, and $\mathrm{d}t$ is the segment advection time. In order to get the initial conditions for the counter-jet trajectory one just needs to change the sign of the z coordinate in both $\boldsymbol{r}_1$ and $\boldsymbol{P}_1$. The Coriolis plus wind forces acting on each segment are:

$$\begin{aligned}F_r &= S_\star\rho_\mathrm{w}v_\mathrm{w}\cos\theta,\\ F_\phi &= \rho_\mathrm{w}S_\phi\min\left(\frac{4\pi(r-a)}{T},\frac{2\pi r}{T}\right)^2,\\ F_z &= S_\star\rho_\mathrm{w}v_\mathrm{w}\sin\theta,\end{aligned} \tag{2}$$

where ρ_w is the wind density, θ is the angle between the r and z coordinates of the segment, and $S_\star$ and S_ϕ are the segment surfaces perpendicular to the $\boldsymbol{x}$ and $\boldsymbol{\phi}$ directions, respectively. As we work under the assumption of an isotropic, spherically symmetric wind, $\rho_\mathrm{w} = \dot{M}_\mathrm{w}/4\pi v_\mathrm{w}d_\star^2$, with $d_\star = \|\boldsymbol{r}\|$ being the distance to the star. Nevertheless, it is worth mentioning that some level of wind beaming towards the accretor is expected, especially for slow winds (Friend & Castor 1982; Gies & Bolton 1986; El Mellah et al. 2019a). This would increase the wind density in the orbital plane with respect to the isotropic case, while decreasing it off the plane, thus reducing the wind influence on the jets farther from the CO. Nonetheless, we neglect wind beaming since we work with a simplified prescription and a fast stellar wind is considered. The first term in the min function is the velocity corresponding to the Coriolis force at each segment position, while the second term is the wind velocity in the ϕ direction as seen from the jet, as the wind-jet relative ϕ-velocity cannot be larger than the wind tangential velocity in the non-inertial frame[1]. The forces in Eq. (2) are then used to compute the momentum of the subsequent segments as:

$$\boldsymbol{P}_{\mathrm{i}+1} = \boldsymbol{P}_\mathrm{i} + \boldsymbol{F}_\mathrm{i}\mathrm{d}t. \tag{3}$$

As we are taking here a constant propagation velocity v_j, the additional momentum that this prescription generates is assumed to go into heat of the shocked structure made of interacting jet and wind material. However, we do not consider the back reaction of the accumulated heat, nor instability growth and mixing, on the interacting flows. A more accurate and realistic account of the process would require carrying out costly 3-dimensional, relativistic hydrodynamical simulations. For simplicity, we use a phenomenological approach to compute the jet trajectory, acknowledging that as the jet segments get farther from the binary, our model becomes less realistic. Nevertheless, as the most relevant emitting regions are close to the binary system (see Sect. 3), we consider our approach a reasonable one at this stage. For illustrative purposes, Fig. 2 shows the path followed by the jet for $\gamma_\mathrm{j} = 1.2$ and 3.

2.3. Particle cooling

In this work, primed quantities refer to quantities in the fluid frame (FF), whereas unprimed quantities refer to the laboratory frame (LF). The jet emission is computed as in MB18, but accounting for relativistic effects and additional absorption mechanisms. The electron distribution and the synchrotron and IC luminosities are calculated first in the FF at each point along the jets. Then, the luminosities are computed as seen by the observer taking into account Doppler (de)boosting. Finally, these luminosities are corrected by different absorption processes.

The point where the non-thermal electrons are injected is located at a height z_rec ($-z_\mathrm{rec}$ for the counter-jet) for which a recollimation shock is formed due to the jet and wind momentum fluxes balancing each other in the y-axis direction (perpendicular to the jet propagation). This condition can be approximately expressed as follows (Bosch-Ramon & Barkov 2016):

$$\frac{\dot{P}_\mathrm{j}}{\pi z_\mathrm{rec}^2\gamma_\mathrm{j}^2} = \frac{\dot{P}_\mathrm{w}}{4\pi a^2}\left(\frac{a^2}{a^2+z_\mathrm{rec}^2}\right), \tag{4}$$

where $\dot{P}_\mathrm{w} = \dot{M}_\mathrm{w}v_\mathrm{w}$ is the wind thrust. For $\gamma_\mathrm{j} = 1.2$ we obtain $z_\mathrm{rec} = 1.4\times10^{12}\,\mathrm{cm}\approx0.47a$, whereas for $\gamma_\mathrm{j} = 3$, $z_\mathrm{rec} = 3.1\times10^{11}\,\mathrm{cm}\approx0.10a$. Some combinations of $\dot{P}_\mathrm{w}$, $\dot{P}_\mathrm{j}$ and γ_j yield non-physical (complex) values of z_rec in Eq. (4), which means that for those sets of parameters no recollimation shock is formed, as the momentum flux balance is never reached (see Yoon et al. 2016, for a non-relativistic simulation where this effect is studied).

Electrons are injected at $\vec{r_0}\approx(a,0,\pm z_\mathrm{rec})$, since the jet displacement in the x and y coordinates is small at $z = \pm z_\mathrm{rec}$

---

[1] We recall that we are assuming a star rotating synchronously with the CO, and thus the wind tangential velocity associated with the stellar rotation is zero.

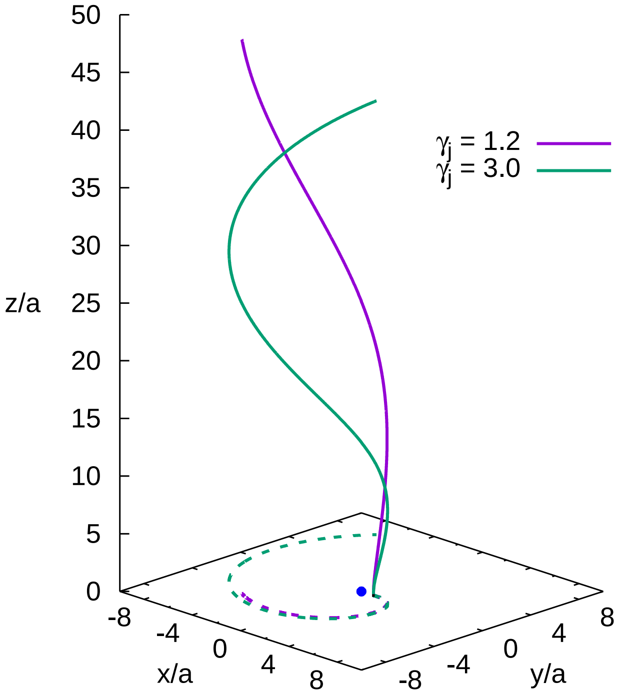

Fig. 2. Trajectory followed by the jet for $\gamma_j = 1.2$ (solid purple line) and 3 (solid green line). The projections in the orbital plane are also shown with dashed lines. The jet length is $50a$, and the counter-jet is symmetric to it with respect to the xy-plane (not shown). The blue circle at the origin of coordinates represents the star (to scale). The jets are plotted starting from the corresponding recollimation shocks.

($\lesssim 0.005a$ in the worst case). The particles are assumed to follow a power-law energy distribution with spectral index −2, typical for acceleration in strong shocks via the Fermi I mechanism (e.g Drury 1983), with a minimum energy of $E'_{\rm min} = 1$ MeV. An exponential cutoff is also assumed:

$$Q'(E') \propto E'^{-2} \exp\left(-\frac{E'}{E'_{\rm cutoff}}\right), \tag{5}$$

where E' is the electron energy in the FF. The normalization of $Q'(E')$ is obtained from the condition that the total power available for non-thermal electrons in the FF is $L'_{\rm NT} = \eta_{\rm NT} L_{\rm j}/\gamma_{\rm j}^2$. Electrons are convected from $\overrightarrow{r_0}$ along the jet path while they cool down via adiabatic, synchrotron and IC processes. For simplicity, we neglect particle acceleration beyond $\overrightarrow{r_0}$, even though weak shocks and turbulence may (re)accelerate particles further downstream in the jets. Analytical expressions are used for the energy losses in the FF (see Longair 1981; Khangulyan et al. 2014 for synchrotron and IC losses, respectively). The characteristic timescale for adiabatic cooling is $t'_{\rm ad} = E'/\dot{E}'_{\rm ad} = 3R_{\rm j}/2\theta_{\rm j} v_{\rm j} \gamma_{\rm j}$, where $R_{\rm j}(l) \propto l$ is the jet radius.

The magnetic pressure at the accelerator (located at $\overrightarrow{r_0}$) is characterized in the FF as a fraction η_B of the total jet energy density:

$$\frac{B_0'^2}{8\pi} = \eta_B \frac{L_{\rm j}}{\pi \gamma_{\rm j}^2 r_{\rm j,0}^2 v_{\rm j}}, \tag{6}$$

where $B'_0 = B_0/\gamma_{\rm j}$ and $r_{\rm j,0} = R_{\rm j}(z_{\rm rec})$ are the magnetic field and the jet radius at $\overrightarrow{r_0}$, respectively. For the same B'_0, this fraction relates to the ratio of magnetic pressure to stellar photon energy density in the LF as $\eta_B^\star = 4(r_0/r_{\rm j,0})^2 (L_{\rm j}/L_\star)\beta_{\rm j}^{-1}\eta_B$, which is useful to compare the expected radiation outputs of synchrotron and IC processes. This yields $\eta_B^\star \approx 19\eta_B$ for $\gamma_{\rm j} = 1.2$, and $\eta_B^\star \approx 200\eta_B$ for $\gamma_{\rm j} = 3$. The jet magnetic field is assumed perpendicular to the flow in the FF, since at the scales considered in this work, far from the jet launching point, a dominant toroidal component for the magnetic field is expected (e.g., Pudritz et al. 2012). Given the adopted assumptions plus frozen in conditions, the magnetic field at each jet point can be computed as:

$$B'(l) = B'_0 \frac{r_{\rm j,0}}{R_{\rm j}(l)}\cdot \tag{7}$$

The cutoff energy $E'_{\rm cutoff}$ is the maximum energy that the electrons can achieve in the accelerator region in the FF, and it is obtained as follows:

1. We compare the acceleration timescale $t'_{\rm acc} = E'/\dot{E}'_{\rm acc} = E'/\eta_{\rm acc} e c B'_0$ with the cooling timescale $t'_{\rm loss} = E'/\dot{E}'$, where $\dot{E}'$ is the cooling rate accounting for adiabatic, synchrotron and IC losses. In this work we set $\eta_{\rm acc} = 0.1$ as a representative case with efficient particle acceleration. The energy $E'^{\rm acc}_{\rm max}$ at which the two timescales are equal is the maximum energy that electrons can attain before the energy losses overcome the energy gain by acceleration.
2. We compare $t'_{\rm acc}$ with the diffusion timescale $t'_{\rm diff} = r_{\rm j,0}^2/2D$, where $D = E'c/3eB'_0$ is the diffusion coefficient in the Bohm regime. If diffusion is a dominant process, particles cannot reach $E'^{\rm acc}_{\rm max}$ before escaping the accelerating region. We can estimate the maximum energy attainable by the electrons before they diffuse away from the accelerator, $E'^{\rm diff}_{\rm max}$, by equating $t'_{\rm acc} = t'_{\rm diff}$.
3. We obtain the cutoff energy as $E'_{\rm cutoff} = \min(E'^{\rm acc}_{\rm max}, E'^{\rm diff}_{\rm max})$. For the different sets of parameters considered in this work we always obtain a $E'_{\rm cutoff}$ of a few TeV.

In order to compute the electron energy distribution $N'(E', l)$ along the jet, the latter is divided into 1500 segments with size $dl = 10^{11}$ cm, extending to a total length of $l_{\rm j} = 1.5 \times 10^{14}$ cm $= 50a$. Once the injection function $Q'(E')$ is determined, the electron energy distribution $N'(E', l)$ is computed for each segment l in an iterative way as done in MB18, but considering that all quantities must be expressed in the FF. This defines a structured, linear relativistic emitter along the trajectory shown in Fig. 2.

2.4. Radiation

We focus our study in the computation of synchrotron and IC radiation of leptons along the jets. Hadronic processes are likely much less efficient at the scales considered in this work, given the conditions of the emitting regions. Relativistic bremsstrahlung is also expected to be unimportant in comparison to the synchrotron and IC mechanisms (Bosch-Ramon & Khangulyan 2009).

At each segment of the jet, the spectral energy distribution (SED) of the emitted synchrotron radiation for an isotropic population of electrons in the FF is given by (Pacholczyk 1970):

$$\varepsilon' L'^{\rm syn}_{\varepsilon'}(l) = \varepsilon' \frac{\sqrt{2} e B'(l)}{m_{\rm e} c^2 h} \int_{E_{\rm min}}^{\infty} F(x') N'(E', l)\, dE', \tag{8}$$

where ε' is the photon energy, $m_{\rm e}$ is the electron mass, h is the Planck constant, $x' = \varepsilon'/\varepsilon'_{\rm c}$, and $\varepsilon'_{\rm c} = \sqrt{3} e h B' E'^2/(2\sqrt{2}\pi m_{\rm e}^3 c^5)$ is the critical photon energy assuming an isotropic distribution of the pitch angle θ'_B between the electron velocity and the magnetic field, such that $B' \sin\theta'_B \approx \sqrt{\langle B'^2 \rangle} = B' \sqrt{2/3}$. The function $F(x')$ can be approximated by $F(x') \approx 1.85\ x'^{-1/3} e^{x'}$ for $x' \in [0.1, 10]$ (Aharonian 2004).

For the calculation of the IC emission we only consider the up-scattering of stellar photons; other radiation fields (such as the one from the accretion disk) are negligible in comparison to the stellar one on the relevant scales. Synchrotron self-Compton also turns out to be negligible. We use the prescription developed by Khangulyan et al. (2014) to compute the interaction rate of an electron with a monodirectional field of target photons with a black body distribution, $\mathrm{d}^2N'/\mathrm{d}\varepsilon'\mathrm{d}t'$. For simplicity, we do not consider possible deviations from a black-body spectrum owing to absorption of stellar photons by wind material, since this is not expected to have a significant effect on the IC emission (see Reitberger et al. 2014, for an illustrative comparison between a black-body and a monochromatic stellar spectrum in colliding-wind binaries). Assuming an isotropic distribution of electrons in the FF, the IC SED at each jet segment is computed as:

$$\varepsilon' L'^{\mathrm{IC}}_{\varepsilon'}(l) = \varepsilon'^2 \int_0^\infty \frac{\mathrm{d}^2 N'}{\mathrm{d}\varepsilon'\,\mathrm{d}t'} N'(E', l)\,\mathrm{d}E'. \tag{9}$$

Once the luminosities are obtained in the FF, we transform them into what would be seen by the observer. For a stationary jet such as the one considered in this work, we have $\varepsilon L_\varepsilon = \varepsilon' L'_\varepsilon \delta^3_{\mathrm{obs}}/\gamma_{\mathrm{j}}$ (Sikora et al. 1997), where $\delta_{\mathrm{obs}} = [\gamma_{\mathrm{j}}(1 - \beta_{\mathrm{j}} \cos\theta_{\mathrm{obs}})]^{-1}$ is the Doppler factor between the emitter and the observer, the velocity of the former and the latter making an angle θ_{obs} in the LF (e.g., Dermer & Schlickeiser 2002). This transformation is done individually for each jet segment, as θ_{obs}, and thus δ_{obs}, varies from one to another. Photon energies as seen by the observer are $\varepsilon = \delta_{\mathrm{obs}}\varepsilon'$.

2.5. Absorption mechanisms

Two main photon absorption processes are considered in this work: electron-positron pair creation from gamma rays interacting with stellar photons ($\gamma\gamma-$absorption, GGA), and the absorption of low-energy photons by the free ions present in the wind (free-free absorption, FFA). Synchrotron self-absorption is also computed and found to be negligible in comparison to FFA in this scenario, regardless of the adopted parameters. The absorption coefficients are calculated directly in the LF, as the emitted luminosities are previously transformed to what would be seen by the observer (see Sect. 2.4).

The optical depth for GGA is computed as follows:

$$\tau_{\gamma\gamma}(\varepsilon) = \int_0^d \mathrm{d}s\ [1 - \cos\theta_{\gamma\gamma}(s)] \int_{\varepsilon_0^{\min}(\theta_{\gamma\gamma})}^{\infty} \mathrm{d}\varepsilon_0\ n(\varepsilon_0)\sigma_{\gamma\gamma}(\varepsilon, \varepsilon_0, s), \tag{10}$$

where s parametrizes the gamma-ray photon trajectory along the line-of-sight, d is the distance to the observer, $\theta_{\gamma\gamma}$ is the angle between the momentum of this photon and the stellar photons, ε_0 is the energy of the latter, which follows a black body distribution $n(\varepsilon_0)$, and $\sigma_{\gamma\gamma}$ is the cross-section for GGA, obtained from Eq. (1) of Gould & Schréder (1967). The lower integral limit $\varepsilon_0^{\min} = 2m_{\mathrm{e}}^2c^4/\varepsilon(1 - \cos\theta_{\gamma\gamma})$ is the energy threshold for the creation of an electron-positron pair.

Regarding the FFA process, its absorption coefficient is given by (e.g., Rybicki & Lightman 1986):

$$\alpha_{\mathrm{ff}} = \frac{4e^6}{3m_{\mathrm{e}}hc}\sqrt{\frac{2\pi}{3k_{\mathrm{B}}m_{\mathrm{e}}}} Z^2 n_{\mathrm{e}} n_{\mathrm{i}} T^{-1/2} \nu^{-3}\left(1 - \mathrm{e}^{-h\nu/k_{\mathrm{B}}T}\right) g_{\mathrm{ff}}, \tag{11}$$

with $n_{\mathrm{i,e}}$ being the number density of ions/electrons in the wind, T its temperature, Z the mean atomic number (taken as 1), ν the photon frequency, and g_{ff} the average Gaunt factor, which can be estimated as $g_{\mathrm{ff}} \approx 9.77[1 + 0.056\ln(T^{3/2}/Z\nu)]$ (Leitherer & Robert 1991).

FFA is strongly dependent on the wind density (as $\propto n_{\mathrm{w}}^2$), and consequently would also be significantly affected by the presence of wind beaming (see Sect. 2.2). Also, for $h\nu \ll k_{\mathrm{B}}T$ the absorption is $\propto \nu^{-2}$, so its effect is much larger for low radio frequencies. The FFA optical depth can be calculated as

$$\tau_{\mathrm{ff}}(\nu) = \int_0^d \alpha_{\mathrm{ff}}(\nu, r)\,\mathrm{d}s, \tag{12}$$

where r is the distance to the star. Given that the stellar wind has a density $n_{\mathrm{w}} \propto r^{-2}$ and that we are modeling a compact system in which the jet inner regions are close to the star, strong absorption is expected in radio.

In addition to the three aforementioned absorption processes, occultation of some parts of the jets by the star is also taken into account (e.g., Khangulyan et al. 2018). Although unimportant for most system configurations, stellar occultation can have a moderate impact on the radiation output for high system inclinations ($i \gtrsim 60°$) when the CO is behind the star (see Sect. 3.3).

3. Results

We explore different values for three free parameters of our model: γ_{j}, η_B, and i (see Table 1). Moreover, we also study the orbital variability of the results by varying φ between 0 and 1 (see Fig. 1). The energy losses and the particle energy distribution are only affected by γ_{j} and η_B, whereas the radiative outputs also depend on i and φ. The observer is assumed to be always in a position such that the CO is closest to the observer for $\varphi = 0$ (inferior conjunction), and farthest from the observer for $\varphi = 0.5$ (superior conjunction). As we are considering a circular orbit, by studying a whole period we cover all the possible system configurations.

3.1. Particle distribution

In Fig. 3, we show the electron energy distribution of each jet segment for $\gamma_{\mathrm{j}} = 1.2$ and $\eta_B = 10^{-2}$ and 1 (which yield $B'_0 = 28.2$ G and 282 G, respectively), as well as the total electron energy distribution up to three different lengths along the jet. The relevant timescales for the first jet segment, where relativistic electrons are injected, are shown in Fig. 4 for $\gamma_{\mathrm{j}} = 1.2$ and $\eta_B = 10^{-2}$. Both the electron distribution and the timescales associated to it are the same for the jet and the counter-jet. For $\eta_B = 1$, synchrotron is the dominant cooling mechanism for electrons with $E' \gtrsim 50$ MeV, and those with $E' \gtrsim 1$ GeV cool down already within the first segment. At lower electron energies the cooling is dominated by the adiabatic expansion of the jet, which allows most of the particles below ~50 MeV to reach distances outside the binary system. For $\eta_B = 10^{-2}$, the synchrotron dominance only happens above ~30 GeV, and there is also a significant contribution of IC losses for 1 GeV $\lesssim E' \lesssim$ 70 GeV, as seen in Fig. 4. However, this contribution is only relevant for the inner $l \sim 10^{13}$ cm of the jet, where the stellar radiation field is strong; farther away adiabatic losses also dominate in this energy range.

3.2. Spectral energy distribution

The SEDs in this section are computed using $\varphi = 0.25$ as a representative situation. Figure 5 shows the combined SED (as

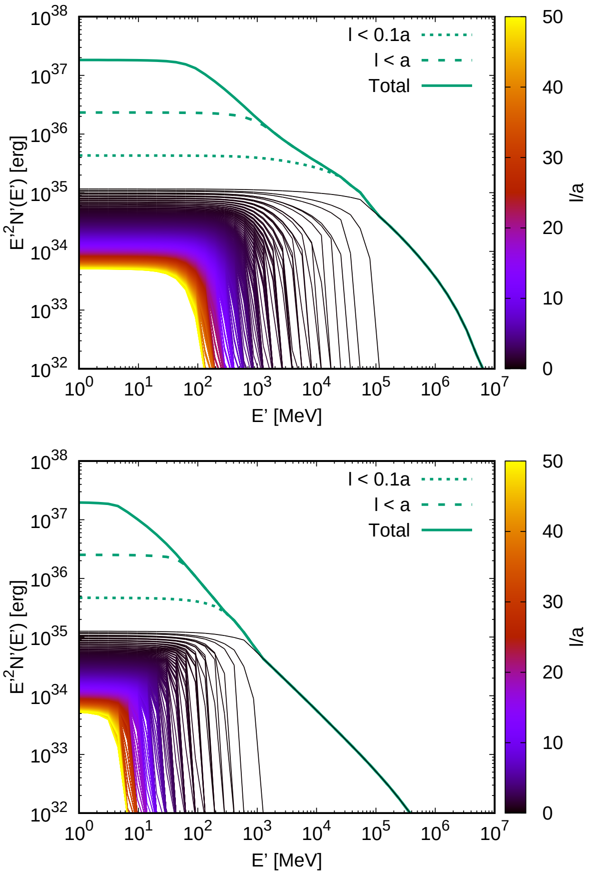

Fig. 3. Energy distribution of the electrons along the jet up to $0.1a$ (dotted line), a (dashed line), and the whole jet (solid line), for $\gamma_j = 1.2$, $\eta_B = 10^{-2}$ (*top panel*), and $\eta_B = 1$ (*bottom panel*). The contribution of the individual jet segments is color-coded, with the color scale representing the position of each segment along the jet. Segments have a constant length of $dl = 10^{11}$ cm ≈ 0.03a.

seen by the observer) of the jet and the counter-jet for $\gamma_j = 1.2$, $i = 30°$, and $\eta_B = 10^{-2}$ and 1. The contribution of the regions of the jets further from to the CO is also depicted. The bump at low energies of the synchrotron SED for $\eta_B = 1$ is a numerical artifact without physical meaning caused by how the first jet segment is treated when computing the particle distribution for intense energy losses (see MB18, a bump is also hinted in the electron energy distribution in Fig. 3). The η_B-value has a strong influence on the synchrotron and IC luminosities, as expected from its relation to $\eta_B^\star$. The SED is totally dominated by the emission at the binary system scales, except for the low-energy end of the synchrotron component, in which the radiation output comes mainly from the more external regions given the high level of FFA close to the star. This same absorption process is the responsible for the lack of radio emission in the spectrum. GGA is significant even for small system inclinations, despite a low i not favouring this absorption process.

The separate jet and counter-jet SEDs are presented in Fig. 6 for $i = 0°$, $30°$ and $60°$, $\eta_B = 10^{-2}$, and $\gamma_j = 1.2$ and 3. The jet is responsible for most of the emission even for a high inclination, which reduces the effect of Doppler boosting. Figure 7 shows the evolution along the jet of the Doppler boosting factor, $\delta_{\rm obs}^3/\gamma_j$, for $\gamma_j = 1.2$ and 3, and $i = 0°$, $30°$ and $60°$. Results are only shown

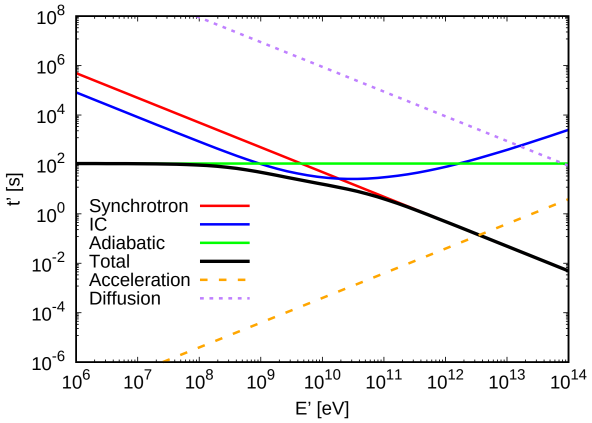

Fig. 4. Characteristic timescales for the first jet segment for $\gamma_j = 1.2$ and $\eta_B = 10^{-2}$. Cooling (solid lines), acceleration (dashed line), and diffusion (dotted line) processes are shown.

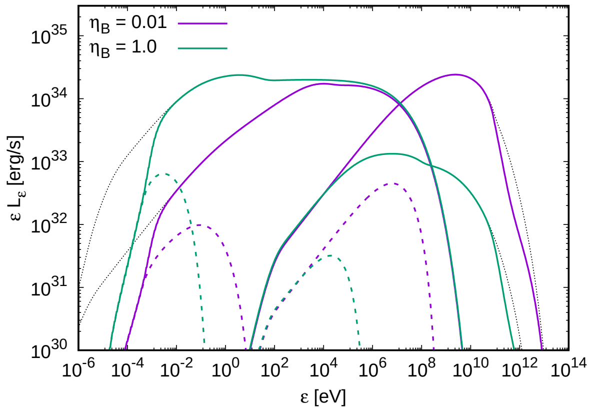

Fig. 5. Total (jet + counter-jet) synchrotron and IC SEDs for $\gamma_j = 1.2$, $i = 30°$, $\varphi = 0.25$, and $\eta_B = 10^{-2}$ (purple lines) and 1 (green lines). Dashed lines show the contribution of the jets beyond a length a, and black dotted lines represent the unabsorbed emission.

up to $l = 10a$, as the contribution of the jets to the SED beyond this length is negligible. For $\gamma_j = 1.2$, $\delta_{\rm obs}^3/\gamma_j$ remains almost constant because $\theta_{\rm obs}$ does so, given the small jet deviation with respect to a straight trajectory at the scales shown in the plot (see Fig. 2). For this γ_j−value, the emission is boosted with respect to the FF as long as $i \lesssim 60°$. For $\gamma_j = 3$ the variation of the Doppler boosting factor along the jet becomes more important due to its helical shape, and the emission is already deboosted for $i \gtrsim 30°$. We note that a higher γ_j implies more boosting only when $i \sim 0$. This can further be seen in Fig. 6, where only for the case of $i = 0$ the SED for $\gamma_j = 3$ becomes comparable to that for $\gamma_j = 1.2$.

The intrinsic jet emission is also highly influenced by the value of γ_j as the latter affects the magnetic and photon fields in the FF. In terms of particle cooling, the relative importance of each process varies with γ_j. Synchrotron losses become less efficient for increasing Lorentz factor, as $t'_{\rm syn} \propto B'^{-2} \propto \gamma_j^2$, whereas adiabatic losses become more dominant, as $t'_{\rm ad} \propto \gamma_j^{-1}$. The dependence of IC cooling with γ_j is more complex (see Khangulyan et al. 2014), but for the cases considered in this work the variation of $t'_{\rm IC}$ is small compared to that of $t'_{\rm syn}$ and

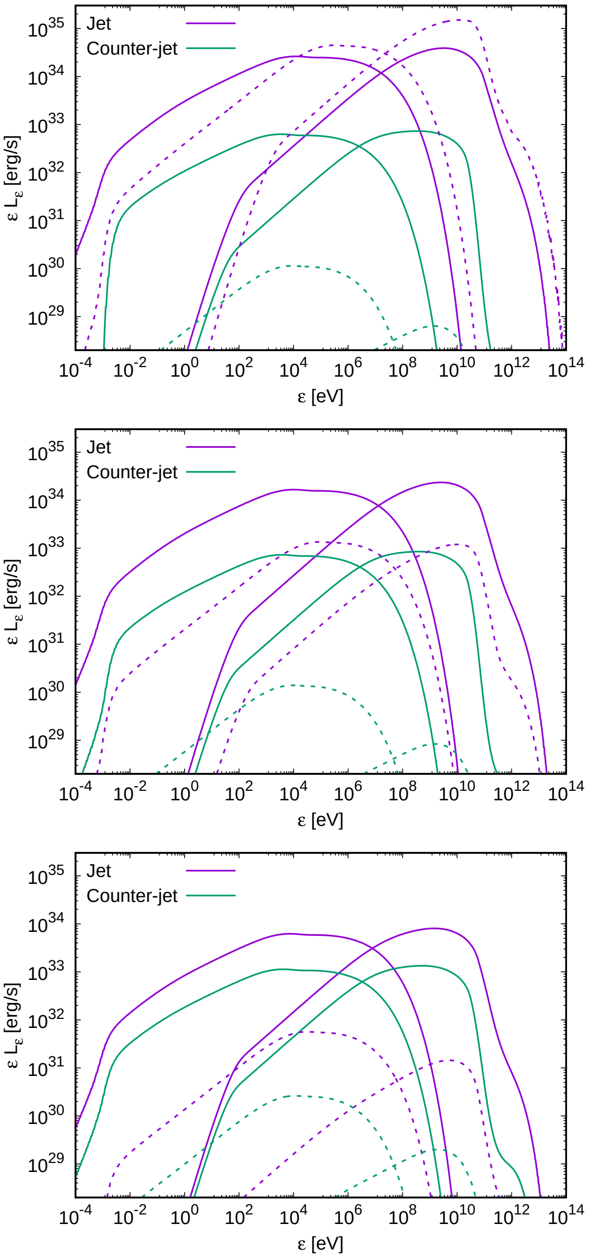

Fig. 6. SEDs of the jet (purple lines) and the counter-jet (green lines) for $\eta_B = 10^{-2}$, $\varphi = 0.25$, $i = 0$ (*top*) 30° (*middle*) and 60° (*bottom*), and $\gamma_{\rm j} = 1.2$ (solid lines) and 3 (dashed lines).

$t'_{\rm ad}$. In general, the combination of the effects of $\gamma_{\rm j}$ on the intrinsic and observed radiative outputs results in a decrease of the detected emission when $\gamma_{\rm j}$ increases, except for small enough values of i.

3.3. Orbital variability

Figures 8 and 9 show the total SEDs for $\eta_B = 10^{-2}$, $i = 30°$ and 60°, and different values of $\varphi \in [0, 0.5]$, $\gamma_{\rm j} = 1.2$ and 3, respectively. Emission is almost symmetric for the remaining orbit, that is $\varphi \in (0.5, 1)$, despite the helical trajectory of the jets. The difference, thus, being only of a few percent, is not shown in the plot. Synchrotron emission at $\varepsilon \gtrsim 10^{-2}$ eV remains almost constant over the whole orbit, with slight variations corresponding to small changes in the $\delta_{\rm obs}$ in the inner jet regions. At lower energies, especially for $i = 60°$, the difference becomes a bit more noticeable due to FFA becoming stronger as the CO approaches the superior conjunction ($\varphi = 0.5$). Both IC emission and GGA are strongly affected by the orbital phase and steadily increase as φ goes from 0 to 0.5. This makes the IC radiation output at most photon energies increase towards the superior conjunction, with the exception of the highest gamma-ray energies ($\varepsilon \gtrsim 100$ GeV), for which the emission of the phases closer to the inferior conjunction is larger due to less efficient GGA. This effect is more pronounced for high inclinations, as the strength of GGA increases with i close to the superior conjunction.

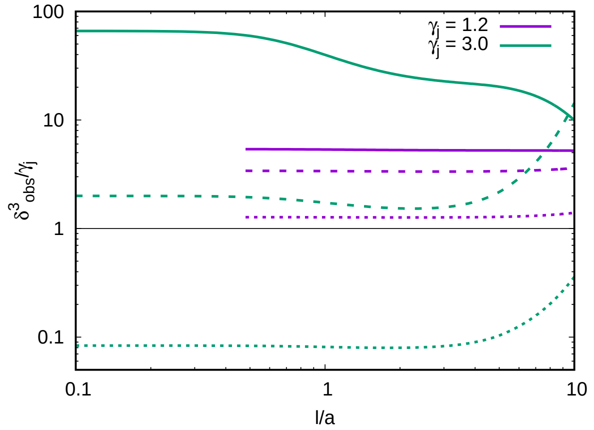

Fig. 7. Doppler boosting factor as a function of jet position for $\varphi = 0.25$, $\gamma_{\rm j} = 1.2$ and 3, and $i = 0$ (solid lines), $i = 30°$ (dashed lines), and $i = 60°$ (dotted lines). The black solid line at $\delta^3_{\rm obs}/\gamma_{\rm j} = 1$ sets the border between boosting (>1) and deboosting (<1). Only the values up to $l = 10a$ are shown.

Figures 10 and 11 show the light curves at different energy bands for $\gamma_{\rm j} = 1.2$ and 3, respectively. Two inclinations, $i = 30°$ and 60°, are studied for $\eta_B = 10^{-2}$. Light curves for straight (unbent) jets moving perpendicular to the orbital plane are also shown for comparison, although we note that this is not a realistic case given the adopted wind and jet parameters. The bumps seen at $\varphi = 0.5$ and $\varepsilon \leq 10$ GeV are caused by photon occultation by the star. Orbital modulation for $\varepsilon \geq 100$ MeV becomes more important the higher the system inclination is. As an example, in the case of $\gamma_{\rm j} = 3$ (Fig. 11) and 10 GeV $\leq \varepsilon \leq$ 100 GeV, for $i = 30°$ the flux changes only by a factor of ~3 along the orbit, whereas for $i = 60°$ it changes by a factor of ~20. This effect is not observed for $\varepsilon < 100$ MeV, as the weakly φ-dependent synchrotron emission dominates at these energies.

The fluxes for bent and straight jets are similar between them, with differences of at most ~15% for $\eta_B = 10^{-2}$. The situation is the same when one considers the orbit-averaged values. This is explained by the strong concentration of the emission at the jet inner regions ($\lesssim a$; see Fig. 5), where the difference in the shape of straight and helical jets is small. For $\gamma_{\rm j} = 1.2$, this difference remains small even for $l \gg a$. If one considers a lower magnetic field, however, the situation changes. Figure 12 shows the light curves for $\gamma_{\rm j} = 3$ and $\eta_B = 10^{-4}$ ($B'_0 = 4.04$ G). As the energy losses close to the CO are less intense, IC emission is more significant for $l > a$ and the light curves have distinct features due to the helical jet trajectory. On the one hand, the

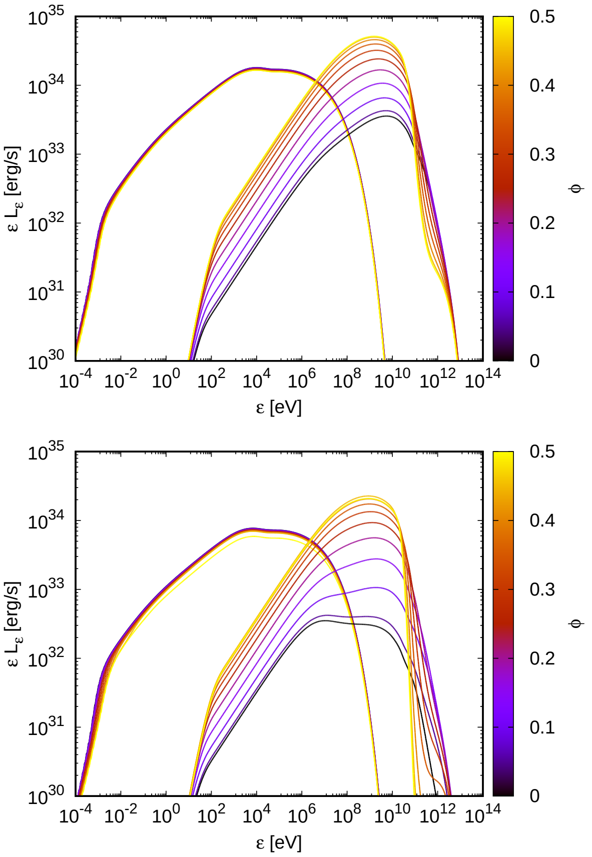

Fig. 8. Total synchrotron and IC SEDs for $\gamma_{\rm j} = 1.2$, $\eta_B = 10^{-2}$, $i = 30°$ (*top*) and 60° (*bottom*), and different orbital phases between 0 and 0.5. SEDs for $0.5 < \varphi < 1$ are not represented because they almost overlap with those shown.

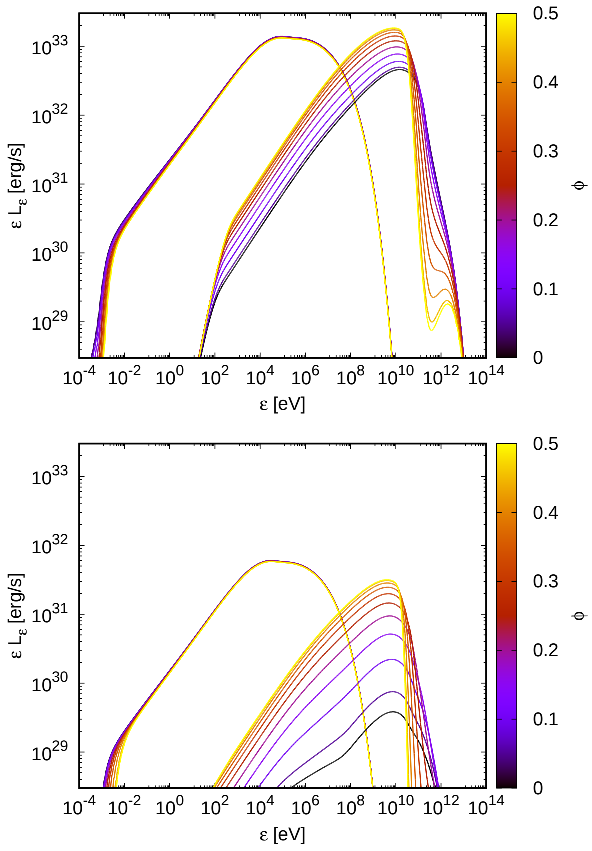

Fig. 9. Same as in Fig. 8, but for $\gamma_{\rm j} = 3.0$. Note the change in the y-axis scale.

difference in the fluxes with respect to straight jets is higher, up to ~40% for $\varepsilon > 10$ GeV. On the other hand, asymmetries in the light curves with respect to $\varphi = 0.5$ arise for $i = 60°$.

4. Summary and discussion

We have extended the study performed in MB18 to the inner regions of HMMQ jets in order to assess the role of the wind-jet interaction at the binary system scales. On those scales, the jet is likely to be more relativistic than further away from the binary (i.e., MB18, the scales studied in). We have shown that the stellar wind plus orbital motion can have a significant effect on the jet radiative output. As a result of this wind-jet interaction, the jets get a helical shape that affects angle-dependent processes such as IC scattering, GGA, and relativistic Doppler boosting. Most of the jet emission is produced at distances below a few orbital separations. If one compares the present results to those of MB18, one finds that the predicted fluxes are similar, although $L_{\rm NT}$ is here an order of magnitude higher, meaning more efficient acceleration is assumed in the strong, asymmetric jet recollimation shock than in the shock at larger scales considered in MB18. The radio emission is severely absorbed in the stellar wind via FFA. This prevents us to use this emission to trace the helical jet structure, as it was done in MB18. Additionally, the small scales considered in this work would require a very high (μ-arcsecond) angular resolution to address such a study. The high proximity to the star also makes IC emission and GGA more susceptible to change along the orbit, which results in a much stronger orbital modulation than in MB18, especially for high-energy gamma rays with $\varepsilon \gtrsim 100$ MeV. Evidence of such a modulation has been found for Cygnus X-3 (Zdziarski et al. 2018), and hints of such an effect have also been observed in Cygnus X-1 (Zanin et al. 2016; Zdziarski et al. 2017).

Including the helical shape of the jets has a moderate impact on the predicted light curves with respect to the straight jet case, introducing a variation not higher than ~40%, with this value depending on the strength of the magnetic field. At the energies at which GGA plays an important role ($\varepsilon \gtrsim 10$ GeV), the emission from helical jets is consistently more absorbed close to the superior conjunction due to the additional distance that the gamma-rays have to travel embedded in the stellar photon field. Nonetheless, this feature must be taken with caution, as a similar effect could be seen for straight jets with acceleration at $z < z_{\rm rec}$, not associated with the recollimation shock. Moreover, helical jets may have stronger energy dissipation, and thereby particle acceleration, than straight jets at $z > z_{\rm rec}$ (not considered here), which could counterbalance also this effect. For small magnetic fields, the asymmetry in the light curves of jets with a helical shape could hint at the presence of this kind of jet structure in HMMQs. This asymmetries were also obtained by Dubus et al. (2010) when studying the effect of jet precession in the gamma-ray light curve of Cygnus X-3.

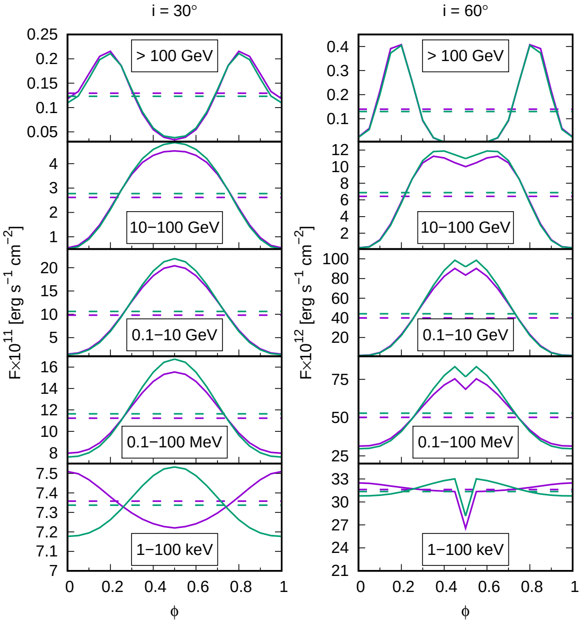

Fig. 10. Integrated light curves for $\gamma_j = 1.2$, $\eta_B = 10^{-2}$, $i = 30°$ and 60°, and different photon energy ranges. Purple lines represent the values for bent jets such as those in Fig. 2, whereas green lines represent the results for straight jets. Dashed lines show the orbit-averaged flux values. Note the change in the flux normalization for each i.

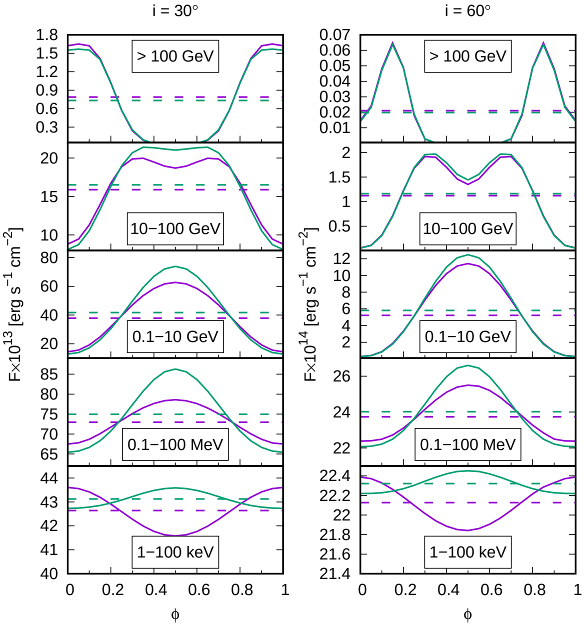

Fig. 11. Same as in Fig. 10, but for $\gamma_j = 3$.

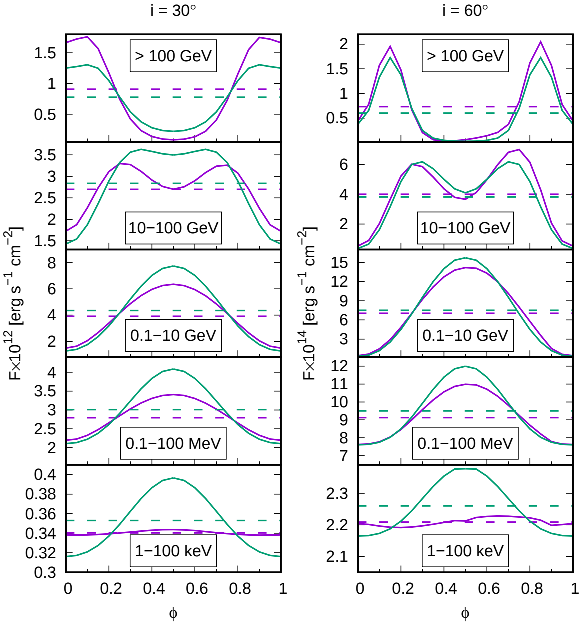

Fig. 12. Same as in Fig. 10, but for $\gamma_j = 3$ and $\eta_B = 10^{-4}$.

The parameters $\eta_{\rm NT}$ and $\eta_{\rm acc}$ used in our model are very difficult to constrain both observationally and from first principles, and thus we have only taken representative values for them. In the case of $\eta_{\rm NT}$, the values of the luminosities and fluxes are easily scalable as $\propto\eta_{\rm NT}$. The value of $\eta_{\rm acc}$ affects the maximum energy that the electrons can attain, and consequently the peak position of the synchrotron and IC components in the SED. A significantly lower value of $\eta_{\rm acc}$ would not allow synchrotron (IC) photons to reach X-rays (gamma rays above 100 GeV), whereas the GeV emission would remain relatively unaffected. As noted, it is also possible that electrons are accelerated in a continuous region extending beyond $\vec{r_0}$. This would modify the particle distribution in such a way that relativistic electrons could propagate further downstream along the jet without cooling down within the first jet segment. As synchrotron losses would not be so dominant further from the CO, this would result in an increase in the emitted gamma-ray luminosity and a decrease in the X-ray luminosity. In addition, the maximum electron and emitted photon energies could be somewhat higher if not limited by synchrotron cooling but by the accelerator size (e.g., Khangulyan et al. 2008). In the present work, for simplicity, we neglect electron acceleration beyond $z_{\rm rec}$, but this possibility should be considered in future studies.

Another free parameter in our model is related to the magnetic field strength, η_B. As shown in Fig. 5, this parameter has a strong impact on the produced fluxes at all photon energies, and it also affects the degree of concentration of the emission close to the CO: the higher η_B is, the more concentrated the emission is. The position of the synchrotron high-energy cutoff is rather insensitive to η_B, whereas it strongly affects the (unabsorbed) IC high-energy cutoff. Therefore, for a higher η_B (stronger B) the synchrotron and IC cutoffs get closer. It is worth noting as well that, for a matter dominated jet, it is not expected that η_B approaches 1. However, depending on the location of $z_{\rm rec}$ (and thus on the value of γ_j), even values of η_B well below one could still mean rather high values for $\eta_B^\star$, yielding an IC flux comparable or even higher than the synchrotron one. As an example, a magnetic fraction $\eta_B = 10^{-2}$ implies $\eta_B^\star \approx 2$ for $\gamma_j = 3$, and $\eta_B^\star \approx 0.19$ for $\gamma_j = 1.2$. This also means that, regardless of the value of η_B, the strong impact of $z_{\rm rec}$ on the value of $\eta_B^\star$, shows that the synchrotron and the IC predictions are rather sensitive to the parameters determining the wind-jet interaction, which are not well constrained (e.g., Yoon et al. 2016; Bosch-Ramon & Barkov 2016).

The wind-jet interaction makes our results valid only for distances up to a few a. The development of instabilities and significant mixing of the jet and wind material are expected to happen already on the binary system scales (Perucho et al. 2010). The former could have an important effect on the jet trajectory at larger scales, while the latter would imply a reduction of γ_j the more the wind material is mixed with the jets. The assumption of a constant θ_j-value is also a simplification, as it is likely that the aperture of the jets is modified by the action of the stellar wind (Bosch-Ramon & Barkov 2016). Despite all this, these effects should not have a significant impact on our results as in our model the radiation output tends to be concentrated on a region at $z \lesssim a$ (except for $z_\mathrm{rec} \sim a$). In any case, proper 3D relativistic simulations of HMMQ jets on large scales would be needed for a more accurate study of the wind-jet interaction.

Both jet instability growth and wind-jet mixing are expected to become more important for clumpy winds (Perucho & Bosch-Ramon 2012), which are usual in massive stars (Owocki & Cohen 2006; Moffat 2008). Non-homogeneous winds may also change the accretion rate of material onto the CO by a few 10% within timescales of several minutes, with a time-averaged value similar to that of an isotropic wind (El Mellah et al. 2018). This would consequently modify the jet power, introducing also a time variability in L_j. Moreover, a clumpy wind would also affect the intensity of FFA, given the latter's dependence on the wind density. Considering a simple microclumping model, typical clumping factors ≤100 (e.g., Mokiem et al. 2007; de Koter et al. 2008) would increase the free-free opacity by a factor of $f \lesssim 10$ (Muijres et al. 2011), and the wind would remain opaque up to frequencies $f^{1/2} \lesssim 3$ times larger than for a homogeneous wind (see Eq. (11)). Therefore, the qualitative results presented in this work regarding the absorption at radio frequencies are independent of the detailed considerations on wind clumping.

Finally, we emphasize that detailed information (e.g., well-sampled light curves) in different energy bands is required in order to significantly constrain the parameter space of the system physical properties. This is the only possible way to disentangle the degeneracy arising from multiple parameter combinations that yield similar results for quantities such as the average flux at a specific energy band. Such studies could be addressed in a future with current and in development observatories, such as *NuSTAR* (hard X-rays), e-ASTROGAM (MeV gamma-rays), *Fermi* (high-energy gamma rays), and CTA (very high-energy gamma rays). Devoted observing time with these instruments would help to improve our knowledge on the interplay between the stellar wind and the jets in HMMQs, and the associated non-thermal processes.

Acknowledgements. We want to thank the referee, Ileyk El Mellah, for his extensive and constructive comments that helped to improve this work. EM and VB acknowledge support by the Spanish Ministerio de Economía y Competitividad (MINECO/FEDER, UE) under grant AYA2016-76012-C3-1-P, with partial support by the European Regional Development Fund (ERDF/FEDER) and MDM-2014-0369 of ICCUB (Unidad de Excelencia "María de Maeztu"). EM acknowledges support from MINECO through grant BES-2016-076342. SdP acknowledges support from CONICET. VB acknowledges support from the Catalan DEC grant 2017 SGR 643.

References

Aharonian, F. A. 2004, Very High Energy Cosmic Gamma Radiation: A Crucial Window on the Extreme Universe (World Scientific Publishing Co)
Araudo, A. T., Bosch-Ramon, V., & Romero, G. E. 2009, A&A, 503, 673
Begelman, M. C., King, A. R., & Pringle, J. E. 2006, MNRAS, 370, 399
Bosch-Ramon, V., & Barkov, M. V. 2016, A&A, 590, A119
Bosch-Ramon, V., & Khangulyan, D. 2009, Int. J. Mod. Phys. D, 18, 347
Crowther, P. A., Lennon, D. J., & Walborn, N. R. 2006, A&A, 446, 279
de Koter, A., Vink, J. S., & Muijres, L. 2008, in Clumping in Hot-Star Winds, eds. W. R. Hamann, A. Feldmeier, & L. M. Oskinova, 47
Dermer, C. D., & Schlickeiser, R. 2002, ApJ, 575, 667
Drury, L. O. 1983, Rep. Prog. Phys., 46, 973
Dubus, G., Cerutti, B., & Henri, G. 2010, MNRAS, 404, L55
El Mellah, I., Sundqvist, J. O., & Keppens, R. 2018, MNRAS, 475, 3240
El Mellah, I., Sundqvist, J. O., & Keppens, R. 2019a, A&A, 622, L3
El Mellah, I., Sander, A. A. C., Sundqvist, J. O., & Keppens, R. 2019b, A&A, 622, A189
Fender, R. P., Belloni, T. M., & Gallo, E. 2004, MNRAS, 355, 1105
Friend, D. B., & Castor, J. I. 1982, ApJ, 261, 293
Gies, D. R., & Bolton, C. T. 1986, ApJ, 304, 389
Gould, R. J., & Schréder, G. P. 1967, Phys. Rev., 155, 1408
Heap, S. R., Lanz, T., & Hubeny, I. 2006, ApJ, 638, 409
Khangulyan, D., Aharonian, F., & Bosch-Ramon, V. 2008, MNRAS, 383, 467
Khangulyan, D., Aharonian, F. A., & Kelner, S. R. 2014, ApJ, 783, 100
Khangulyan, D., Bosch-Ramon, V., & Uchiyama, Y. 2018, MNRAS, 481, 1455
Lamers, H. J. G. L. M., & Cassinelli, J. P. 1999, Introduction to Stellar Winds (Cambridge University Press)
Leitherer, C., & Robert, C. 1991, ApJ, 377, 629
Longair, M. S. 1981, High Energy Astrophysics (Cambridge University Press)
Luque-Escamilla, P. L., Martí, J., & Martínez-Aroza, J. 2015, A&A, 584, A122
Miller-Jones, J. C. A., Blundell, K. M., Rupen, M. P., et al. 2004, ApJ, 600, 368
Mioduszewski, A. J., Rupen, M. P., Hjellming, R. M., Pooley, G. G., & Waltman, E. B. 2001, ApJ, 553, 766
Moffat, A. F. J. 2008, in Clumping in Hot-Star Winds, eds. W. R. Hamann, A. Feldmeier, & L. M. Oskinova, 17
Mokiem, M. R., de Koter, A., Vink, J. S., et al. 2007, A&A, 473, 603
Molina, E., & Bosch-Ramon, V. 2018, A&A, 618, A146
Monceau-Baroux, R., Porth, O., Meliani, Z., & Keppens, R. 2014, A&A, 561, A30
Muijres, L. E., de Koter, A., Vink, J. S., et al. 2011, A&A, 526, A32
Muijres, L. E., Vink, J. S., de Koter, A., Müller, P. E., & Langer, N. 2012, A&A, 537, A37
Owocki, S. P., & Cohen, D. H. 2006, ApJ, 648, 565
Owocki, S. P., Romero, G. E., Townsend, R. H. D., & Araudo, A. T. 2009, ApJ, 696, 690
Pacholczyk, A. G. 1970, Radio Astrophysics. Nonthermal Processes in Galactic and Extragalactic Sources (W. H. Freeman & Company)
Pauldrach, A., Puls, J., & Kudritzki, R. P. 1986, A&A, 164, 86
Perucho, M., & Bosch-Ramon, V. 2008, A&A, 482, 917
Perucho, M., & Bosch-Ramon, V. 2012, A&A, 539, A57
Perucho, M., Bosch-Ramon, V., & Khangulyan, D. 2010, A&A, 512, L4
Pudritz, R. E., Hardcastle, M. J., & Gabuzda, D. C. 2012, Space Sci. Rev., 169, 27
Puls, J., Kudritzki, R. P., Herrero, A., et al. 1996, A&A, 305, 171
Reitberger, K., Kissmann, R., Reimer, A., & Reimer, O. 2014, ApJ, 789, 87
Romero, G. E., & Orellana, M. 2005, A&A, 439, 237
Rybicki, G. B., & Lightman, A. P. 1986, Radiative Processes in Astrophysics (Wiley-VCH)
Sander, A. A. C., Fürst, F., Kretschmar, P., et al. 2018, A&A, 610, A60
Sikora, M., Madejski, G., Moderski, R., & Poutanen, J. 1997, ApJ, 484, 108
Stirling, A. M., Spencer, R. E., de la Force, C. J., et al. 2001, MNRAS, 327, 1273
Yoon, D., Zdziarski, A. A., & Heinz, S. 2016, MNRAS, 456, 3638
Zanin, R., Fernández-Barral, A., de Oña Wilhelmi, E., et al. 2016, A&A, 596, A55
Zdziarski, A. A., Malyshev, D., Chernyakova, M., & Pooley, G. G. 2017, MNRAS, 471, 3657
Zdziarski, A. A., Malyshev, D., Dubus, G., et al. 2018, MNRAS, 479, 4399

4

A DYNAMICAL AND RADIATION MODEL OF PULSAR-STAR COLLIDING WINDS ALONG THE ORBIT

This Chapter contains the published version of Molina and Bosch-Ramon (2020, A&A, 641, A84).

In this work, we adapt the hydrodynamical and radiative model developed in Chapters 2 and 3 for its use in pulsar wind binaries, with a specific application to the case of LS 5039. From the hydrodynamical point of view, the outflows of pulsar wind binaries differ from the microquasar jets in that their motion takes place mainly in the orbital plane, and that they are typically less collimated. In this scenario, our phenomenological trajectory computation is in reasonably good agreement with numerical simulations (Bosch-Ramon et al. 2015) up to distances of several orbital separations.

Regarding the non-thermal features of the model, it now considers two sites for particle acceleration, one at the two-wind standoff location and the other one at the Coriolis shock produced when orbital effects start to dominate the flow propagation. The non-thermal energy content and intrinsic emission are more prominent downstream of the Coriolis shock than upstream of it. Nonetheless, for those orbital phases close to the inferior conjunction of the pulsar, the observed emission is dominated by the inner regions of the outflow, where Doppler boosting is more important due to higher flow speeds. Similarly as with HMMQ jets, the spiral-like structure of the outflow can be traced via its synchrotron radio emission for sufficiently high magnetic fields.

The application of the model to LS 5039 yields a reasonably good explanation of the general non-thermal behavior of this source, especially at X-ray and VHE gamma-ray energies. The main discrepancy with the observations comes, as in previous works (e.g., Takahashi et al. 2009; Zabalza et al. 2013; Dubus et al. 2015), from the underestimation of the MeV emission, which possibly requires accounting for the emission of the unshocked pulsar wind to be properly characterized (Bosch-Ramon 2021).

A&A 641, A84 (2020)
https://doi.org/10.1051/0004-6361/202038417

Astronomy & Astrophysics

A dynamical and radiation semi-analytical model of pulsar-star colliding winds along the orbit: Application to LS 5039

E. Molina and V. Bosch-Ramon

Departament de Física Quàntica i Astrofísica, Institut de Ciències del Cosmos (ICCUB), Universitat de Barcelona (IEEC-UB),
Martí i Franquès 1, 08028 Barcelona, Spain
e-mail: `emolina@fqa.ub.edu, vbosch@fqa.ub.edu`

Received 14 May 2020 / Accepted 30 June 2020

ABSTRACT

Context. Gamma-ray binaries are systems that emit nonthermal radiation peaking at energies above 1 MeV. One proposed scenario to explain their emission consists of a pulsar orbiting a massive star, with particle acceleration taking place in shocks produced by the interaction of the stellar and pulsar winds.

Aims. We develop a semi-analytical model of the nonthermal emission of the colliding-wind structure, which includes the dynamical effects of orbital motion. We apply the model to a general case and to LS 5039.

Methods. The model consists of a one-dimensional emitter, the geometry of which is affected by Coriolis forces owing to orbital motion. Two particle accelerators are considered: one at the two-wind standoff location and the other one at the turnover produced by the Coriolis force. Synchrotron and inverse Compton emission is studied taking into account Doppler boosting and absorption processes associated to the massive star.

Results. If both accelerators are provided with the same energy budget, most of the radiation comes from the region of the Coriolis turnover and beyond, up to a few orbital separations from the binary system. Significant orbital changes of the nonthermal emission are predicted in all energy bands. The model allows us to reproduce some of the LS 5039 emission features, but not all of them. In particular, the MeV radiation is probably too high to be explained by our model alone, the GeV flux is recovered but not its modulation, and the radio emission beyond the Coriolis turnover is too low. The predicted system inclination is consistent with the presence of a pulsar in the binary.

Conclusions. The model is quite successful in reproducing the overall nonthermal behavior of LS 5039. Some improvements are suggested to better explain the phenomenology observed in this source, such as accounting for particle reacceleration beyond the Coriolis turnover, unshocked pulsar wind emission, and the three-dimensional extension of the emitter.

Key words. gamma rays: stars – radiation mechanisms: non-thermal – stars: winds, outflows – stars: individual: LS 5039

1. Introduction

Gamma-ray binaries are binary systems consisting of a compact object, which can be a black hole or a neutron star, and a nondegenerate star. These sources emit nonthermal radiation from radio up to very high-energy (VHE) gamma rays (above 100 GeV), and the most powerful ones host massive stars (see Dubus 2013; Paredes & Bordas 2019, for a review). The main difference with X-ray binaries, which may also show persistent or flaring gamma-ray activity (see, e.g., Zanin et al. 2016; Zdziarski et al. 2018, for Cygnus X-1 and Cygnus X-3, respectively, and references therein), is that in X-ray binaries the (nonstellar) emission reaches its maximum at X-rays, whereas gamma-ray binaries emit most of their radiation at energies above 1 MeV.

Thus far, there are nine confirmed high-mass gamma-ray binaries for which emission above 100 MeV has been detected: LS I +61 303 (Tavani et al. 1998), LS 5039 (Paredes et al. 2000), PSR B1259-63 (Aharonian et al. 2005), HESS J0632+057 (Aharonian et al. 2007; Hinton et al. 2009), 1FGL J1018.6-5856 (Fermi LAT Collaboration 2012), HESS J1832-093 (Hess & Abramowski 2015; Eger et al. 2016), LMC P3 (Corbet et al. 2016), PSR J2032+4127 (Abeysekara et al. 2018), and 4FGL J1405-6119 (Corbet et al. 2019). There are other candidate systems with a pulsar orbiting a massive star that exhibit nonthermal radio emission, but for which gamma rays have yet to be detected (see Dubus et al. 2017, and references therein).

The two most common scenarios proposed to explain the observed nonthermal emission in gamma-ray binaries involve either a microquasar, which generates nonthermal particles in relativistic jets powered by accretion onto a compact object (see, e.g., Bosch-Ramon & Khangulyan 2009, for a thorough study of the scenario), or a nonaccreting pulsar, in which energetic particles are accelerated through shocks produced by the interaction of the stellar and pulsar winds (e.g., Maraschi & Treves 1981; Leahy 2004; Dubus 2006; Khangulyan et al. 2007; Sierpowska-Bartosik & Torres 2007; Zabalza et al. 2013; Takata et al. 2014; Dubus et al. 2015). With the contribution of orbital motion at large scales, this wind interaction leads to the formation of a spiral-like structure that is mainly composed of shocked pulsar material that can extend up to several dozens of times the orbital separation (see, e.g., Bosch-Ramon & Barkov 2011; Bosch-Ramon et al. 2012, 2015; Barkov & Bosch-Ramon 2016, for an analytical description and numerical simulations of this structure).

In this work, we present a model to describe the broadband nonthermal emission observed in gamma-ray binaries through the interaction of the stellar and pulsar winds. The novelty of this model, with respect to previous works, is the application of

Table 1. Parameters that are used in this work.

	Parameter	Value
Star	Temperature $T_\star$	4×10^4 K
	Luminosity $L_\star$	10^{39} erg s^{-1}
	Mass-loss rate $\dot{M}_{\rm w}$	$3 \times 10^{-7}\ M_\odot$ yr^{-1}
	Wind speed $v_{\rm w}$	3×10^8 cm s^{-1}
Pulsar	Luminosity $L_{\rm p}$	3×10^{36} erg s^{-1}
	Wind Lorentz factor $\Gamma_{\rm p}$	10^5
System	Orbital separation D	3×10^{12} cm
	Orbital period T	5 days
	Orbital eccentricity e	0
	Distance to the observer d	3 kpc
	Nonthermal fraction $\eta_{\rm NT}$	0.1
	Acceleration efficiency $\eta_{\rm acc}$	0.1
	Injection power-law index p	-2
	Coriolis turnover speed $v_{\rm Cor}$	3×10^9, 10^{10} cm s^{-1}
	Magnetic fraction η_B	10^{-3}, 10^{-1}
	System inclination i	30°, 60°

Notes. The last three are those for which different values are explored.

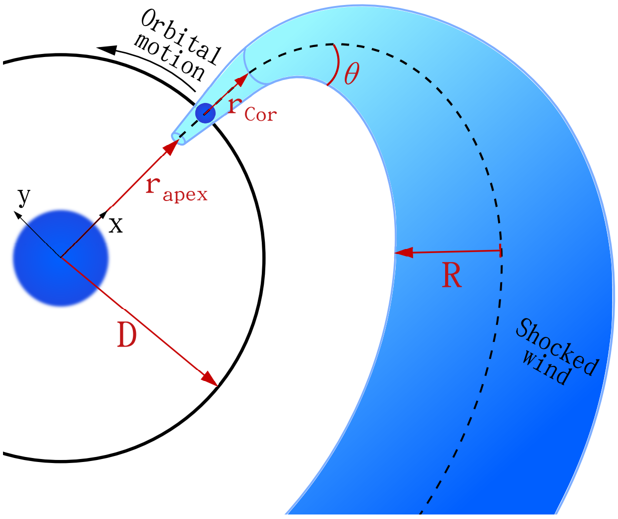

Fig. 1. Schematic zenithal view of the studied scenario (not to scale). Only a fraction of the orbit is shown for clarity.

a semi-analytical hydrodynamical approach to study the combined effect of the stellar wind and orbital motion on the emitter, which is assumed to be one-dimensional (1D; see Molina & Bosch-Ramon 2018; Molina et al. 2019, for a similar model in a microquasar scenario). The paper is structured as follows: the details of the model are given in Sect. 2, the results for a generic system are shown in Sect. 3, a specific application to the case of LS 5039 is done in Sect. 4, and a summary and a discussion are given in Sect. 5.

2. Description of the general model

As a representative situation, we study a binary system made of a massive O-type star and a pulsar that orbit around each other with a period of $T = 5$ days. The orbit is taken circular for simplicity, with an orbital separation of $D = 3 \times 10^{12}$ cm ≈ 0.2 AU. The stellar properties are typical for a main sequence O-type star (Muijres et al. 2012), namely a temperature of $T_\star = 40\,000$ K and a luminosity of $L_\star = 10^{39}$ erg s^{-1}. For simplicity, we model the stellar wind as an isotropic supersonic outflow with a velocity of $v_{\rm w} = 3 \times 10^8$ cm s^{-1} and a mass-loss rate of $\dot{M}_{\rm w} = 3 \times 10^{-7}\ M_\odot$ yr^{-1}. The wind velocity is taken constant and not following the classical β-law for massive stars (e.g., Pauldrach et al. 1986), as the effect of considering such a velocity profile for standard β values is small for the purpose of this work. The pulsar has a spin-down luminosity of $L_{\rm p} = 3 \times 10^{36}$ erg s^{-1}, which is taken here as equal to the kinetic luminosity of the pulsar wind. The latter is assumed to be ultra-relativistic and isotropic, with Lorentz factor $\Gamma_{\rm p} = 10^5$. The distance to the system is taken to be $d = 3$ kpc, and the inclination i is left as a free parameter. A list of the parameter values used for a generic gamma-ray binary can be found in Table 1, and a sketch of the studied scenario is presented in Fig. 1. Throughout this section, the notation $u = \|\vec{u}\|$ is used to refer to a vector norm. Also, we use primed quantities in the fluid frame (FF), and unprimed ones in the frame of the star, assumed here to be the laboratory frame (LF).

2.1. Dynamics

The interaction of the stellar and the pulsar winds produces an interface region between the two where the shocked flow pressures are in equilibrium: the so-called contact discontinuity (CD). Close to the binary system, where the orbital motion can be neglected, the shape of this surface is characterized by the pulsar-to-stellar wind momentum rate ratio, defined as

$$\eta = \frac{L_{\rm p}}{\dot{M}_{\rm w} v_{\rm w} c} \tag{1}$$

for $\Gamma_{\rm p} \gg 1$. The asymptotic half-opening angle of the CD can be approximated by the following expression from Eichler & Usov (1993), which is in good agreement with numerical simulations (e.g., Bogovalov et al. 2008):

$$\theta = 28.6^\circ (4 - \eta^{2/5}) \eta^{1/3}\ . \tag{2}$$

The apex of the CD, where the two winds collide frontally, is located along the star-pulsar direction at a distance from the star of $r_{\rm apex} = D/(1 + \sqrt{\eta})$, with D being the orbital separation. For the adopted parameters, we obtain $\eta = 0.018$, $\theta = 28.7^\circ$, and $r_{\rm apex} = 0.88D = 2.6 \times 10^{12}$ cm, the latter being constant owing to the circularity of the orbit.

The star is located at the origin of the coordinate system, which co-rotates with the pulsar. The x-axis is defined as the star-pulsar direction, and the y-axis is perpendicular to it and points in the direction of the orbital motion. We model the evolution of the shocked stellar and pulsar winds in the inner interaction region as a straight conical structure of half-opening angle θ and increasing radius R, the onset of which is at $x = r_{\rm apex}$, where it has a radius of $R_0 = D - r_{\rm apex}$, roughly corresponding to the characteristic size of the CD at its apex. The shocked flows are assumed to move along the x direction in this region (i.e., the orbital velocity is neglected here with respect to the wind speed), until they reach a point where their dynamics start to be dominated by orbital effects, the Coriolis turnover. Beyond this point, the CD is progressively bent in the -y direction due to the asymmetric interaction with the stellar wind, which arises from Coriolis forces (see Fig. 1 for an schematic view). As a result, the shocked flow structure acquires a spiral shape at large scales. One can estimate the distance of the Coriolis turnover to the pulsar $r_{\rm Cor}$ by following the analytical prescription in Bosch-Ramon & Barkov (2011), which comes from equating the total pulsar wind pressure to the stellar wind ram pressure due to the Coriolis effect (for $\Gamma_p \gg 1$):

$$\frac{L_p}{4\pi c r_{\rm Cor}^2} = \frac{\rho_w(D)}{(1+r_{\rm Cor}/D)^2}\left(\frac{4\pi}{T}\right)^2 r_{\rm Cor}^2\,, \tag{3}$$

where $\rho_w(r) = \dot{M}_w/4\pi r^2 v_w$ is the stellar wind density at a distance r from the star. Although approximate, this expression agrees well with results from 3D numerical simulations (Bosch-Ramon et al. 2015). Numerically solving Eq. (3) for our set of parameters yields $r_{\rm Cor} = 0.94D$. We note that in the case of an elliptical system $r_{\rm Cor}$ changes along the orbit.

The radiation model explained in Sect. 2.2 focuses on the shocked pulsar material flowing inside the CD. The values of the Lorentz factor of this fluid are set to increase linearly with distance from the CD apex ($\Gamma_0 = 1.06, v_0 = c/3$) to the Coriolis turnover ($\Gamma = 4, v = 0.97c$), based on the simulations by Bogovalov et al. (2008). Beyond the Coriolis turnover, and due to some degree of mixing between the pulsar and stellar winds (see, e.g., the numerical simulations in Bosch-Ramon et al. 2015), we fix the shocked pulsar wind speed $v_{\rm Cor}$ to a constant value that is left as a free parameter in our model, and could account for different levels of mixing. The shocked stellar wind that surrounds the shocked pulsar wind plays the role of a channel through which the former flows, and may have a much lower speed. This channel is assumed to effectively transfer the lateral momentum coming from the unshocked stellar wind to the shocked pulsar wind.

The trajectory of the shocked winds flowing away from the binary, which are assumed to form a (bent) conical structure, is determined by accounting for orbital motion and momentum balance between the upstream shocked pulsar wind and the unshocked stellar wind, with a thin shocked stellar wind channel playing the role of a mediator. This conical structure is divided into 2000 cylindrical segments of length $dl = 0.05D$, amounting to a total length of $100D$. Initially, all the shocked material moves along the x axis between $x = r_{\rm apex}$ and $x = D + r_{\rm Cor}$. At the latter point, its position and momentum are, in Cartesian coordinates of the co-rotating frame,

$$\begin{aligned}\vec{r} &= (D + r_{\rm Cor}, 0)\\ \vec{P} &= (\dot{P}dt, 0)\,,\end{aligned} \tag{4}$$

where $\dot{P}$ is the momentum rate of the shocked flow, which we estimate as:

$$\dot{P} = \frac{L_p}{c}. \tag{5}$$

For simplicity, we are not considering the contribution of the momentum of the stellar wind loaded through mixing into the pulsar wind before the Coriolis turnover. This contribution depends on the level of mixing, and could be as high as $\Omega\dot{M}_w v_w$, with $\Omega = R^2/4(D + r_{\rm Cor})^2$ being the solid angle fraction subtended by the shocked pulsar wind at the Coriolis turnover, as seen from the position of the star. We note, nonetheless, that the inclusion of the stellar wind contribution to $\dot{P}$ has a modest impact on the radiation predictions of the model and can be neglected at this stage.

The unshocked stellar wind velocity in the co-rotating frame has components in both the x and the y directions:

$$\vec{\hat{v}}_w = v_w\frac{(x,y)}{r} + \omega r\frac{(y,-x)}{r}\,, \tag{6}$$

where ω is the orbital angular velocity, and the hat symbol is used to distinguish $\hat{v}_w$ from the purely radial component of the wind, v_w. In a stationary configuration, the force that the unshocked stellar wind exerts onto each segment of the shocked wind structure is

$$\vec{F_w} = \rho_w \hat{v}_w^2 S\,\sin\alpha\frac{\vec{\hat{v}}_w}{\hat{v}_w}\,, \tag{7}$$

with α being the angle between $\vec{\hat{v}}_w$ and the shocked pulsar wind velocity $\vec{v}$, and $S\,\sin\alpha = 2R dl\sin\alpha$ the segment lateral surface normal to the stellar wind direction. The component of $\vec{F_w}$ parallel to the fluid direction is assumed to be mostly converted into thermal pressure, whereas the perpendicular component $\vec{F_w^\perp} = \vec{F_w}\sin\alpha$ modifies the segment momentum direction. Thus, the interaction with the stellar wind only reorients the fluid, but it does not change its speed beyond the Coriolis turnover[1].

We find the conditions for the subsequent segments by applying the following recursive relations:

$$\begin{aligned}\vec{P}_{i+1} &= \vec{P}_i + \vec{F_w^\perp}dt_i\\ \vec{v}_{i+1} &= v_i\frac{\vec{P}_i}{P_i}\\ \vec{r}_{i+1} &= \vec{r}_i + \vec{v}_i dt_i\,,\end{aligned} \tag{8}$$

where v_i is the shocked pulsar wind velocity in each segment, and $dt_i = dl/v_i$ is the segment advection time. This procedure yields a fluid trajectory semi-quantitatively similar to that obtained from numerical simulations within approximately the first spiral turn (e.g., Bosch-Ramon et al. 2015).

2.2. Characterization of the emitter

The nonthermal emission is assumed to take place in the shocked pulsar wind, which moves through the shocked stellar wind channel and follows the trajectory defined in the previous section. We consider a nonthermal particle population consisting only of electrons and positrons. These are radiatively more efficient than accelerated protons (e.g., Bosch-Ramon & Khangulyan 2009), but the presence of the latter cannot be discarded. Particles are accelerated at two different regions where strong shocks develop: the pulsar wind termination shock, located here at the CD apex; and the shock that forms in the Coriolis turnover (as in Zabalza et al. 2013, hereafter the Coriolis shock). In our general model, we consider for simplicity that both regions have the same power injected into nonthermal particles (in the LF), taken as a fraction of the total pulsar wind luminosity: $L_{\rm NT} = \eta_{\rm NT}L_p$, with $\eta_{\rm NT} = 0.1$. They also have the same acceleration efficiency $\eta_{\rm acc} = 0.1$, which defines the energy gain rate $\dot{E}'_{\rm acc} = \eta_{\rm acc}ecB'$ of particles for a given magnetic field B'. The latter is defined through its energy density being a fraction of the total energy density at the CD apex (indicated with the subscript 0):

$$\frac{B_0'^2}{8\pi} = \eta_B\frac{L_p}{\pi R_0^2 v_0\Gamma_0^2}\,. \tag{9}$$

The magnetic field is assumed toroidal, and therefore it evolves along the emitter as $B' \propto R^{-1}\Gamma^{-1}$. For simplicity, we assume

---

[1] There must be some acceleration of the shocked flow away from the binary as a pressure gradient is expected, but for simplicity this effect is neglected here.

that all the flow particles at the Coriolis turnover are reprocessed by the shock there, leading to a whole new population of particles. This means that the particle population beyond the Coriolis shock only depends on the properties of the latter, and is independent of the particle energy distribution coming from the initial shock at the CD apex. This assumption divides the emitter into two independent and distinct regions: one region between the CD apex and the Coriolis turnover (hereafter the inner region), and one beyond the latter (hereafter the outer region). We recall that the inner region has a velocity profile corresponding to a linear increase in Γ, whereas in the outer region the fluid moves at a constant speed (see Sect. 2.1).

To compute the particle evolution, the emitter is divided into 1000 segments of length $0.1D$, in order to account for the same total length as in Sect 2.1. An electron and positron population is injected at each accelerator following a power-law distribution in the energy E', with an exponential cutoff and spectral index p:

$$Q'(E') \propto E'^{p} \exp\left(-\frac{E'}{E'_{\rm max}}\right), \tag{10}$$

where $E'_{\rm max}$ is the cutoff energy obtained by comparing the acceleration timescale, $t'_{\rm acc} = E'/|\dot{E}'_{\rm acc}|$, with the cooling and diffusion timescales, $t'_{\rm cool} = E'/|\dot{E}'|$ and $t'_{\rm diff} = 3R'^2eB'/2cE'$, respectively ($R$ is the perpendicular size and thus is taken $R' = R$). We adopt $p = -2$ because it allows for a substantial power to be available for gamma-ray emission. Harder, and also a bit softer electron distributions would also be reasonable options. The particle injection is normalized by the total available power $L'_{\rm NT} = L_{\rm NT}/\Gamma^2$. We note that $E'_{\rm max}$ and $L'_{\rm NT}$ are not the same for both accelerators, since their properties differ. Particles are advected between subsequent segments following the bulk motion of the fluid (see Appendix B2 in de la Cita et al. 2016), and they cool down via adiabatic, synchrotron, and inverse Compton (IC) losses as they move along the emitter. The particle energy distribution at each segment is computed in the FF following the same recursive method as in Molina & Bosch-Ramon (2018), which yields, for a given segment k:

$$N'_{\rm k}(E'_{\rm k}) = N'_0(E'_0)\prod_{\rm i=k}^{1}\frac{\dot{E}'_{\rm i}(E'_{\rm i-1})}{\dot{E}'_{\rm i}(E'_{\rm i})}\,, \tag{11}$$

where $E'_{\rm k}$ is the energy of a given particle at the location of segment k, and $E'_{\rm i}$ is the energy that this same particle had when it was at the position of segment i, with $i \leq k$ (we note that $E'_{\rm i} > E'_{\rm k}$ due to energy losses).

For every point where we have the particle distribution, the synchrotron spectral energy distribution (SED) is computed following Pacholczyk (1970). The IC SED is obtained from the numerical prescription developed by Khangulyan et al. (2014) for a monodirectional field of stellar target photons with a blackbody spectrum. The distribution of electrons is isotropic in the FF. These SEDs are then corrected by Doppler boosting and absorption processes, the latter consisting of gamma-gamma absorption with the stellar photons (e.g. Gould & Schréder 1967), and free-free absorption with the stellar wind ions (e.g., Rybicki & Lightman 1986). We do not consider emission from secondary particles generated via the interaction of gamma rays with stellar photons, although it may have a nonnegligible impact on our results (see discussion in Sect. 5.2). Partial occultation of the emitter by the star is also taken into account, although it is only noticeable for very specific system-observer configurations. For a more detailed description of the SED computation we refer the reader to Molina et al. (2019).

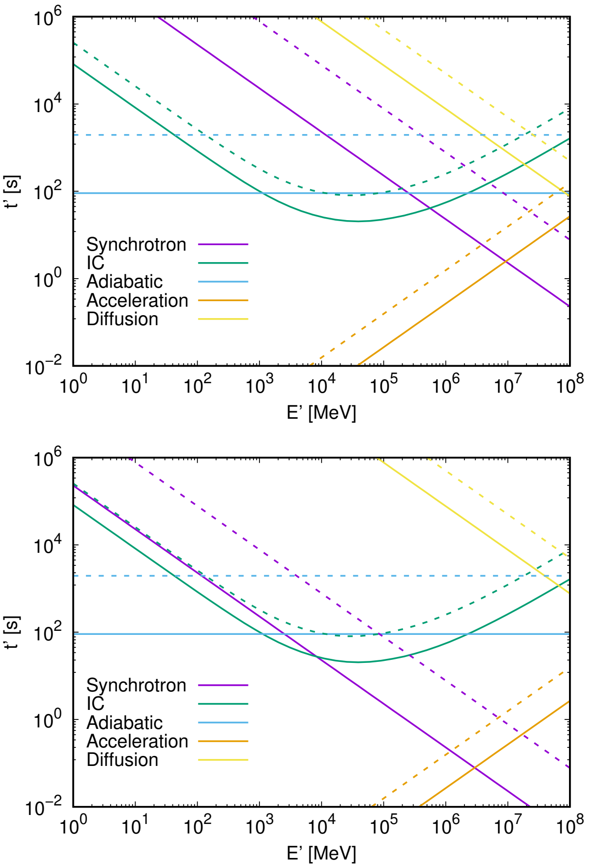

Fig. 2. Characteristic timescales in the FF for $v_{\rm Cor} = 3 \times 10^9$, and $\eta_B = 10^{-3}$ (*top panel*) and 10^{-1} (*bottom panel*). Solid and dashed lines represent the values at the CD apex and the Coriolis turnover locations, respectively.

3. General results

For the results presented in this section, we make use of the parameter values listed in Table 1. The orbital phase Φ is defined such that the pulsar is in the inferior conjunction (INFC) for $\Phi = 0$, and in the superior conjunction (SUPC) for $\Phi = 0.5$.

3.1. Energy losses and particle distribution

Figure 2 shows the characteristic timescales in the FF for the cooling, acceleration, and diffusion processes, for $v_{\rm Cor} = 3 \times 10^9\,{\rm cm\,s^{-1}}$, and $\eta_B = 10^{-3}$ and 10^{-1}, which correspond to initial magnetic fields of $B'_0 = 4.15$ G and 41.5 G, respectively. In general, particle cooling is dominated by adiabatic losses at the lowest energies, IC losses at intermediate energies, and synchrotron losses at the highest ones unless a very small magnetic field with $\eta_B < 10^{-5}$ is assumed. The exact energy values at which the different cooling processes dominate depend on η_B, and also on whichever emitter region we are looking at. Given the dependency of the synchrotron and acceleration timescales on the magnetic field, and that the latter decreases linearly with distance, $E'_{\rm max}$ is higher at the Coriolis turnover than at the CD apex (see where the synchrotron and acceleration lines intersect in Fig. 2), allowing particles to reach higher energies at the location of the former. The larger region size involved and longer accumulation time, combined with the lower energy losses farther

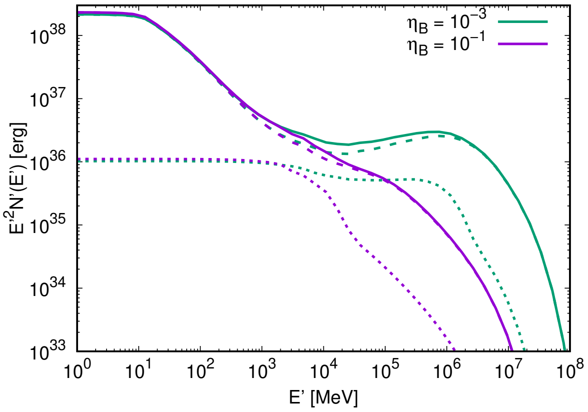

Fig. 3. Particle energy distribution in the FF for $v_{\rm Cor} = 3 \times 10^9\,{\rm cm\,s^{-1}}$, and $\eta_B = 10^{-3}$ (green lines) and 10^{-1} (purple lines). The contributions of the inner and outer regions are represented with dotted and dashed lines, respectively, and their sum is shown by the solid lines.

from the star, make the nonthermal particle distribution to be dominated by the outer region of the emitter, with just a small contribution from the inner part at middle energies, as seen in Fig. 3 (we recall that both regions are assumed to have the same injection power in the LF). The only significant effect of increasing the post-Coriolis shock speed to $v_{\rm Cor} = 10^{10}\,{\rm cm\,s^{-1}}$ is the increase of the adiabatic losses by a factor of $\sim$3 at the Coriolis turnover location and beyond (not shown in the figures). This results in a decrease of $N'(E')$ for $E' \lesssim 100$ MeV, where adiabatic cooling (and particle escape) dominates.

3.2. Spectral energy distribution

The synchrotron and IC SEDs, as seen by the observer, are shown in Figs. 4 and 5 for $v_{\rm Cor} = 3 \times 10^9\,{\rm cm\,s^{-1}}$ and $v_{\rm Cor} = 10^{10}\,{\rm cm\,s^{-1}}$, respectively. We take a representative orbital phase of $\Phi = 0.3$, $i = 60°$, and $\eta_B = 10^{-3}$ and 10^{-1}. The overall SED has the typical shape for synchrotron and IC emission, with the magnetic field changing the relative intensity of each component. The IC SED is totally dominated by the outer region even if it is farther from the star and the target photon field is less dense than in the inner region. This happens because the former contains many more (accumulated) nonthermal particles that scatter stellar photons (see Fig. 3), and also because the ratio of synchrotron to IC cooling is smaller than in the inner region (therefore, more energy is emitted in the form of IC photons at the electron energies where radiative losses dominate). Synchrotron radiation, on the other hand, is more equally distributed between the two regions. We note, however, that Doppler boosting could make the inner region dominate both the IC and synchrotron emission in a broad energy range for orbital phases close to the INFC (see Sect. 3.3, and the discussion in Sect. 5.1).

3.3. Orbital variability

Light curves for two different system inclinations, $i = 30°$ and $60°$, and post-Coriolis shock speeds, $v_{\rm Cor} = 3 \times 10^9\,{\rm cm\,s^{-1}}$ and $10^{10}\,{\rm cm\,s^{-1}}$, are shown in Figs. 6 and 7 for $\eta_B = 10^{-3}$. Aside from a change in the flux normalization, the behavior of the light curves is very similar for $\eta_B = 10^{-1}$. The modulation of X-rays is correlated with that of VHE gamma rays (top and bottom panels, respectively). Low-energy (LE) gamma rays (second panel) show a correlated modulation with VHE gamma rays and X-rays for $v_{\rm Cor} = 10^{10}\,{\rm cm\,s^{-1}}$, and an anti-correlated one for $v_{\rm Cor} = 3 \times 10^9\,{\rm cm\,s^{-1}}$. This change in the LE gamma-ray modulation is caused by a higher boosting (deboosting) of the outer region emission close to the INFC (SUPC) for $v_{\rm Cor} = 10^{10}\,{\rm cm\,s^{-1}}$, which overcomes the intrinsic IC modulation. This same effect is responsible for high-energy (HE) gamma rays (third panel) to not show a clear correlation with other energy bands at high $v_{\rm Cor}$, whereas they are anti-correlated with VHE gamma rays and X-rays (and correlated with LE gamma rays) at low $v_{\rm Cor}$. The fact that Doppler boosting modulates the emission in the opposite way as IC does also cause the predicted variability in the inner region as seen by the observer to significantly decrease with respect to its intrinsic one, whereas the effect on the outer region is less extreme due to a lower fluid speed. Asymmetries can be observed in the light curves due to the spiral trajectory of the emitter, although they are mild because most of the radiation is emitted within a distance of a few orbital separations from the star, where the spiral pattern is just beginning to form. The asymmetry only becomes more noticeable for HE gamma rays, $i = 60°$, and $v_{\rm Cor} = 10^{10}\,{\rm cm\,s^{-1}}$ (third panel in Fig. 7), in which a double peak structure can be seen. The proximity to the star also makes VHE emission close to the SUPC to be almost suppressed by gamma-gamma absorption.

Figures 8 and 9 show, for $i = 30°$ and $60°$ respectively, simulated radio sky maps at 5 GHz for $v_{\rm Cor} = 3 \times 10^9\,{\rm cm\,s^{-1}}$, and $\eta_B = 10^{-3}$ and 10^{-1}. They are obtained by convolving the

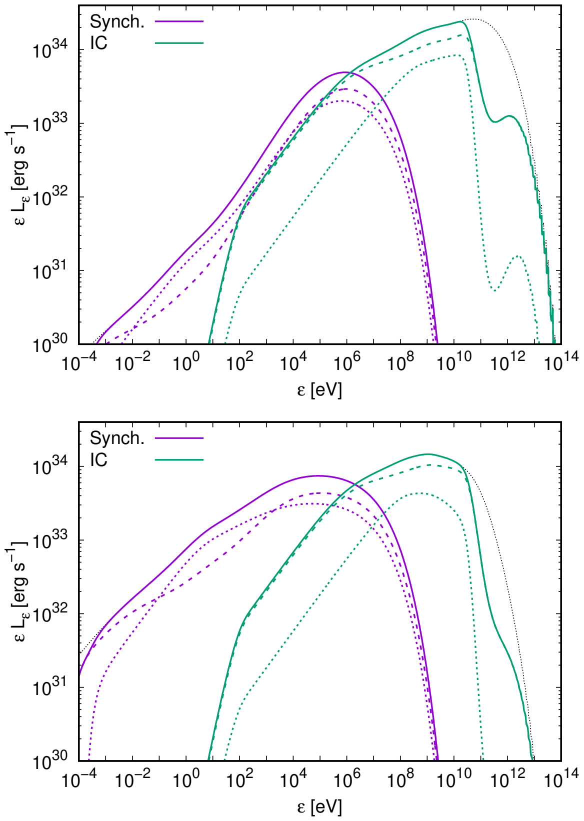

Fig. 4. Observer synchrotron (purple lines) and IC (green lines) spectral energy distributions for $\Phi = 0.3$, $v_{\rm Cor} = 3 \times 10^9\,{\rm cm\,s^{-1}}$, $i = 60°$, and $\eta_B = 10^{-3}$ (*top panel*) and 10^{-1} (*bottom panel*). The contributions of the inner and outer regions are represented with dotted and dashed lines, respectively. The black dotted lines show the total unabsorbed emission.

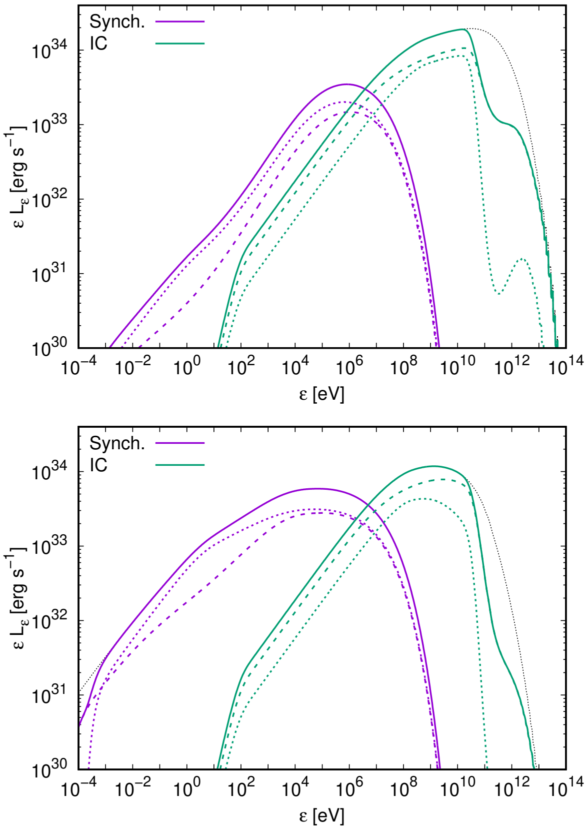

Fig. 5. Same as in Fig. 4, but for $v_{\rm Cor} = 10^{10}$ cm s^{-1}.

projected emission of each segment with a 2D Gaussian with increasing width to approximately simulate the segment perpendicular extension. The resulting maps are then convolved again with a Gaussian telescope beam of full width at half maximum (FWHM) = 0.5 mas. The contours are chosen so that the outermost one is 10 μJy beam^{-1}, on the order of the sensitivity of very-long-baseline interferometry (VLBI). Due to free-free absorption, radio emission from the inner region is highly suppressed, and what can be seen in the sky maps comes mostly from the outer region. In particular, the part of the outer region that contributes most to the radio emission is located close to the Coriolis shock, and has an angular size of ∼0.5 mas, which corresponds to a linear size of ∼1 AU at the assumed distance of 3 kpc. For high η_B and the assumed angular resolution, the initial part of the spiral structure can be traced in the radio images, especially for low inclinations. For small η_B, only the sites very close to the Coriolis shock contribute to the emission due to the low synchrotron efficiency farther away, and hints of a spiral outflow cannot be seen. Regardless of the magnetic field value, the position of the maximum of the radio emission shifts for as much as ≈1 mas at different orbital phases.

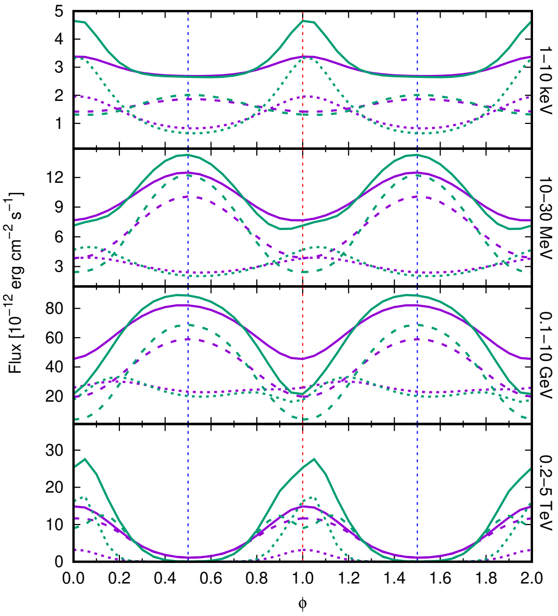

Fig. 6. Light curves at different energy ranges (indicated in the right side) for $\eta_B = 10^{-3}$, $v_{\rm Cor} = 3 \times 10^9$ cm s^{-1}, and $i = 30°$ (purple lines) and 60° (green lines). The contributions from the inner and outer regions are shown with dotted and dashed lines, respectively. The vertical dotted blue and red lines show the position of the superior and inferior conjunctions, respectively. Two orbits are represented for a better visualization.

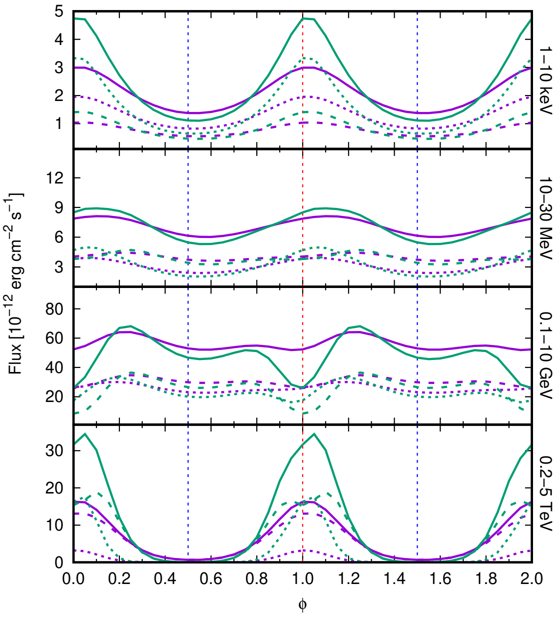

Fig. 7. Same as in Fig. 6, but for $v_{\rm Cor} = 10^{10}$ cm s^{-1}.

4. Application to LS 5039

LS 5039 is a widely studied binary system hosting a main sequence O-type star and a compact companion, the nature of which is still unclear. Low system inclinations ($i \lesssim 40°$) favor a black hole scenario, whereas higher inclinations favor the compact object to be a neutron star. Inclinations above ≈60° are unlikely due to the absence of X-ray eclipses in this system (Casares et al. 2005). LS 5039 has an elliptical orbit with a semi-major axis of $a \approx 2.4 \times 10^{12}$ cm, an eccentricity of $e = 0.35 \pm 0.04$, and a period of $T \approx 3.9$ days. The superior and inferior conjunctions are located at $\Phi = 0.058$ and 0.716, respectively, with $\Phi = 0$ corresponding to the periastron. The star has a

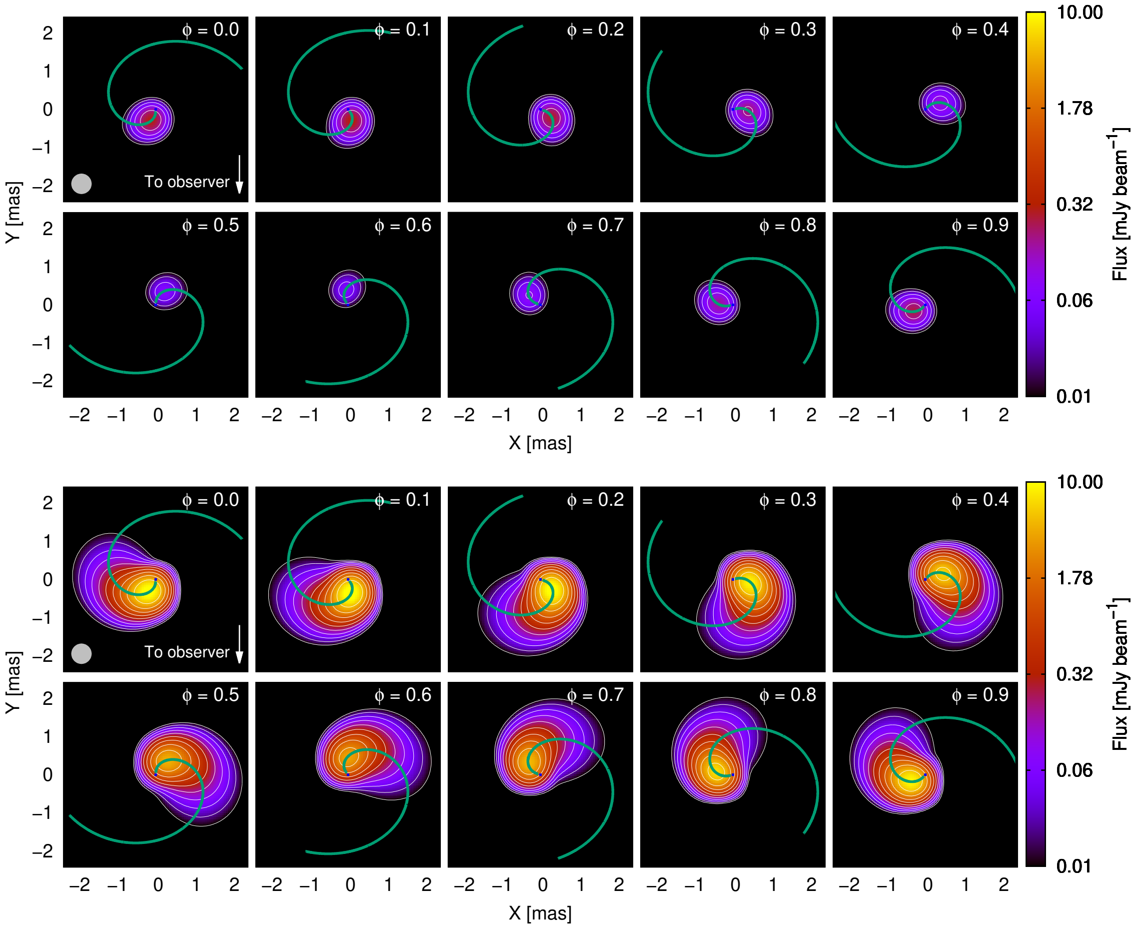

Fig. 8. Simulated radio sky maps at 5 GHz for different orbital phases, $v_{\rm Cor} = 3 \times 10^9$ cm s^{-1}, $i = 30°$, and $\eta_B = 10^{-3}$ (*top panel*) and 10^{-1} (*bottom panel*). The assumed telescope beam is shown as a gray circle in the bottom left corner of the first plot. The contour lines start at a flux of 10 μJy beam^{-1} and increase with a factor of 2. The star is represented (to scale) with a blue circle at (0,0), and the solid green line shows the axis of the conical emitter, the onset of which points toward the observer for $\Phi = 0$, and opposite to it for $\Phi = 0.5$.

luminosity of $L_\star = (7 \pm 1) \times 10^{38}$ erg s^{-1}, a radius of $R_\star = 9.3 \pm 0.7\,R_\odot$, and an effective temperature of $T_\star = (3.9 \pm 0.2) \times 10^4$ K (Casares et al. 2005). The stellar mass-loss rate obtained through Hα measurements is in the range $\dot{M}_{\rm w} = 3.7{-}4.8 \times 10^{-7}\,M_\odot$ yr^{-1} (Sarty et al. 2011), although this value would be overestimated if the wind were clumpy (e.g., Muijres et al. 2011). The assumption of an extended X-ray emitter (as it is the case in this work) places an upper limit for $\dot{M}_{\rm w}$ of up to a few times $10^{-7}\,M_\odot$ yr^{-1}, with the exact value depending on the system parameters (Szostek & Dubus 2011; see also Bosch-Ramon et al. 2007). The lack of thermal X-rays in the shocked stellar wind, in the context of a semi-analytical model of the shocked wind structure, puts an upper limit in the putative pulsar spin down luminosity of $L_{\rm p} \leq 6 \times 10^{36}$ erg s^{-1} (Zabalza et al. 2011). The latest *Gaia* DR2 parallax data (Gaia Collaboration 2018; Luri et al. 2018) sets a distance to the source of $d = 2.1 \pm 0.2$ kpc. The rest of the model parameters are unknown for LS 5039.

Carrying out a statistical analysis is hardly possible in our context, as we have many free parameters or parameters that are loosely constrained. Thus, we have looked for a set of parameter values that approximately reproduce the observational data, but the result should be considered just as illustrative of the model capability to reproduce the source behavior, and not a fit. We note that, for this purpose, we use a different value of the nonthermal power fraction for each accelerator ($\eta_{\rm NT}^A$ for the CD apex, and $\eta_{\rm NT}^B$ for the Coriolis shock). Table 2 shows all the model parameters used for the study of LS 5039, which are left constant throughout the whole orbit. For these parameters, we obtain $\eta = 0.035$, $\theta = 35.5°$, $0.55a \leq r_{\rm apex} \leq 1.14a$, and $1.03a \leq r_{\rm Cor} \leq 1.29a$, with the lower (upper) limits corresponding to the periastron (apastron).

Figure 10 shows, for $i = 60°$, the computed SED averaged over two wide phase intervals, one around the INFC ($0.45 < \Phi \leq 0.90$), and the other one around the SUPC ($0.90 < \Phi$ or $\Phi \leq 0.45$). Observational data points of *Suzaku* (Takahashi et al. 2009), COMPTEL (Collmar & Zhang 2014), *Fermi*/LAT (Fermi LAT Collaboration 2009; Hadasch et al. 2012), and H.E.S.S. (Aharonian et al. 2006) averaged over the same phase intervals are also plotted. The SEDs for different system inclinations in which a pulsar scenario is viable ($40° \lesssim i \lesssim 60°$) are not represented due their similarity to the one shown in Fig. 10. Synchrotron emission dominates for $\varepsilon \lesssim 10$ GeV, with IC only contributing significantly at VHE. With the exception of the COMPTEL energies ($1\,{\rm MeV} \lesssim \varepsilon \lesssim 30\,{\rm MeV}$), the SED reproduces reasonably well the magnitude of the observed fluxes, especially for X-rays and VHE gamma rays. At energies

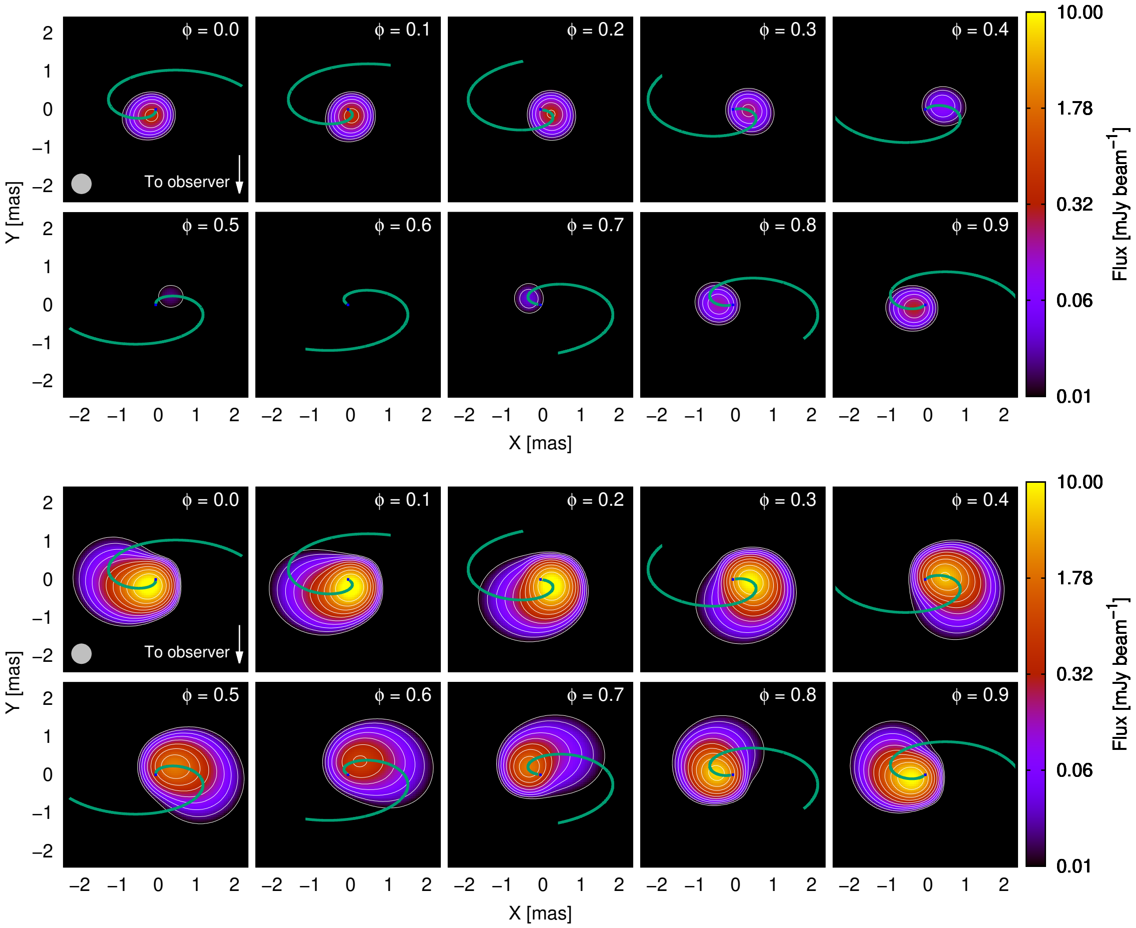

Fig. 9. Same as in Fig. 8, but for $i = 60°$.

of $100\,\mathrm{MeV} \lesssim \varepsilon \lesssim 10\,\mathrm{GeV}$, the model overpredicts (underpredicts) the emission around INFC (SUPC). The hard electron spectrum allows the IC component not to strongly overestimate the fluxes around 10 GeV, although we must note that IC emission from secondary pairs, not taken into account, may increase a bit the predicted fluxes.

The computed LS 5039 light curves are shown in Fig. 11 for the limits of the system inclination range allowed for a pulsar binary system ($40° \lesssim i \lesssim 60°$). Most of the emission comes from the outer region, regardless of the energy range. As in the SED, the model matches well the *Suzaku* and H.E.S.S observations, except for an underestimation of the latter fluxes around the SUPC. Inclinations close to 60° are favored by the presence of a double peak in the VHE fluxes, which is not reproduced for lower values of i. This double peak is originated by the effect of the system orientation in the IC emission and Doppler boosting; the peak at $\Phi \approx 0.5$ has a higher intrinsic IC emission, but a lower boosting than the peak at $\Phi \approx 0.85$. At *Fermi*/LAT energies, the model predicts a maximum in the light curve around the INFC and a minimum around the SUPC, contrary to what is observed. This happens because, in this energy range, the model emission is dominated by synchrotron radiation, which has a maximum around the INFC due to Doppler boosting. In the COMPTEL energy range, the relative behavior of the computed light curve is similar to the observations, although a factor of 4–5 lower.

Table 2. Parameters used for the study of LS 5039.

	Parameter	Value
Star	Temperature $T_\star$	4×10^4 K
	Luminosity $L_\star$	7×10^{38} erg s^{-1}
	Mass-loss rate $\dot{M}_\mathrm{w}$	$1.5 \times 10^{-7}\,M_\odot\,\mathrm{yr}^{-1}$
	Wind speed v_w	3×10^8 cm s^{-1}
Pulsar	Luminosity L_p	3×10^{36} erg s^{-1}
	Wind Lorentz factor Γ_p	10^5
System	Orbit semi-major axis a	2.4×10^{12} cm
	Orbital period T	3.9 days
	Orbital eccentricity e	0.35
	Distance to the observer d	2.1 kpc
	CD apex NT fraction η_NT^A	0.03
	Cor. shock NT fraction η_NT^B	0.18
	Acceleration efficiency η_acc	0.8
	Injection power-law index p	−1.3
	Coriolis turnover speed v_Cor	3×10^9 cm s^{-1}
	Magnetic fraction η_B	0.02
	System inclination i	40°, 60°

Figure 12 shows the computed radio sky map of LS 5039 at 5 GHz, for $i = 60°$ and a telescope beam with $FWHM = 0.5$ mas.

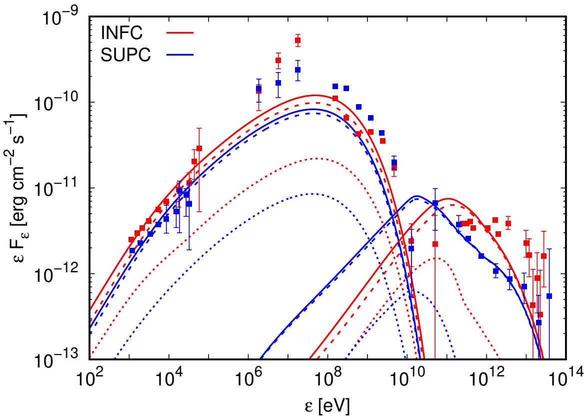

Fig. 10. Observer synchrotron and IC SEDs of LS 5039 for $i = 60°$, averaged over the INFC (red lines; $0.45 < \Phi \leq 0.90$) and SUPC (blue lines; $0.90 < \Phi$ or $\Phi \leq 0.45$) phase intervals. Dotted and dashed lines represent the contributions of the inner and outer regions, respectively. From left to right, data from *Suzaku*, COMPTEL, *Fermi*/LAT, and H.E.S.S. are also represented.

The sky map for $i = 40°$ is very similar and is not shown. Since we do not consider particle reacceleration beyond the Coriolis shock, these maps show the synchrotron emission up to a few orbital separations from the latter, as farther away synchrotron emission is too weak to significantly contribute to the radio flux. This lack of reacceleration does not allow for a meaningful comparison between our model and the observations. While the predicted total radio flux at 5 GHz, averaged over a whole orbit, is 0.10 mJy, the detected one is around 20 mJy (Moldón et al. 2012). The assumption of a hard particle spectrum ($p = -1.3$) needed to explain the SEDs makes most of the available power to go into the most energetic electrons and positrons. Therefore, only a small part of the energy budget goes to those lower energy particles responsible for the radio emission, which makes the latter considerably fainter than in the generic case studied in Sect. 3, in which $p = -2$. Despite the almost point-like and faint nature of the radio source, the emission maximum is displaced along the orbit by a similar angular distance of ≈1 mas.

5. Summary and discussion

We have developed a semi-analytical model, consisting of a 1D emitter, which can be used to describe both the dynamics and the radiation of gamma-ray binaries in a colliding wind scenario that includes orbital motion. In the following, we discuss the obtained results for a generic system and for the specific case of LS 5039, as well as the main sources of uncertainty.

5.1. General case

In general, a favorable combination of nonradiative and radiative losses, and residence time of the emitting particles, leads to an outer emitting region that is more prominent in its nonthermal energy content and emission than the inner region. Thus, the SEDs are dominated by the outer region for most orbital phases. Moreover, both radio and VHE gamma-ray emission are suppressed close to the star due to free-free and gamma-gamma absorption, respectively, unless small system inclinations $i < 30°$ and/or orbital phases close to the INFC are considered. Nevertheless, the light curves show a nonnegligible or even dominant contribution of the inner region close to the INFC for a broad energy range. This is mainly caused by the inner region emission being more Doppler-boosted than the outer region one, due to the flow moving faster in the former. Higher values of $v_{\rm Cor}$ (which could indicate a lower degree of mixing of stellar and pulsar winds) tend to decrease the radiative output of the outer region due to an increase in the adiabatic losses and in the escape rate of particles from the relevant emitting region. This trend is only broken for orbital phases close to the INFC, where a higher Doppler boosting is able to compensate for the decrease of intrinsic emission in the outer region. Doppler boosting (and hence the adopted velocity profile) has also a high influence on the orbital modulation of the IC radiation in both the inner and outer regions, to the point that emission peaks can become valleys owing to a change in the fluid speed of a factor of ∼3 in the outer region[2].

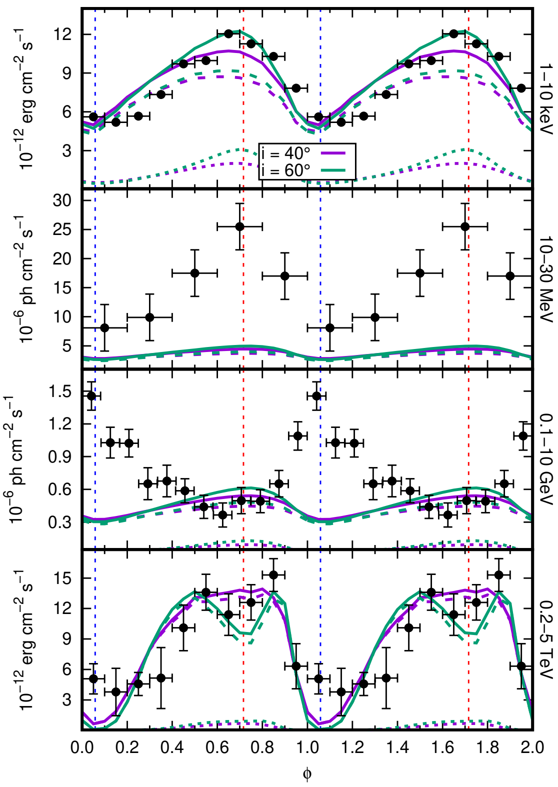

Fig. 11. *From top to bottom*: light curves of LS 5039 in the *Suzaku* (1–10 keV), COMPTEL (10–30 MeV), *Fermi*/LAT (0.1–10 GeV), and H.E.S.S. (0.2–5 TeV) energy ranges, for $i = 40°$ (purple lines) and 60° (green lines). The contributions of the inner and outer regions are shown with dotted and dashed lines, respectively. The phases corresponding to the INFC (SUPC) are shown with red (blue) vertical dashed lines. Flux units are not the same for all the plots.

Radio emission could be used to track part of the spiral trajectory of the shocked flow for strong enough magnetic fields with $\eta_B \gtrsim 0.1$, while no evidence of such spiral structure is predicted for low fields. In any case, as long as the overall radio emission is detectable, variations of the image centroid position on the order of 1 mas (for a distance to the source of ∼3 kpc) could be used as an indication of the dependency of the emitter structure with the orbital phase. This behavior is not exclusive

---

[2] A similar effect is expected to happen if different velocity profiles are assumed for the inner region, but this has not been explicitly explored in this work.

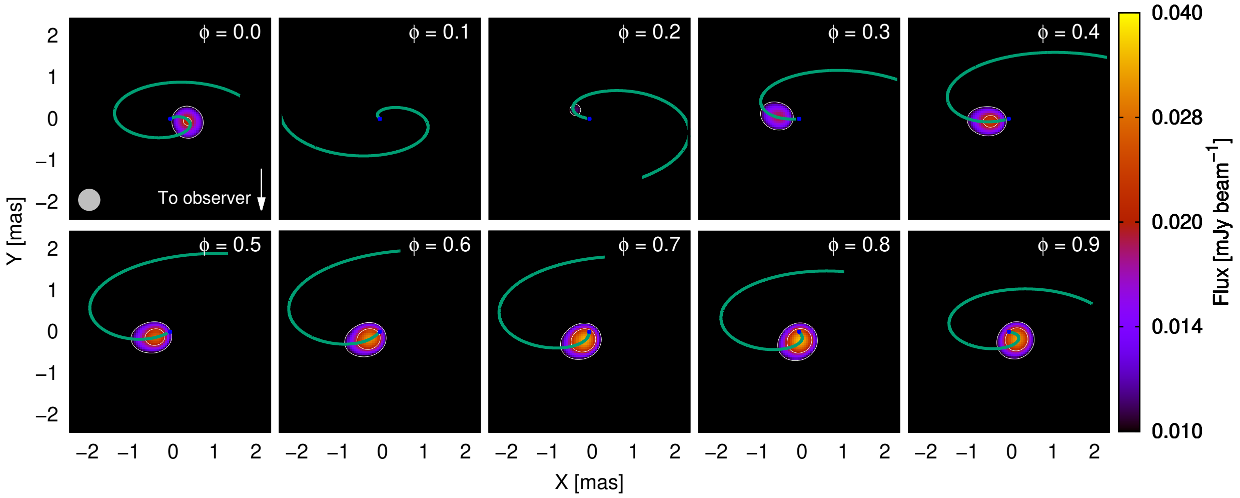

Fig. 12. Same as in Fig. 9, but for the LS 5039 model parameters, with $i = 60°$. Note the change in the color scale.

of a colliding wind scenario, however, since the jets in a microquasar scenario could be affected by orbital motion in a similar manner (e.g., Bosch-Ramon 2013; Molina & Bosch-Ramon 2018; Molina et al. 2019).

There are some limitations in our model that should be acknowledged. One of them is the simplified dynamical treatment of the emitter, considered as a 1D structure. Not using proper hydrodynamical simulations makes the computed trajectory approximately valid within the first spiral turn, after which strong instabilities would significantly affect the fluid propagation, as seen in Bosch-Ramon et al. (2015). Nonetheless, since most of the emission comes from the regions close to the binary system, we do not expect strong variations in the radiative output due to this issue. We are not considering particle reacceleration beyond the Coriolis shock, although additional shocks and turbulence are expected to develop under the conditions present farther downstream (Bosch-Ramon et al. 2015), and these processes could contribute to increase the nonthermal particle energetics. Accounting for reacceleration would in turn increase the emission farther from the binary system, resulting for instance in more extended radio structures, although with the aforementioned inaccuracies in the trajectory computation gaining more importance.

Finally, we note that the model results for a generic case could change significantly for different values of some parameters that are difficult to determine accurately. The fluid speed and detailed geometry in the inner and outer regions are hard to constrain observationally. Precise values of the magnetic field, the electron injection index, the acceleration efficiency, and the nonthermal luminosity fraction are also difficult to obtain due to the presence of some degeneracy among them. Any significant changes in these quantities with respect to the values adopted in this work could have a strong influence on the emission outputs of the system.

5.2. LS 5039

Several model parameters can be fixed for the study of LS 5039 thanks to the existing observations of the source. Those parameters that cannot be obtained from observations are determined by heuristically (although quite thoroughly) exploring the parameter space, trying to better reproduce the observed LS 5039 emission. For this purpose, a hard particle spectrum is injected at both accelerators, with a power-law index $p = -1.3$, and a very high acceleration efficiency of $\eta_{\rm acc} = 0.8$ is assumed in both locations (we note that values between 0.5 and 1 give qualitatively similar results). These values are higher than those used for the general case, already quite extreme, although they cannot be discarded given the current lack of knowledge on the acceleration processes taking place in LS 5039 (or even the emitting process; see, e.g., Khangulyan et al. 2020, for an alternative origin of the gamma rays in which a synchrotron-related mechanism does play a role). Additionally, since the outer region behavior reproduces better the observed (X-ray and VHE) light curves, a higher $\eta_{\rm NT}$ is assumed for the Coriolis shock than for the CD apex, providing the former with a larger nonthermal luminosity budget (i.e., $\eta_{\rm NT} = 0.18$ versus 0.03).

The model nicely reproduces the observed X-ray and VHE gamma-ray emission of LS 5039, as well as the HE gamma-ray flux, although it fails to properly account for the HE gamma-ray modulation due to the synchrotron dominance in this energy range. A possible solution to this issue could be the inclusion of particle reacceleration beyond the Coriolis shock, which combined with the lower magnetic field may result in enough IC emission to explain the observed modulation of the HE gamma rays. This would also alleviate the extreme value of $\eta_{\rm acc}$ needed for the synchrotron emission to reach GeV energies. The largest difference between the model predictions and the observations comes at photon energies around 10 MeV, where the emission is underestimated by a factor of up to 5 (although interestingly the modulation is as observed). Some MeV flux would be added if we accounted for the synchrotron emission of electron-positron pairs created by gamma rays interacting with stellar photons (e.g., Bosch-Ramon et al. 2008; Cerutti et al. 2010), which is not included in our model. However, this component cannot be much larger than the TeV emission, as otherwise IC from these secondary particles would largely violate the 10 GeV observational flux constraints. Therefore, the energy budget of secondaries alone cannot explain the MeV flux.

The lack of predicted VHE emission around the SUPC is due to strong gamma-gamma absorption. The fact that we use a 1D emitter at the symmetry axis of the conical CD overestimates this absorption, since we are not considering emitting sites at the CD itself, which is approximately at a distance R from the axis (see Fig. 1) or even farther (see the shocked pulsar wind extension in the direction normal to the orbital plane in the corresponding maps in Bosch-Ramon et al. 2015). Within a few orbital separations from the pulsar (where most of the emission comes from), the CD is significantly farther from the star than its axis, and the observer, star, and flow relative positions are also quite different, allowing for lower absorption in some of the emitting regions. Therefore, the use of an extended emitter would reduce gamma-gamma absorption and increase the predicted VHE fluxes around the SUPC, possibly explaining the H.E.S.S. fluxes. Particle reacceleration beyond the Coriolis shock may also make some regions farther away from the star to emit VHE photons that would be less absorbed. As already discussed for the general case, reacceleration would also extend the radio emission and, if accounted for, could allow for a sky map comparison with VLBI observations (e.g., Moldón et al. 2012). Thus, one could constrain a reacceleration region added to our model using VLBI observations, but this is beyond the scope of the present work. It is worth noting that emission from secondary particles could also have a significant contribution to the extended and nonextended VLBI components (Bosch-Ramon & Khangulyan 2011).

Our computed SED is qualitatively different to the best fit scenario presented in del Palacio et al. (2015), in which a one-zone model was applied for an accelerator in a fixed position at a distance of $1.4a \approx 3.3 \times 10^{12}$ cm from the star. Although the general shape is similar, their SED is totally dominated by IC down to $\sim$1 MeV, whereas in our model IC is only relevant at energies $\gtrsim$10 GeV. Another one-zone model in Takahashi et al. (2009) explains well the X-ray and VHE gamma-ray emission and modulation, although it underestimates the fluxes at MeV and GeV energies (which were not available by the time of publication of this work). Our synchrotron and IC phase-averaged SEDs above 100 MeV are somewhat close to those in Zabalza et al. (2013). They applied a two-zone model to LS 5039, with the two emitting regions located at the CD apex and the Coriolis shock. Their model reproduces better the GeV modulation, although it also fails to explain the MeV emission, and underestimates the X-ray emission by more than one order of magnitude. Similar results were obtained by Dubus et al. (2015) with a model that computes the flow evolution through a 3D hydrodynamical simulation of the shocked wind close to the binary system, where orbital motion is still unimportant (and thus, it does not include the Coriolis shock). Modulation in the HE band is well explained there, although both the X-ray and the MeV emission are underestimated. All of the above, added to the fact that the 1D emitter model presented in this work also fails to reproduce some of the LS 5039 features, seems to point toward the need of more complex models to describe the behavior of this source, accounting for particle reacceleration, using data from 3D (magneto-)hydrodynamical simulations to compute the evolution of an emitter affected by orbital motion, and possibly including the unshocked pulsar wind zone to correctly describe the MeV radiation (see, e.g., Derishev et al. 2012).

Acknowledgements. We would like to thank the referee for his/her constructive and useful comments, which were helpful to improve the manuscript. We acknowledge support by the Spanish Ministerio de Economía y Competitividad (MINECO/FEDER, UE) under grant AYA2016-76012-C3-1-P, with partial support by the European Regional Development Fund (ERDF/FEDER), and from the Catalan DEC grant 2017 SGR 643. EM acknowledges support from MINECO through grant BES-2016-076342.

References

Abeysekara, A. U., Benbow, W., Bird, R., et al. 2018, ApJ, 867, L19
Aharonian, F., Akhperjanian, A. G., Aye, K. M., et al. 2005, A&A, 442, 1
Aharonian, F., Akhperjanian, A. G., Bazer-Bachi, A. R., et al. 2006, A&A, 460, 743
Aharonian, F. A., Akhperjanian, A. G., Bazer-Bachi, A. R., et al. 2007, A&A, 469, L1
Barkov, M. V., & Bosch-Ramon, V. 2016, MNRAS, 456, L64
Bogovalov, S. V., Khangulyan, D. V., Koldoba, A. V., Ustyugova, G. V., & Aharonian, F. A. 2008, MNRAS, 387, 63
Bosch-Ramon, V. 2013, Eur. Phys. J. Web Conf., 61, 03001
Bosch-Ramon, V., & Barkov, M. V. 2011, A&A, 535, A20
Bosch-Ramon, V., & Khangulyan, D. 2009, Int. J. Mod. Phys. D, 18, 347
Bosch-Ramon, V., & Khangulyan, D. 2011, PASJ, 63, 1023
Bosch-Ramon, V., Motch, C., Ribó, M., et al. 2007, A&A, 473, 545
Bosch-Ramon, V., Khangulyan, D., & Aharonian, F. A. 2008, A&A, 482, 397
Bosch-Ramon, V., Barkov, M. V., Khangulyan, D., & Perucho, M. 2012, A&A, 544, A59
Bosch-Ramon, V., Barkov, M. V., & Perucho, M. 2015, A&A, 577, A89
Casares, J., Ribó, M., Ribas, I., et al. 2005, MNRAS, 364, 899
Cerutti, B., Malzac, J., Dubus, G., & Henri, G. 2010, A&A, 519, A81
Collmar, W., & Zhang, S. 2014, A&A, 565, A38
Corbet, R. H. D., Chomiuk, L., Coe, M. J., et al. 2016, ApJ, 829, 105
Corbet, R. H. D., Chomiuk, L., Coe, M. J., et al. 2019, ApJ, 884, 93
de la Cita, V. M., Bosch-Ramon, V., Paredes-Fortuny, X., Khangulyan, D., & Perucho, M. 2016, A&A, 591, A15
del Palacio, S., Bosch-Ramon, V., & Romero, G. E. 2015, A&A, 575, A112
Derishev, E. V., & Aharonian, F. A. 2012, in American Institute of Physics Conference Series, eds. F. A. Aharonian, W. Hofmann, & F. M. Rieger, Am. Inst. Phys. Conf. Ser., 1505, 402
Dubus, G. 2006, A&A, 456, 801
Dubus, G. 2013, A&ARv., 21, 64
Dubus, G., Lamberts, A., & Fromang, S. 2015, A&A, 581, A27
Dubus, G., Guillard, N., Petrucci, P.-O., & Martin, P. 2017, A&A, 608, A59
Eger, P., Laffon, H., Bordas, P., et al. 2016, MNRAS, 457, 1753
Eichler, D., & Usov, V. 1993, ApJ, 402, 271
Fermi LAT Collaboration (Abdo, A. A., et al.) 2009, ApJ, 706, L56
Fermi LAT Collaboration (Ackermann, M., et al.) 2012, Science, 335, 189
Gaia Collaboration (Brown, A. G. A., et al.) 2018, A&A, 616, A1
Gould, R. J., & Schréder, G. P. 1967, Phys. Rev., 155, 1408
Hadasch, D., Torres, D. F., Tanaka, T., et al. 2012, ApJ, 749, 54
Hess, C., Abramowski, A., et al. 2015, MNRAS, 446, 1163
Hinton, J. A., Skilton, J. L., Funk, S., et al. 2009, ApJ, 690, L101
Khangulyan, D., Hnatic, S., Aharonian, F., & Bogovalov, S. 2007, MNRAS, 380, 320
Khangulyan, D., Aharonian, F. A., & Kelner, S. R. 2014, ApJ, 783, 100
Khangulyan, D., Aharonian, F., Romoli, C., & Taylor, A. 2020, ArXiv e-prints [arXiv:2003.00927]
Leahy, D. A. 2004, A&A, 413, 1019
Luri, X., Brown, A. G. A., Sarro, L. M., et al. 2018, A&A, 616, A9
Maraschi, L., & Treves, A. 1981, MNRAS, 194, 1P
Moldón, J., Ribó, M., & Paredes, J. M. 2012, A&A, 548, A103
Molina, E., & Bosch-Ramon, V. 2018, A&A, 618, A146
Molina, E., del Palacio, S., & Bosch-Ramon, V. 2019, A&A, 629, A129
Muijres, L. E., de Koter, A., Vink, J. S., et al. 2011, A&A, 526, A32
Muijres, L. E., Vink, J. S., de Koter, A., Müller, P. E., & Langer, N. 2012, A&A, 537, A37
Pacholczyk, A. G. 1970, Radio Astrophysics. Nonthermal Processes in Galactic and Extragalactic Sources (W. H. Freeman & Company)
Paredes, J. M., & Bordas, P. 2019, ArXiv e-prints [arXiv:1901.03624]
Paredes, J. M., Martí, J., Ribó, M., & Massi, M. 2000, Science, 288, 2340
Pauldrach, A., Puls, J., & Kudritzki, R. P. 1986, A&A, 164, 86
Rybicki, G. B., & Lightman, A. P. 1986, Radiative Processes in Astrophysics (Wiley-VCH)
Sarty, G. E., Szalai, T., Kiss, L. L., et al. 2011, MNRAS, 411, 1293
Sierpowska-Bartosik, A., & Torres, D. F. 2007, ApJ, 671, L145
Szostek, A., & Dubus, G. 2011, MNRAS, 411, 193
Takahashi, T., Kishishita, T., Uchiyama, Y., et al. 2009, ApJ, 697, 592
Takata, J., Leung, G. C. K., Tam, P. H. T., et al. 2014, ApJ, 790, 18
Tavani, M., Kniffen, D., Mattox, J. R., Paredes, J. M., & Foster, R. S. 1998, ApJ, 497, L89
Zabalza, V., Bosch-Ramon, V., & Paredes, J. M. 2011, ApJ, 743, 7
Zabalza, V., Bosch-Ramon, V., Aharonian, F., & Khangulyan, D. 2013, A&A, 551, A17
Zanin, R., Fernández-Barral, A., de Oña Wilhelmi, E., et al. 2016, A&A, 596, A55
Zdziarski, A. A., Malyshev, D., Dubus, G., et al. 2018, MNRAS, 479, 4399

Part II

BINARY SYSTEMS WITH THE MAGIC TELESCOPES

5

MULTIWAVELENGTH OBSERVATION OF MAXI J1820+070

The work presented in this chapter corresponds to a paper in preparation for submission to the Monthly Notices of the Royal Astronomical Society. This paper includes data from the MAGIC, H.E.S.S. and VERITAS collaborations, the latter two not shown here due to privacy policies.

5.1 INTRODUCTION

X-ray binaries are systems consisting of a non-degenerate star and a compact object – either a BH or a NS – that accretes matter from the companion star. In low-mass X-ray binaries, the companion mass is below $\sim 1\ M_{\odot}$, and accretion on to the compact object normally takes place via the Roche lobe overflow mechanism (e.g. Remillard and McClintock 2006). Typically, low-mass X-ray binaries with a BH (BH-LMXBs) also feature transient jets launched from the latter, which are powered by the accretion process, the magnetic field or the BH rotation, or a combination of them (see Romero et al. 2017, and references therein). These jets can efficiently accelerate charged particles to very high energies, and emit non-thermal radiation from radio to gamma rays as a result of the radiative cooling of the accelerated particles (see e.g., Mirabel and Rodríguez 1999; Fender and Muñoz-Darias 2016, for a review on jets in X-ray binaries).

Most of the time, BH-LMXBs are in a quiescent state and remain undetected until they undergo periodic outbursts that may last for several months, and during which their luminosity increases by several orders of magnitude. A BH-LMXB can be mainly classified into either a soft state (SS) or a hard state (HS) based on the hardness of its X-ray spectrum during one of these outbursts. At the beginning of the outburst, a BH-LMXB is typically in the HS, in which the X-rays exhibit a hard-spectrum component. This emission is likely originated in a hot corona around the BH, where IC scattering of low-energy photons coming from the accretion disk takes place. The HS also features jet synchrotron emission, which is mostly seen at radio and infrared wavelengths, although it may also be responsible for a significant contribution to the X-ray output of the system (e.g. Fender and Muñoz-Darias 2016). Eventually, as the outburst goes on, the source will transition to the SS. In this state, most of the X-rays are of thermal origin, emitted by the hot inner regions of the accretion disk. Also, radio emission fades away, indicating a lack of jet activity (although weak jets may still be present and remain undetected). In a typical outburst, a BH-LMXB normally completes the HS–SS–HS cycle, going through short-lived intermediate states during the HS–SS and SS–HS transitions (see Fender and Belloni 2012, and references therein for a more detailed description of the states of BH-LMXBs). High-energy (HE, above 100 MeV) and very high-energy (VHE, above 100 GeV) gamma rays are not typically detected coming from BH-LMXBs (Ahnen et al. 2017; H. E. S. S. Collaboration et al. 2018), with the main exception of the $\sim 4\sigma$ detection at HE of V404 Cygni during an outburst in 2015 (Loh et al. 2016; Piano et al. 2017). On the other hand, HE emission is detected from high-mass systems like Cygnus X-1 and Cygnus X-3, with likely jet origin in both cases (see Zanin et al. 2016; Fermi LAT Collaboration et al. 2009; Tavani et al. 2009a; Zdziarski et al. 2018). Nevertheless, the VHE detection of high-mass X-ray binaries remains also elusive (Aleksić et al. 2010, 2015; MAGIC Collaboration et al. 2017, 2018), with the possible exception of SS433, for which the HAWC Collaboration claimed a detection of ~ 20 TeV photons originating in a region very far from the binary system (where the jets interact with the supernova remnant around the source; Abeysekara et al. 2018), and perhaps Cygnus X-1, which was detected at a $\sim 4\sigma$ level on a single night by MAGIC (Albert et al. 2007). Increasing the number of X-ray binaries detected in HE and VHE gamma rays would enable a better physical characterization of these systems in terms of their magnetic field, particle acceleration mechanisms and maximum particle energy, or gamma-ray absorption processes, among others.

MAXI J1820+070 (RA = $18^{\mathrm{h}}20^{\mathrm{m}}21^{\mathrm{s}}.9$, Dec = $+07^{\circ}11'07''$) is a BH-LMXB that was first discovered in the optical band on 2018 March 6 (MJD 58183.6) by the All-Sky Automated Survey for Supernovae (ASAS-SN; Tucker et al. 2018), and on March 11 (MJD 58188.8) it was also detected in X-rays by the Monitor of All-sky X-ray Image (MAXI; Kawamuro et al. 2018). Soon after its discovery, MAXI J1820+070 showed an exceptionally high X-ray flux peaking at ~ 4 times that of the Crab Nebula (e.g., Del Santo and Segreto 2018; Shidatsu et al. 2019). A distance to the source of 2.96 ± 0.33 kpc was determined from radio parallax (Atri et al. 2020), which is consistent with previous measurements from *Gaia* DR2 data (Gandhi et al. 2019). The estimates for the jet speed and inclination during transient ejections in the HS–SS transition are, respectively, $0.89c \pm 0.09c$ and $63^{\circ} \pm 3^{\circ}$ (Atri et al. 2020). Assuming the latter value as the binary inclination, the BH and stellar masses were constrained from optical spectroscopy measurements to $8.48^{+0.79}_{-0.72} M_{\odot}$ and $0.61^{+0.13}_{-0.12} M_{\odot}$, respectively (Torres et al. 2020). Spectroscopic measurements set the orbital period of MAXI J1820+070 to 16.4518 ± 0.0002 h (Torres et al. 2019). The parameters above yield an orbital semi-major axis of 5×10^{11} cm.

MAXI J1820+070 remained in the HS from the beginning of the outburst in March until early July (2018), when it began its transi-

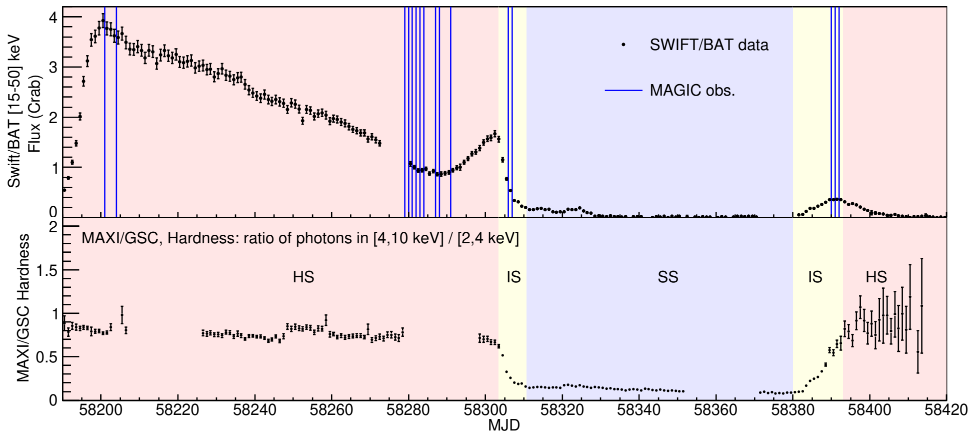

Figure 5.1: *Top panel*: *Swift*/BAT LC of MAXI J1820+070 during the 2018 outburst. Vertical lines show the dates when MAGIC observations were done. *Bottom panel*: Evolution of the MAXI J1820+070 hardness ratio of the 4–10 to 2–4 keV fluxes as seen by MAXI/GSC. The source states are superimposed as red (HS), blue (SS) and yellow (HS–SS and SS–HS) background colors. Plot provided by Jean-Pierre Ernenwein.

tion to the SS. This source state lasted until late September, when MAXI J1820+070 started transitioning back to the HS shortly before becoming quiescent and putting an end to the outburst, which lasted a total of $\sim$ 7 months. During its outburst, MAXI J1820+070 was observed with a wide variety of instruments at radio (e.g., Atri et al. 2020; Bright et al. 2020), near infrared (e.g. Sánchez-Sierras and Muñoz-Darias 2020), optical (e.g., Veledina et al. 2019; Torres et al. 2019; Shidatsu et al. 2019), and X-ray (e.g., Roques and Jourdain 2019; Shidatsu et al. 2019; Buisson et al. 2019; Fabian et al. 2020; Chakraborty et al. 2020; Zdziarski et al. 2021) frequencies. Making use of the results in Shidatsu et al. 2019 to define the exact dates of the beginning and end of each source state, the HS is set in MJD 58189.0 – 58303.5 and MJD 58393.0 – 58420.0, the HS–SS transition in MJD 58303.5 – 58310.7, the SS in MJD 58310.7 – 58380.0, and the SS–HS transition in MJD 58380.0 – 58393.0. The evolution of the X-ray state of MAXI J1820+070 can be seen in Fig. 5.1, which shows its X-ray LC in the 15–50 keV range, and its hardness ratio (i.e., the flux ratio of high-energy to low-energy X-rays) from *Swift*/BAT and MAXI/GSC data.

We present the results of observations at VHE gamma rays from MAXI J1820+070 with the MAGIC telescopes. In order to give a more complete picture of the source, we also include *Fermi*-LAT data of HE gamma rays, as well as multiwavelength observations from radio to X-rays. This chapter is structured as follows: Section 5.2 describes the observations and data analysis for each telescope. Section 5.3 presents

Table 5.1: Summary of the observations of MAXI J1820+070 by the MAGIC telescopes. The effective observation time, the zenith angle range and its median are shown for each source state.

Source state	Time [h]	Zenith angle (median) [deg]
Hard State	14.2	21 – 58 (34)
HS → SS	4.9	21 – 48 (27)
SS → HS	3.4	28 – 56 (41)
TOTAL	22.5	21 – 58 (32)

the results of this work, for which a discussion is given in Section 5.4. Finally, we conclude with a summary in Section 5.5.

5.2 OBSERVATIONS AND DATA ANALYSIS

5.2.1 *MAGIC data*

MAXI J1820+070 was observed during its 2018 outburst by the MAGIC IACT array (Aleksić et al. 2016a), which is a stereoscopic system of two telescopes located at the Roque de los Muchachos Observatory in La Palma, Spain (29°N, 18°W, 2200 m above sea level). The telescopes are equipped with mirror dishes with a diameter of 17-m, and fast photo-multiplier tube cameras with a 3.5° field of view. The MAGIC observations were performed from March to October 2018, covering the initial HS of the source as well as the state transitions. After data quality cuts a total of 22.5 h of observations remain. We divided our data sample according to the X-ray state (or transition) of the source as defined in Sect. 5.1. The top panel of Fig. 5.1 shows the specific days in which MAGIC observations were performed. A summary breakdown of these observations, including their zenith angle, is shown in Table 5.1.

The low-level analysis of MAGIC data was performed using the standard procedure (see Aleksić et al. 2016b). No significant signal was detected from the data set regardless of the energy binning considered, neither by analyzing all the data together, or by separating them by source state or in daily bins. In all cases, the detection significance was below 2.5σ. The gamma-ray upper limits upper limits (ULs) at different energy bins were computed following a maximum-likelihood ratio test as described in the Appendix of this chapter. A confidence level (C.L.) of 95% was used, and a global systematic uncertainty of 30% was taken, which accounts for the systematic error in both the flux normalization and the energy scale. For the UL computation, the source VHE gamma-ray spectrum was assumed to follow a power law with spectral index $\alpha = 2.5$, i.e. $\mathrm{d}N/\mathrm{d}\varepsilon \propto \varepsilon^{-\alpha}$.

5.2.2 *Fermi*-LAT data

Fermi-LAT[1] data selected for the analysis presented in this paper cover the period MJD 58189 – 58420. The data were analyzed with the latest available `fermitools` v. 2.0.8 with P8R3_V3 response functions (`SOURCE` photon class)[2].

We performed a standard binned likelihood analysis of a 14°-radius region around the MAXI J1820+070 position. The analysis is based on the fitting of a spatial and spectral model of the sky region around the source of interest to the data. The model of the region included all sources from the 4FGL DR2 catalog (Abdollahi et al. 2020) as well as components for isotropic and galactic diffuse emissions given by the standard spatial and spectral templates `iso_P8R3_CLEAN_V2_v1.txt` and `gll_iem_v07.fits`.

The spectral template for each 4FGL source in the region was selected according to the catalog model. MAXI J1820+070 was modeled as a point-like source with a power-law spectrum. Following the recommendation of the *Fermi*-LAT collaboration, our analysis is performed with energy dispersion handling enabled. The flux upper limits were calculated at a 95% C.L. with the help of the `IntegralUpperLimit` module for a power-law slope fixed to $\alpha = 2.5$, as for the VHE data analysis.

5.2.3 *Additional multiwavelength data*

We use data from several radio telescopes at different frequencies taken from Bright et al. 2020. Optical data are taken from Celma 2019, in which observations performed with the Joan Oró Telescope (TJO; Colomé et al. 2010) and *Swift*/UVOT are reported. The optical fluxes are already corrected from interstellar extinction using a hydrogen column density of $N_{\mathrm{H}} = 1.12 \times 10^{21}$ cm^{-2} and $N_{\mathrm{H}}/A_V = 2.87 \times 10^{21}$ cm^{-2} mag^{-1}, being A_V the extinction in the V band. This yields an interstellar extinction going from 0.2 to 0.6 mag, the limits corresponding to the I and U bands, respectively (see Celma 2019, and references therein). We also include public LCs from MAXI/GSC[3] and *Swift*/BAT[4].

For the SEDs of MAXI J1820+070, INTEGRAL (Winkler et al. 2003) data are added to that of the previously mentioned instruments, based on results by Roques and Jourdain 2019 from MJD 58206 to 58246, during the first half of the HS. NICER[5] (Gendreau et al. 2012) data are also used, and were retrieved through the HEASARC database as pre-processed event files. Re-processing and filtering are done with

---

[1] *Fermi*-LAT analysis by Denys Malyshev

[2] See description of *Fermi*-LAT response functions.

[3] `http://maxi.riken.jp/star_data/J1820+071/J1820+071.html`

[4] `https://swift.gsfc.nasa.gov/results/transients/weak/MAXIJ1820p070`

[5] NICER analysis by Sebastien Le Stum

Table 5.2: Integral flux upper limits at different source states, computed above 100 MeV from *Fermi*-LAT data, and above 200 GeV from MAGIC data. For the SS–HS transition, the UL above 300 GeV is shown instead.

Source state	UL ($\varepsilon > 100$ MeV) [ph cm^{-2} s^{-1}]	UL ($\varepsilon > 200/300$ GeV) [ph cm^{-2} s^{-1}]
Hard State	3.5×10^{-8}	3.8×10^{-12}
HS → SS	1.5×10^{-7}	3.0×10^{-12}
Soft State	2.7×10^{-8}	–
SS → HS	5.0×10^{-8}	3.2×10^{-12}
Hard State	6.6×10^{-8}	–
TOTAL	2.1×10^{-8}	2.2×10^{-12}

NICERDAS software available in the HEAsoft distribution (v6.26) using standard criteria. The data shown in this thesis are not deabsorbed from interstellar absorption. Spectra were extracted using the *extractor* function from the ftools package. Error bars are $\pm 1\sigma$ Poisson uncertainty. Energy and gain calibrations were performed using the HEASARC Calibration Database version XTI (20200722). To avoid telemetry saturation, the fraction of active modules had to be adjusted. This was taken into account considering that each module contributes equally to the effective area. NICER observed for 109 h, 21.8 h and 4.56 h during the HS, the HS–SS transition and SS–HS transition, respectively.

5.3 RESULTS

The observations of MAXI J1820+070 reported in this work do not show any significant emission in either HE or VHE gamma rays, regardless of the source state. The computed integral flux ULs for *Fermi*-LAT and MAGIC data are shown in Table 5.2 for each X-ray state. The former are calculated for photon energies $\varepsilon > 100$ MeV, whereas the latter are computed at $\varepsilon > 200$ GeV for the HS, the HS–SS transition and the whole sample, and at $\varepsilon > 300$ GeV for the SS–HS transition. The increase in energy threshold of the last data set is due to a higher average zenith angle of the observations, which does not allow electromagnetic showers triggered by lower energy gamma rays to be detected.

Fig. 5.2 represents the ULs on the VHE differential flux obtained for 5 different energy bins and each source state for which observations were performed. For the SS–HS transition, the lowest energy bin is not computed due to the increased energy threshold of the corresponding observations.

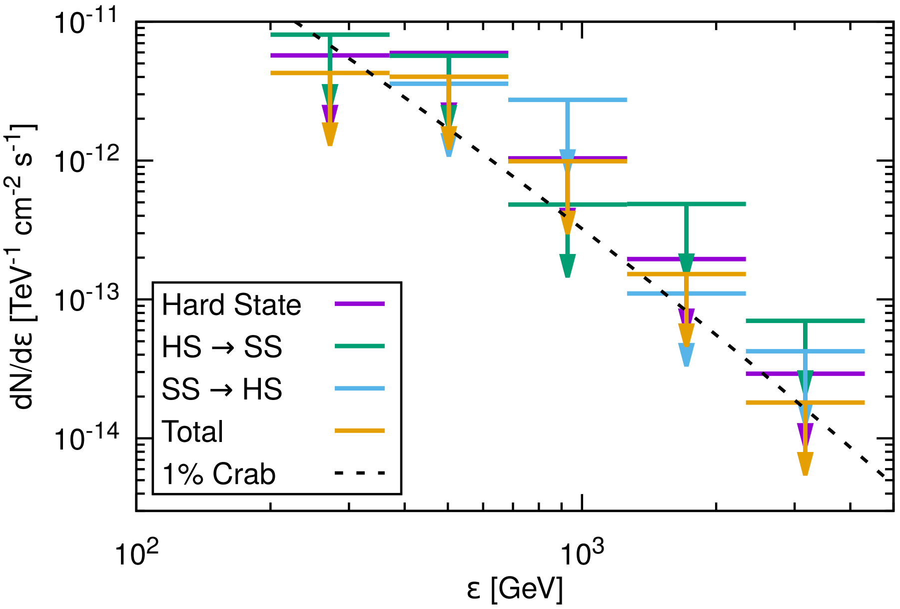

Figure 5.2: Differential flux upper limits of MAXI J1820+070 obtained from MAGIC data for different energy ranges and source states. The dashed black line shows 1% of the differential spectrum of the Crab Nebula.

Fig. 5.3 shows the LCs of MAXI J1820+070 at different frequencies, with the gamma-ray LC corresponding to the ULs in Table 5.2. The radio fluxes in the top panel include both the core emission from the jet regions close to the binary system, and the radiation emitted by discrete ejections launched during the HS–SS transition. Core emission is dominant during the source HS, while the ejections dominate throughout the SS, during which no core emission is detected (see Bright et al. 2020, for the details). Optical fluxes in the second panel are obtained from a total set of 16457 images taken in the 5 Johnson-Cousins filters (with central wavelengths around 366, 435, 548, 635 and 880 nm, respectively from the *U* to *I* filters), and distributed over 113 different nights between March and November 2018. The X-ray LCs in the third panel are obtained from the daily integral fluxes of MAXI J1820+070 from MAXI/GSC (for 2 keV $\leq \varepsilon \leq$ 20 keV) and *Swift*-BAT (for 15 keV $\leq \varepsilon \leq$ 50 keV). The gaps represent the periods when the source was not observed with these instruments.

The SEDs of MAXI J1820+070, averaged for those source states in which VHE data are available, are shown in Fig. 5.4. We note that the jump between NICER and INTEGRAL data in the top panel is just an effect of the different time coverage of the observations. While NICER data are averaged over the whole duration of the HS, INTEGRAL data only cover roughly the first half of it (see Sect. 5.2.3), when the average X-ray flux was higher.

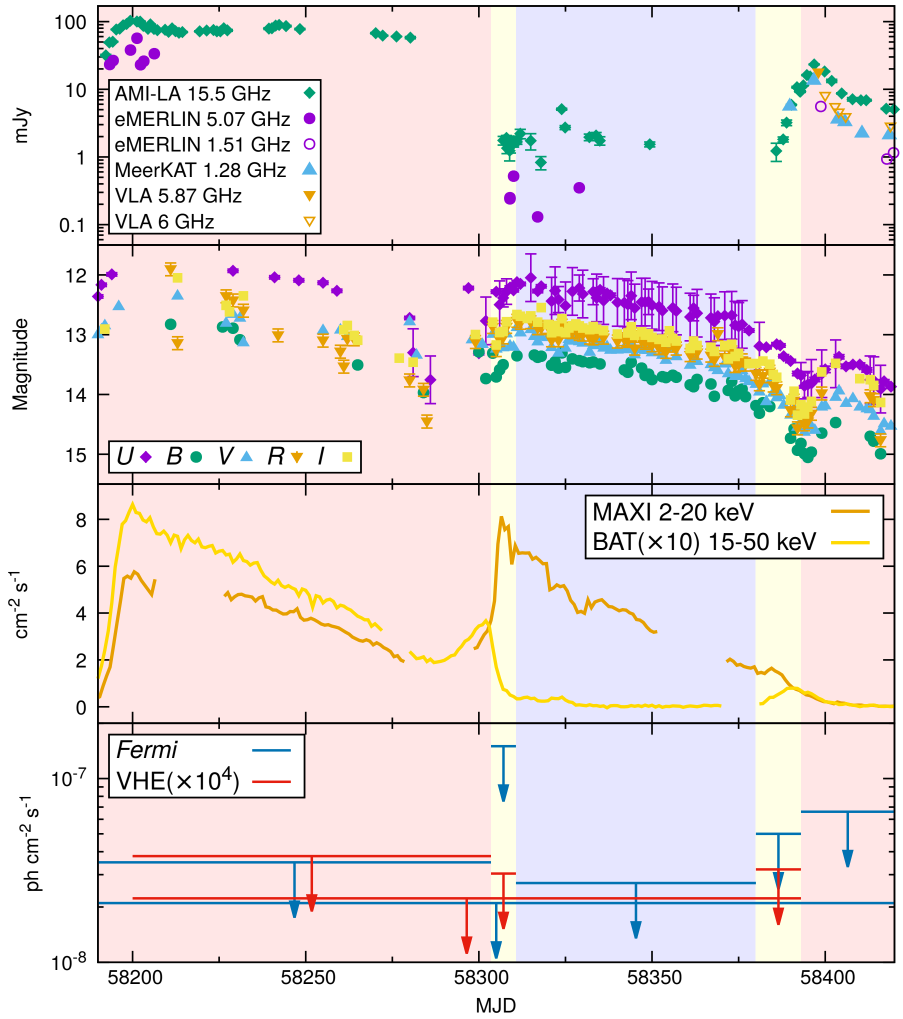

Figure 5.3: From *top* to *bottom*: Radio, optical, X-ray, and gamma-ray light curves of MAXI J1820+070 during its 2018 outburst (MJD 58189.0 – 58420.0). The shaded areas correspond to the HS (red), the HS–SS and SS–HS transitions (yellow) and the SS (blue). The units of the third panel are [ph cm^{-2} s^{-1}] for MAXI/GSC, and [counts cm^{-2} s^{-1}] for *Swift*/BAT. The latter fluxes are multiplied by 10 for a better visualization. The bottom panel shows *Fermi*-LAT ULs above 100 MeV (purple lines), and MAGIC ULs (green lines, multiplied by 10^4) for each source state and transition for which data are available, as well as for the whole outburst. The VHE ULs are computed above 200 GeV except for the SS–HS transition (MJD 58380.0 – 58393.0) for which 300 GeV ULs are shown.

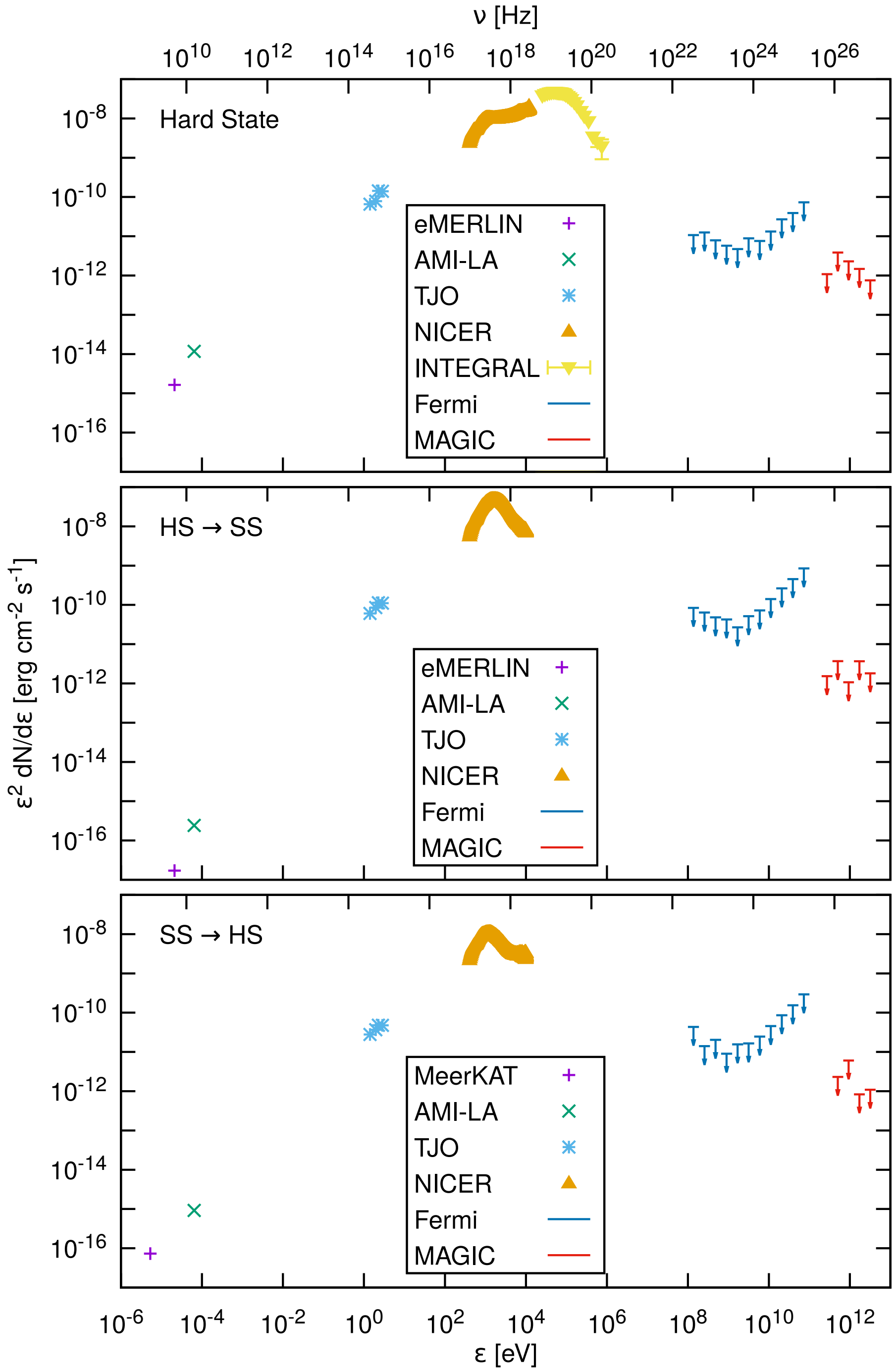

Figure 5.4: From *top* to *bottom*: Spectral energy distributions of MAXI J1820+070 averaged over the HS, the HS–SS transition, and the SS–HS transition. Optical fluxes are corrected from interstellar absorption, whereas NICER ones are not. Note the use of MeerKAT data instead of eMERLIN ones in the bottom plot.

5.4 DISCUSSION

In this section, we start with a short description of the multiwavelength behavior of MAXI J1820+070 based on the data from radio to X-rays. Together with these data, the computation of HE and VHE gamma-ray flux ULs performed in this work, allows us to constrain the size and distance to the BH of any putative region able to produce HE or VHE gamma rays (from now on the potential gamma-ray emitter). This is done through a number of analytical estimates, as well as some reasonable assumptions regarding the magnetic field strength and the distribution (energy dependence and maximum energy) of the non-thermal particles.

Radio emission from MAXI J1820+070 is evidence for jet activity during the whole 2018 outburst. This emission is dominated by a steady jet in the HS, discrete blobs in the HS–SS transition (the emission of which is also dominant throughout the SS as the blobs move away from the binary system), and a jet rebrightening during the SS–HS transition (Bright et al. 2020). Without accounting for blob emission during the SS, which is causally disconnected from the accretion disk, the radio and hard X-ray fluxes have similar behaviors: they decrease slowly through the HS, have a steep decrease in the HS–SS transition, are practically undetectable during the SS, and increase again in the SS–HS transition. This is in accordance with the standard picture of BH-LMXBs, in which steady radio jets in the HS coexist with a hard X-ray emitting corona (sometimes considered to be the base of the jet; Markoff et al. 2001) both of them disappearing in the SS. During the HS, jet synchrotron emission is likely the dominant contribution to the SED up to infrared frequencies, beyond which the spectrum becomes dominated by disk and coronal emission (Rodi et al. 2021; Tetarenko et al. 2021).

Regarding the contribution from the star to the overall SED, MAXI J1820+070 had a magnitude of 17.4 in the G filter (with a central frequency around 460 nm) before the outburst, which is at least 3 magnitudes above the observed optical magnitude during the flare (the latter corresponding to a flux about 15 times larger than before the outburst). These 17.4 magnitudes in G can therefore be taken as an upper limit for the intrinsic emission of the star. In addition, the small solid angle of the star as seen by the BH, assuming a stellar radius equal to that of the Roche lobe, i.e. $\sim 10^{11}$ cm, means that the luminosity of the reprocessed X-rays in the stellar surface should be relatively small. All this implies that the optical and ultraviolet contribution from the star during the outburst should be negligible, and we can safely assume that the observed optical fluxes are dominated by thermal emission from the outer regions of the accretion disk (we recall that the jet is also not dominant at these frequencies).

The estimates performed in the following paragraphs make use of the observations for the HS, but similar arguments can be used for the state transitions as well, for which results are given at the end of this section. The particles responsible for the non-thermal emission are assumed to be only electrons (and positrons), and the hadronic contribution is neglected. Additionally, the derived jet inclination and speed in MAXI J1820+070 make the counter-jet emission much more deboosted than the jet one. We therefore focus the discussion on the jet emission and neglect the counter-jet contribution. Additionally, we use primed quantities for those given in the reference frame moving with the jet flow, while unprimed ones refer to the laboratory frame.

The spectral shape derived from the two radio points at 5.07 and 15.5 GHz in Fig. 5.4 is of the form $\varepsilon\, \mathrm{d}N/\mathrm{d}\varepsilon \propto \varepsilon^{0.75}$, which indicates a highly self-absorbed synchrotron emission at those frequencies. This points towards a transition frequency from an optically thick to an optically thin synchrotron emission at least a few times larger than 15.5 GHz. We assume this frequency (as seen by the observer) to be $\nu_0 = 100$ GHz, with a corresponding extrapolated spectral flux density of $F_0 = 300$ mJy (we note that Rodi et al. 2021 find a higher transition frequency of 10^4 GHz, although this is based on single-day observations instead of the average over the whole HS, as in this work). Since observations at 100 GHz are not available, we assume that the non-thermal electrons reach the energies required for such emission (~ 100 MeV, see below). The values in the jet frame of $\nu_0' = \nu_0/\delta$ and $F_0' = F_0\, \delta^2/\Gamma$ can be used to constrain the magnetic field B' and size R of the radio emitting region (unprimed as the line of sight is almost perpendicular to the jet) through the following relation in cgs units (in which the distance to the source is implicit; Bosch-Ramon 2009; Pacholczyk 1970):

$$\nu_0' \approx 1.6 F_0'^{2/5} B'^{1/5} R^{-4/5} \, . \tag{5.1}$$

The magnetic field is parametrized through the fraction η of magnetic to non-thermal energy density:

$$\frac{B'^2}{8\pi} = \eta \frac{E'_{\rm NT}}{V'} \, , \tag{5.2}$$

where $V' \approx 4\pi R^3 \Gamma/3$ is the proper volume of the emitting region, and $E'_{\rm NT}$ is the energy budget of the non-thermal electrons. We note that this is an approximate approach with a spherical emitter geometry, and that the actual shape could be different (in particular a cylindrical or conical jet-like emitter). Taking an electron distribution $N'(E') = QE'^{-p}$ with $p = 2$ between $E'_{\rm min} \sim 50$ MeV and $E'_{\rm max} \sim$ GeV yields

$$E'_{\rm NT} \approx Q \ln(E'_{\rm max}/E'_{\rm min}) \sim 3Q \, , \tag{5.3}$$

with Q being a normalization constant. We note that p, $E'_{\rm min}$ and $E'_{\rm max}$ are not strongly constrained by the observations, but using typical values of $p \sim 2$, makes Eq. (5.3) not very sensitive to the exact values of $E'_{\rm min}$ and $E'_{\rm max}$. In any case, the chosen values of $E'_{\rm min}$ and $E'_{\rm max}$ are enough to explain the observed (and extrapolated to ν_0) radio emission. We can relate the synchrotron spectral luminosity with the particle distribution with the so-called synchrotron delta-function approximation:

$$L'_{\varepsilon'} \approx N'(E')|\dot{E}'_{\rm syn}|\frac{{\rm d}E'}{{\rm d}\varepsilon'}\ , \tag{5.4}$$

where $\dot{E}'_{\rm syn} = -1.6 \times 10^{-3} B'^2 E'^2$ erg s^{-1} is the synchrotron energy-loss rate of electrons with characteristic energies of $E' = 10^4\,\varepsilon'^{1/2} B'^{-1/2}$ erg, in cgs units (e.g., Pacholczyk 1970).

Taking an equipartition magnetic field with $\eta = 1$ (approximately corresponding to the minimum energy requirement for synchrotron radiation; e.g., Longair 1981), Eqs. (5.1) to (5.4) provide a radio emitter size of $R \approx 2.4 \times 10^{12}$ cm, a non-thermal energy budget of $E'_{\rm NT} \approx 5.6 \times 10^{38}$ erg, and a magnetic field of $B' \approx 10$ G. The latter is consistent with the best-fit value obtained by Rodi et al. 2021, taking into account the dependence of B' with distance used in their model. With this value of B', the electrons responsible for emitting synchrotron photons at ν_0 are those with average energy $E = \Gamma E' \approx 125$ MeV.

In order to put constraints on a potential gamma-ray emitter, we assume that gamma rays are produced by IC scattering of photons coming from the accretion disk or the corona by jet electrons. Given the conditions in MAXI J1820+070, the discussion can be done in the context of the Thompson regime, which is approximately valid at the energies adopted (see below), and simplifies very much the estimates derivation. In this regime, IC is more efficient and the energy gain of the scattered photons is proportional to the square of the electrons Lorentz factor γ. We take characteristic energies for HE and VHE gamma rays of 100 MeV and 100 GeV, respectively. We note that the latter energy is taken slightly below the VHE ULs in order for IC to still happen in the Thomson regime, and we assume that at 100 GeV we would have UL at the same level in SED units as those measured at 200 GeV and shown in Fig. 5.4. The HE gamma rays would be the result of the IC scattering of target X-ray photons with typical energies of ~ 1 keV by $E_{\rm HE} \sim 150$ MeV electrons ($\gamma \sim 300$), while VHE emission would come from optical photons with ~ 1 eV scattered by $E_{\rm VHE} \sim 150$ GeV electrons ($\gamma \sim 3 \times 10^5$). These are reference values for which data at the target photon energies are available, although we note that target photons with energies around the chosen ones would also contribute to the IC emission at the characteristic HE and VHE gamma-ray energies.

As long as the assumptions regarding the magnetic field and electron population hold, the same electrons (i.e., those with the same energy $E \sim 100$ MeV) are responsible for the 100 GHz emission via synchrotron, and the 100 MeV emission via IC. This means that we can derive constraints on the potential HE emitter based on the properties derived above for the radio emitter. The IC radiative output at HE as seen by the observer can be estimated from the (extrapolated) synchrotron radio emission at ν_0 as seen by the observer:

$$\varepsilon^2 \frac{\mathrm{d}N}{\mathrm{d}\varepsilon} \approx \nu_0 F_0 \frac{\dot{E}'_{\mathrm{IC}}}{\dot{E}'_{\mathrm{syn}}} \,, \tag{5.5}$$

where $\dot{E}'_{\mathrm{IC}} = -0.039\, u' E'^2$ is the IC energy-loss rate in the Thomson regime. The energy density of the target photon field with luminosity L_{tar} is $u' \approx u/\Gamma^2 = L_{\mathrm{tar}}/4\pi r^2 c \Gamma^2$, where r is the distance from the potential HE emitter to the BH. This expression is valid as long as the target photons reach the jet mainly from behind (Dermer and Schlickeiser 1994), which is likely the case in MAXI J1820+070. Knowing from the *Fermi*-LAT ULs in Fig. 5.4 that the flux in Eq. (5.5) cannot be higher than $\approx 10^{-11}$ erg cm^{-2} s^{-1}, we obtain a constraint for the distance of $r_{\mathrm{HE}} \gtrsim 3 \times 10^{11}$ cm, meaning that potential HE emission must come from jet regions at the edge of or outside the binary system. Actually, this lower limit for distance is larger given that the radio emitter size derived above is already a few times 10^{12} cm. Conversely, r cannot be more than a few times 10^{13} cm, the exact value depending on the jet opening angle, since that would increase the emitter size and the synchrotron radio emission would become optically thin, contradicting the observations. We note that, in this range of distances and for the R and B' derived above, the energy density of the synchrotron soft X-ray photons (emitted as long as the electrons reach ~ 100 GeV) should be comparable to that of the X-rays coming from the corona and/or the disk. Therefore, synchrotron self-Compton must be responsible for a significant fraction of the total HE emission of MAXI J1820+070.

In order to perform estimations on the VHE emission, we assume that electrons are accelerated up to E_{VHE}. This is reasonable given the magnetic field obtained above, since high acceleration efficiencies are not required to reach those energies (we only need $\eta_{\mathrm{acc}} \lesssim 2 \times 10^3$, with $t'_{\mathrm{acc}} = \eta_{\mathrm{acc}} E'/ecB'$ being the acceleration timescale). The electrons with energies around E_{VHE} emit synchrotron photons of ~ 1 keV. At these energies, the SED is dominated by the accretion disk and the corona, so the jet contribution cannot be directly observed. Nonetheless, recalling that synchrotron emission is taken as optically thin above 100 GHz, the ~ 1 keV radiative output can be extrapolated with the additional assumption (also used in the computation of E'_{NT}) that the non-thermal electrons with E_{VHE} have a similar energy budget as those with E_{HE} (i.e., $p \sim 2$). This is consistent with the fact that, for the derived emitter properties and electron energies, non-radiative losses are dominant and therefore p is not modified by them. The same argument used for the IC HE emission can then be used to derive the VHE emission, taking now the energy density corresponding to optical target photons (for the IC cooling rate) and the extrapolated synchrotron flux at

~ 1 keV (for the synchroton cooling rate) Eq. (5.5), and the lowest energy VHE UL in Fig. 5.4. This results in a distance to the BH of the potential VHE emitter of $r_{\mathrm{VHE}} \gtrsim 4.9 \times 10^{12}$ cm. We recall that the derived R from radio observations puts the emitter at most at a few times 10^{13} cm from the BH.

We note that the distances derived above are sufficiently large for the jet gamma-ray emission to be unaffected by gamma-gamma absorption with the external photons from the disk and corona. The distance up to which this process is important can be estimated by imposing $\tau_{\gamma\gamma} \sim \sigma_{\gamma\gamma} n r \gtrsim 1$, where $\tau_{\gamma\gamma}$ is the optical depth, $\sigma_{\gamma\gamma}$ is the maximum cross-section for gamma-gamma absorption (Gould and Schréder 1967), and $n = L_{\mathrm{tar}}/4\pi r^2 c \varepsilon_{\mathrm{tar}}$ is the number density of the absorbing target photons. For the HE (VHE) gamma rays, the characteristic target energy is $\varepsilon_{\mathrm{tar}} \sim 3$ keV (3 eV), and target photons have a luminosity of $L_{\mathrm{tar}} \sim 1.1 \times 10^{37}$ erg s^{-1} ($\sim 1.4 \times 10^{35}$ erg s^{-1}). This makes gamma-gamma absorption relevant for $r \lesssim 10^9$ cm ($\lesssim 1.3 \times 10^{10}$ cm), much smaller than the minimum emitter distances obtained above. Internal gamma-gamma absorption with synchrotron photons can be neglected, since the number density of those photons is small for the derived emitter size.

We recall that all these computations are averages over the whole HS, and that they are done assuming a strong equipartition magnetic field with $\eta = 1$. Decreasing this value results in more constraining emitter distances. For instance, taking $\eta = 0.01$ ($B' \approx 3$ G) yields a radio emitter size $R \approx 1.8 \times 10^{12}$ cm, $r_{\mathrm{HE}} \gtrsim 9 \times 10^{11}$ cm and $r_{\mathrm{VHE}} \gtrsim 1.5 \times 10^{13}$ cm. In addition, the estimations above can also be done for the state transitions by using the corresponding radio and IC target photon fluxes derived from the SEDs. We use for simplicity the same value of ν_0 as for the HS, although this does not need to be the case, and we keep $\eta = 1$. For the HS–SS transition, an emitter size of $R \approx 6.8 \times 10^{11}$ cm is obtained, corresponding to $B' \approx 14$ G and $E'_{\mathrm{NT}} \approx 2.4 \times 10^{37}$ erg. This leads to $r_{\mathrm{HE}} \gtrsim 4.5 \times 10^{10}$ cm and $r_{\mathrm{VHE}} \gtrsim 9.3 \times 10^{11}$ cm. For the SS–HS transition, we obtain $R \approx 3.7 \times 10^{11}$ cm, $B' \approx 17$ G, and $E'_{\mathrm{NT}} \approx 5.3 \times 10^{36}$ erg, resulting in $r_{\mathrm{HE}} \gtrsim 10^{10}$ cm and $r_{\mathrm{VHE}} \gtrsim 1.6 \times 10^{11}$ cm. The smaller estimated radio emitter size and minimum distances to the BH constrain the potential gamma-ray emitter location to be about a factor 5 closer to the binary system in the state transitions than in the HS, although still far enough so that gamma-gamma absorption is unimportant.

5.5 SUMMARY AND CONCLUSIONS

We have performed observations of the exceptionally bright X-ray source MAXI J1820+070 during its 2018 outburst with the MAGIC experiment in VHE gamma rays. A total of 22.5 h of data were taken during the initial HS of the source and the state transitions. *Fermi-*

LAT data in HE gamma rays covering the whole outburst are also analyzed. The source is not detected at HE or VHE regardless of the energy binning considered, neither for the whole data sample or for the individual source states. Integral and differential HE and VHE flux ULs are provided for each source state, as well as for the whole outburst. These gamma-ray ULs are complemented with additional multiwavelength data from radio to X-rays, in order to provide context to the source interpretation. The radio and X-ray flux evolution throughout the outburst show the expected behavior for a typical BH-LMXB, indicating a source following the usual HS–SS–HS cycle.

Radio emission throughout the whole outburst provides evidence for the presence of jets with a population of non-thermal particles (electrons and possibly positrons) emitting via the synchrotron mechanism. Using reasonable and conservative extrapolations for the spectrum of the emitting electrons, the latter should also emit gamma rays through IC scattering of photons coming from the accretion disk and the corona, and synchrotron self-Compton. The non-detection of these gamma rays puts constraints on the emitting region based on radio data and the HE and VHE flux ULs computed in this work. For an equipartition magnetic field, the potential HE emitter associated to the radio emitter must be located in the jet at a distance from the BH between a few 10^{12} and a few 10^{13} cm for the HS, and a factor ~ 5 closer for the state transitions. The additional assumption that electrons are accelerated up to ~ 150 GeV with a power-law index of ~ 2 also places a putative VHE emitter in a similar region. Having the emitter closer (farther) than the region defined by these limits would violate the gamma-ray (radio) observations. This relatively narrow range of allowed distances indicates that the HE and VHE gamma-ray flux of MAXI J1820+070 (and possibly other BH-LMXBs showing evidence for non-thermal emission) seems not too far from being detectable with the current instrument sensitivities (as it was for V404 Cygni at HE), and may be detectable by future gamma-ray telescopes like the Cherenkov Telescope Array (Paredes et al. 2013; Cherenkov Telescope Array Consortium 2019; Inoue et al. 2019), or for especially bright outbursts with current instrumentation.

We also want to note that observations in the $100-1000$ GHz band would be very useful to constrain the non-thermal emitter properties by means of assuring whether non-thermal particles are accelerated up to a few hundred MeV or not, as well as establishing the transition frequency between the optically thin and optically thick synchrotron regimes.

APPENDIX: COMPUTATION OF THE GAMMA-RAY FLUX UPPER LIMITS

For each energy bin, the low-level data analysis yields: the number of gamma-ray events recorded in the direction of the source (ON region) and in control regions with only background events (OFF regions), N_{on} and N_{off}, respectively; the exposure ratio of the OFF to ON regions, τ; the effective observation time of the source after data quality cuts, t_{eff}; and the effective collection area averaged over the considered energy interval, $< A_{\text{eff}} >$. We assume a power-law distribution for the gamma rays coming from the source, i.e. $\mathrm{d}N/\mathrm{d}\varepsilon = K\varepsilon^{-\alpha}$, where K is the flux normalization constant, ε is the gamma-ray energy, and α is the spectral index. With this, the expected number of gamma rays coming from the source in the energy interval $[\varepsilon_{\text{min}}\ ,\ \varepsilon_{\text{max}}]$ can be expressed as

$$\mu = t_{\text{eff}} \int_{\varepsilon_{\text{min}}}^{\varepsilon_{\text{max}}} A_{\text{eff}}(\varepsilon) \frac{\mathrm{d}N}{\mathrm{d}\varepsilon} \mathrm{d}\varepsilon = K < A_{\text{eff}} > t_{\text{eff}} \frac{\varepsilon_{\text{min}}^{1-\alpha} - \varepsilon_{\text{max}}^{1-\alpha}}{\alpha - 1} \ . \tag{5.6}$$

In order to obtain the range of values of K compatible with the observed quantities, we fix the value of α and proceed with a maximum likelihood method as described by Rolke et al. 2005. We define a Poissonian likelihood function as

$$L = \frac{(\epsilon\mu + b)^{N_{\text{on}}}}{N_{\text{on}}!} \times \frac{(\tau b)^{N_{\text{off}}}}{N_{\text{off}}!} \times \frac{1}{\sigma_\epsilon \sqrt{2\pi}} \exp\left[-\frac{1}{2} \left(\frac{\epsilon - \epsilon_0}{\sigma_\epsilon} \right)^2 \right] , \tag{5.7}$$

where the multiplied terms correspond, from left to right, to the statistical distributions of a Poissonian signal, a Poissonian background, and a detection efficiency with a Gaussian uncertainty. The factors b and ϵ, which are treated as nuisance parameters, are the expected number of background events in the signal region, and the expected detector efficiency, respectively. The parameters ϵ_0 and σ_ϵ are the estimates for the efficiency and its standard deviation, respectively. Fixing $\epsilon_0 = 1$ allows us to account for the relative systematic uncertainty of the instrument through the value of σ_ϵ.

With the likelihood function defined, we find the values $\hat{K}$, $\hat{b}$ and $\hat{\epsilon}$ that maximize L, which can be obtained analytically for the likelihood function expressed in Eq. (5.7). We then test the null hypothesis $K = K_0$ versus the alternative hypothesis $K \neq K_0$ through a likelihood ratio test statistic:

$$\lambda = \frac{L(K_0, \hat{b}(K_0), \hat{\epsilon}(K_0))}{L(\hat{K}, \hat{b}, \hat{\epsilon})} \ , \tag{5.8}$$

where $\hat{b}(K_0)$ and $\hat{\epsilon}(K_0)$ are the values that maximize L for a given K_0. According to the Wilks theorem (Wilks 1938), under the null hypothesis the distribution of the quantity $-2\ln\lambda$ converges to a χ^2 distribution with 1 degree of freedom for large enough statistics. This allows us to find the range of K_0 compatible with the observations, i.e. being $n = \sqrt{-2 \ln \lambda}$, the null hypothesis is excluded at a $n\sigma$ level. Finally, the upper end of this range of K_0 is translated to an upper limit in flux through the assumed spectral shape for the source.

Part III

SUMMARY OF RESULTS, DISCUSSION AND CONCLUSIONS

6

SUMMARY, DISCUSSION AND CONCLUSIONS

This last chapter is devoted to summarize the main results presented in this thesis, discuss their key features and give some general conclusions. Additionally, future work prospects in the field of X-ray and gamma-ray binaries are also given.

6.1 MICROQUASAR JETS AFFECTED BY THE STELLAR WIND

The articles presented in the first two sections of Part i give insight on the interaction between HMMQ jets and the stellar wind at the binary system scales and beyond. This interaction is something to be taken into account when characterizing these systems, and it likely has an influence on the observed emission. As already pointed out by the analytical estimates in Bosch-Ramon and Barkov 2016, a non-ballistic helix-like structure is likely formed for the jet and counter-jet, with typical turn distances of a few tens of orbital separations. Arguably, this trajectory is not maintained for much longer distances owing to instability development, as well as significant wind mixing (e.g., Perucho et al. 2010). Since the phenomenological jet trajectories computed in Chapters 2 and 3 do not take these effects into account, they remain mostly valid only for (roughly) the first helix turn. Nevertheless, the particularities of the particle acceleration and cooling mechanisms in the two microquasar jet models developed during this thesis make the qualitative predictions on the radiative output not very sensitive to the exact trajectory at large scales, and can therefore be considered quite robust. We note that a more accurate computation of the path followed by jets under the influence of a strong stellar wind would require the use of complex 3-dimensional (magneto-)hydrodynamical simulations in order to properly account for the effects stated above.

6.1.1 *Inner jet regions*

In the regions close to the binary system, where the jets move at relativistic speeds and the effect of Doppler boosting is significant, the counter-jet emission is negligible in comparison with the one from the jet except for very high inclinations. The discussion on the non-thermal radiative output within a few binary separations from the system is therefore focused on the jet. Assuming that particle acceleration only takes place in the jet at the recollimation shock triggered by the stellar wind, the emission is highly concentrated within one orbital separation, except if the recollimation happens at the edge of the binary system. Only the lowest energy tail of the synchrotron emission has a significant contribution from jet regions outside the binary, and this (radio) emission is in any case highly absorbed by the wind ions through free-free absorption. It is therefore not possible to observe any extended emission from the jet as long as the assumption that particles are not accelerated beyond the recollimation shock holds.

The helical shape of the jet affects angle-dependent processes such as IC scattering, Doppler boosting, and gamma-gamma and free-free absorption (the latter through the change in the ion column density towards the observer), changing the jet radiative output with respect to a straight, unbent jet (i.e., a case that does not account for the dynamical effect of the wind). Nevertheless, these effects are only mild due to the fact that the emission mostly comes from the jet innermost regions, where the helical trajectory is only beginning to develop. The biggest observable difference between a helical and a straight jet emerges when considering a weak magnetic field, and thus dominant IC losses over synchrotron losses. This results in asymmetric LCs above ~ 10 GeV (which are not expected for straight jets) and in general more absorption close to the superior conjunction of the CO. We note that the observational signatures of a helical jet would be more pronounced if acceleration happened beyond the recollimation shock, although this is not considered in our model. This is not unlikely given that the jets have to propagate through a dense medium consisting of wind material, and therefore shocks (and consequent particle acceleration) may also be produced in the jets outside of the binary system. Additionally, due to the reduced energy losses far from the system, high-energy particles would survive longer and radiate their energy over larger distances. All this would result in a more extended helical jet emission with clearer observational features than those predicted by the model in Chapter 3.

6.1.2 *Outer jet regions*

In the model of Chapter 2, non-thermal particles are injected at the point where the jet dynamics start to be dominated by the stellar wind, located approximately at a distance of ~ 10 times the orbital separation for typical jet and massive star wind parameters. So far from the binary system, the jets are expected to have been strongly mixed with the stellar wind, effectively decreasing their speeds down to a non-relativistic regime. The larger distances to the star of these jet regions imply less prominent absorption features, as well as a smaller variation of angle-dependent quantities along the helical path. Altogether results in a much smaller modulation of the gamma-ray emission than for the inner regions. Also, negligible Doppler boosting, combined with a higher intrinsic IC emission for the counter-jet due to angular effects, makes the latter dominate the global observed

IC SED over the jet. Contrary to what happened in the inner jet regions, the lack of free-free absorption of the radio emission allows to somewhat trace the helical jets for large enough magnetic fields (and thus synchrotron emission). Helix-like shaped jets have been observed for Cygnus X-3 (Mioduszewski et al. 2001; Miller-Jones et al. 2004), and observations do not discard such phenomenon also happening in Cygnus X-1 (Stirling et al. 2001), although the physical cause of these trajectories remains unclear.

6.1.3 *Sources of uncertainty and additional considerations*

The models discussed above make use of a number of assumptions and simplifications which could significantly affect the obtained results. There are also some model parameters relevant for the radiative output of the system that are very difficult to constrain observationally, making the results very dependent on the values taken for them. In this section, the main sources of uncertainty in our models, coming both from parameter uncertainties and assumed simplifications, are addressed.

A first consideration to take into account is the fact that, for simplicity, the stellar wind is assumed isotropic and homogeneous. Nevertheless, massive stars normally feature a non-homogeneous clumpy wind (Owocki and Cohen 2006; Moffat 2008). This makes jet disruption and mixing with the stellar wind more likely than for an homogeneous case (Perucho and Bosch-Ramon 2012), effectively decreasing the distance range up to which our phenomenological trajectory computation is valid. Moreover, wind clumps interacting with the jets may also have a non-negligible contribution to the total radiative output of the system through the shocks that they generate (de la Cita et al. 2017). Regarding absorption processes, for a given mass-loss rate, the presence of clumps in the wind effectively increases its free-free opacity by up to a factor of 10, for typical clumping factors of massive stars (e.g., Muijres et al. 2011). This would make free-free absorption significant up to frequencies $\lesssim 3$ times larger than in the homogeneous case (we note that this is not relevant for the outer jet regions, where free-free absorption does not play an important role). Finally, wind clumping may also introduce temporal, minute-timescale variations of the mass accretion rate in HMMQs (El Mellah et al. 2018). This would be translated to variations in the jet power, which would in turn modify the balance between jet and wind pressures and momentum rates, and thus the overall shape of the helical jets. Another consideration relative to the stellar wind is that some degree of beaming of the latter towards the CO is expected, especially for slow winds (El Mellah et al. 2019). Such effect would decrease the wind density outside of the orbital plane, decreasing its overall effect on the jets. Nonetheless, we note that this does not affect much the models in Chapters 2 and 3 since we are considering fast winds with speeds of ~ 2000 km s^{-1} typical for O-type stars, for which beaming is not so important.

Even though the models presented are not applied to specific sources, there are a number of quantities that are difficult to constrain observationally regardless of the source. Some of these quantities include the magnetic field strength, the acceleration efficiency or the amount of energy in the form of non-thermal particles. Regarding the magnetic field strength, the articles in Chapters 2 and 3 already explore explicitly its effect on the results. The acceleration efficiency basically affects the maximum energy that the non-thermal particles can obtain (which also depends on the magnetic field if acceleration happens under the diffusive shock acceleration mechanism, as we assume). This maximum particle energy in turn affects the synchrotron and IC SEDs by shifting their peaks, and thus setting the position of the energy cutoffs in the spectrum. Finally, the non-thermal energy budget acts as a normalization of the overall emission of the system, increasing or decreasing the radiative output by a given factor independent of the energy of the emitted radiation. More detailed and specific discussions on the different sources of uncertainty in the models can be found in the corresponding articles, to which the reader is referred for more information.

6.2 PULSAR-WIND SYSTEMS ALONG THE ORBIT

In the following, the main conclusions extracted from the pulsar-wind model are summarized both for a generic case and for the specific model parameters corresponding to LS 5039. We note that similar sources of uncertainty as those described in the previous section are also present in this case, namely the validity of the hydrodynamic computation only up to a few tens of orbital separations, and some poorly constrained parameters the values of which can significantly affect the radiative output of the system. Also, only two accelerators are assumed, one at the two-wind stagnation point and the other at the Coriolis shock (located at a few orbital separations from the pulsar). This limits the energetics of non-thermal particles far from the binary system, since they are mostly cooled down once they reach distances of $5-10$ orbital separations. This effect could be (partially) compensated with the inclusion of additional shocks downstream of the Coriolis turnover, which are actually expected according to numerical simulations (Bosch-Ramon et al. 2015). This is not done in our model in order not to add too much complexity, given the uncertainties present in the properties of these shocks.

6.2.1 *General scenario*

The generic case assumes a pulsar with a spin-down luminosity of 3×10^{36} erg s^{-1} orbiting a typical O-type star in a circular orbit with a separation of 3×10^{12} cm and a period of 5 days. Under these conditions and with the same available energy budget for non-thermal particles in both accelerators, the inner region of the emitter (between the wind standoff and the Coriolis turnover locations) generally contributes less to the total observed radiation than the outer region (beyond the Coriolis turnover). The exception to this happens close to the inferior conjunction of the pulsar and for sufficiently high inclinations, for which Doppler boosting makes the inner region dominate the emission. The proximity to the star also makes radio and VHE gamma-ray emission to be considerably absorbed for most orbital phases, through free-free and gamma-gamma processes, respectively. As with microquasar jets at large scales, the synchrotron radio emission from the outer regions is extended and traces part of the spiral structure of the outflow for high enough magnetic fields.

6.2.2 *The specific case of LS 5039*

The parameters that best allow us to reproduce the observed behavior of LS 5039 include a very high acceleration efficiency of $\eta_{\rm acc} = 0.8$ (with the energy gain rate of the particles being $\dot{E}'_{\rm acc} = \eta_{\rm acc} ecB'$), and a hard particle injection with power-law index of 1.3. Also, the outer region is given a higher non-thermal energy budget, since it reproduces better the observations of the source. The average X-ray, HE and VHE fluxes are well explained by the model, although it fails to properly account for the HE gamma-ray modulation. The VHE LC is well reproduced, including the double peak around the inferior conjunction of the pulsar, although the emission is underpredicted close to the superior conjunction, where it is almost totally absorbed. This strong absorption would be alleviated with the use of a 3D emitter, instead of the current 1D emitter located along the "axis" of the CD, since that would locate part of the emitter farther from the star. The inclusion of particle reacceleration beyond the Coriolis shock would also contribute in this direction, allowing the most energetic particles to reach farther along the shocked structure. Reacceleration is probably needed for a meaningful comparison of the model predictions with the radio observations, since the latter extend with significant fluxes up to scales much larger than those probed in our work (Moldón et al. 2012). Besides this, the biggest flaw of the model comes in the MeV range, for which observations are underpredicted by a factor of ~ 5. This underestimation of the MeV emission is a common issue for many models applied to LS 5039 (e.g., Takahashi et al. 2009; Zabalza et al. 2013; Dubus et al. 2015), and seems to point towards the need of including (at least) the contribution to the MeV radiation of the unshocked pulsar wind (see Bosch-Ramon 2021, for the unshocked pulsar wind emission around periastron), and synchrotron emission of secondary electron-positron pairs produced by the interaction of gamma rays with stellar photons (e.g., Bosch-Ramon et al. 2008; Cerutti et al. 2010).

6.3 OBSERVATIONS OF MAXI J1820+070

MAXI J1820+070 is the brightest BH-LMXB in X-rays ever observed by the current generation of IACT telescopes. The source was observed with the MAGIC telescopes during an outburst in 2018, for a total of 22.5 h after data quality cuts. These observations were performed when MAXI J1820+070 was in the HS, as well as during the HS–SS and the SS–HS state transitions. The MAGIC observations were complemented with *Fermi*/LAT data at HE gamma rays, as well as additional data from radio, optical, and X-ray telescopes.

The analysis of the VHE data does not yield any significant detection of the source at these energies. Instead, differential and integral flux ULs are given for each source state with a 95% C.L. and assuming a power-law photon spectrum with index -2.5. The differential ULs are between 1 and 10% of the Crab Nebula flux, depending on the state of the source and the energy bin. HE emission is also not detected from MAXI J1820+070, and ULs with the same C.L. and assumed spectral shape as for the VHE analysis are computed. The evolution of the radio and hard X-ray fluxes follows the expected behavior for a BH-LMXB in outburst, with radio-emitting jets coexisting with a corona emitting hard X-rays during the HS, both of them disappearing in the SS.

The computed HE and VHE ULs, together with the multiwavelength data from radio to X-rays available for MAXI J1820+070, allow us to constrain significantly the properties of a potential gamma-ray emitter in this source. For this purpose, some simple analytical estimations are made using a number of reasonable assumptions, mainly regarding the extrapolation of the radio-emitting electron particle distribution at high energies. With this, the particles responsible for the synchrotron radio emission are the same as those responsible for the potential HE emission via IC with X-ray photons, and we can put constraints on the properties of the jet regions responsible for the potential HE emission through the available radio data. Among others, the putative HE (and radio) emitter is constrained to have a linear size in the range $\approx (3.7 - 24) \times 10^{11}$ cm, depending on the source state. This range of values, combined with the *Fermi*-LAT ULs and the X-ray fluxes, sets a distance from the emitter to the BH between $\sim 10^{12}$ and a few times 10^{13} cm. As long as the non-thermal particles reach the required energies, the jet regions responsible for the potential VHE emission are also limited in space to a similar range as the HE emitter. If these putative gamma-ray emitters were closer to the BH, the gamma-ray ULs would be violated, whereas having the emitters farther than the estimated distance range would contradict the radio observations.

6.4 FUTURE WORK PROSPECTS

From the theoretical point of view, a future improvement to the pulsar-wind model that would make it more realistic would be the proper computation of the 3-dimensional CD resulting from the wind-wind interaction. This would substitute the current, simplified 1D emitter at the axis of a conical CD. The evolution of the particle distribution and its radiation could then be computed for an emitter made of a number of streamlines flowing within the defined 3D shape. These lines would propagate farther from the star, and with different orientations, than the current 1D emitter consisting of a single streamline. Therefore, processes depending on the distance to the star and the flow direction, like IC, gamma-gamma absorption, or free-free absorption, would see their effects significantly modified by the new, more realistic emitter. Both analytical (e.g., Usov 1992; Cantó et al. 1996) and numerical (e.g., Bosch-Ramon 2021) prescriptions exist for the computation of the shape of the CD, with the analytical ones only being valid for an axisymmetric CD. This axisymmetry is only realistic as long as orbital effects are small, i.e., as long as we focus our study to the emitter regions well before the Coriolis turnover. Even in this case, a reorientation of the CD with respect to the star-pulsar direction is needed in order to account for the non-radial component of the stellar wind in the pulsar reference frame. The inclusion of orbital effects affects non-trivially the shape of the CD, and its computation needs to make use of some simplifications regarding how momentum is transferred between the stellar and pulsar winds (Bosch-Ramon 2021).

Another improvement to both the microquasar and pulsar-wind models would be the inclusion of a non-isotropic stellar wind. This is especially relevant for those systems with a Be stellar companion, which features a circumstellar decretion disk in its equatorial plane. The material in these disks follows quasi-Keplerian orbits, and has a much higher density than its polar counterpart (e.g., Carciofi 2011). The dynamic and radiative influence of a decretion disk on the outflows is therefore very different to that of a radial isotropic wind, and should be considered for a proper characterization of binary systems hosting a Be star. Unless the equatorial plane of the star and the orbital plane are largely misaligned, the effect of the decretion disk on the relativistic outflow should be particularly important in the pulsar-wind scenario. The inclusion of this feature in our model would allow for a better characterization of binary systems such as LS I +61 303, PSR J2032+4127, PSR B1259-63 or HESS J0632+057, all of them consisting of a CO (confirmed to be a pulsar in PSR J2032+4127 and PSR B1259-63) and a Be star.

Regarding the work performed on MAXI J1820+070, a possible improvement of the estimations would be to take into account a jet-like emitter instead of a spherical one located at a given distance from the BH, especially in the HS of the source. Additionally, other radio spectral indices, like the one obtained by Tetarenko et al. 2021, could be considered, which would affect the extrapolated radio flux at the synchrotron transition frequency from the optically thin to the optically thick regime. In any case, the study performed for MAXI J1820+070 shows that we may be not too far from detecting (HE or VHE) gamma-ray emission from low-mass microquasars in outburst. It is therefore important to keep monitoring these sources in order to be able to react fast in case of strong flares. This is reinforced by the fact that CTA (Cherenkov Telescope Array Consortium 2019), the next generation IACT observatory with improved sensitivity and increased energy range, will begin operations within the next few years. Moreover, even if a source is not detected, the gamma-ray ULs combined with multiwavelength data can still be used to put significant constrains on the system properties. This also applies, even more given their physical conditions, to HMMQs, which have never been detected at VHE (although we note the detection hint of Cygnus X-1 reported in Albert et al. 2007). In particular, it would be interesting to perform a global analysis of all the MAGIC data available for Cygnus X-3 (see Appendix a), since it could allow us to put the most stringent constrains up to date regarding the VHE emission of the source.

Part IV

APPENDICES

a

GAMMA-RAY OBSERVATIONS OF CYGNUS X-3 WITH FERMI-LAT AND MAGIC

This appendix contains a report on HE and VHE gamma-ray observations of Cygnus X-3 obtained during the course of this PhD Thesis. The ultimate goal was the detection of VHE gamma-ray emission from Cygnus X-3 with MAGIC after triggering observations based on the UB Fermi pipeline at HE gamma rays. Upper limits at VHE are reported.

A.1 INTRODUCTION

Cygnus X-3 (Cyg X-3) is a high-mass microquasar hosting a Wolf-Rayet star and a CO of unknown nature, with both the BH and (weakly magnetized) NS scenarios being possible. Zdziarski et al. 2013 estimated a mass of the CO of $2.4^{+2.1}_{-1.1}$ $M_\odot$ and a companion mass of $\sim 10^{+3.9}_{-2.8}$ $M_\odot$. The two objects orbit around each other in a very close orbit with a period of 4.8 h (Parsignault et al. 1976), and the distance to the source was set to 7.4 ± 1.1 kpc by McCollough et al. 2016. At this distance, the derived (absorption-corrected) bolometric X-ray luminosity of Cyg X-3 reaches up to several times 10^{38} erg s^{-1} during flares, making it the brightest of the known X-ray binaries. Taking into account that the Eddington luminosity for an object of mass M is $1.26 \times 10^{38} (M/M_\odot)$ erg s^{-1}, we note that the inferred luminosity of Cyg X-3 is above the Eddington limit for most of the CO mass range stated above, and always in the NS scenario ($M \lesssim 2.5\ M_\odot$). Extended radio emission in the form of jets has also been observed from Cyg X-3 during some flaring episodes (e.g., Martí et al. 2000; Martí et al. 2001; Mioduszewski et al. 2001; Miller-Jones et al. 2004; Egron et al. 2017). Being an X-ray binary, Cyg X-3 shows variable emission at different frequencies depending on the state of the source, which is typically characterized through the shape of its X-ray spectrum (see Sect. 5.1). This variability is especially significant at radio wavelengths, for which the flux can change more than 3 orders of magnitude between different source states (e.g., Egron et al. 2021).

As mentioned in Chapter 5, Cyg X-3 is one of the two only known microquasars to have been consistently detected at HE with a significance above 5σ (Tavani et al. 2009b; Fermi LAT Collaboration et al. 2009), the other one being Cyg X-1 (which is also a high-mass system). Additionally, there is also a strong hint of detection of the low-mass system V404 Cyg at a $\sim 4\sigma$ level during a flare in 2015 (Loh et al. 2016; Piano et al. 2017). Emission at VHE has never been detected from

Cyg X-3 or any other microquasar (see Aleksić et al. 2010 for Cyg X-3, and Aleksić et al. 2011, 2015; MAGIC Collaboration et al. 2017; Ahnen et al. 2017; MAGIC Collaboration et al. 2018; H. E. S. S. Collaboration et al. 2018 for other sources), although we note the $\sim 4\sigma$ detection hint of Cygnus X-1 in a single night by MAGIC (Albert et al. 2007). Another possible exception to the non-detection of microquasars at VHE is the case of SS433, for which the HAWC Collaboration claimed a detection of ~ 20 TeV photons coming from a region very far from the binary system, where the jets interact with the supernova remnant around the source (Abeysekara et al. 2018).

This appendix focuses on the gamma-ray emission of Cyg X-3 by making use of an automatic pipeline for the analysis of *Fermi*-LAT HE data (Sect. a.2), and MAGIC VHE observations triggered by the latter results (Sect. a.3). In the following, the observations of Cyg X-3 in these two energy ranges are described.

A.2 MONITORING WITH FERMI-LAT

During the last ~ 11 years, Cyg X-3 has been actively monitored through a *Fermi*-LAT analysis pipeline developed and maintained by the high-energy astrophysics group of the University of Barcelona. This pipeline automatically runs at noon on a daily basis, and analyzes all the source data[1] available from the previous day. The results of the analysis pipeline include an integral flux of gamma rays with energies above $\varepsilon > 100$ MeV, and a test statistic (TS) that evaluates the goodness of a likelihood fit to the data. It has been shown that the latter behaves approximately as the square of the detection significance (e.g., Mattox et al. 1996). We refer the reader to Zabalza 2011; Galindo 2018 for the details on the *Fermi*-LAT analysis and the working procedure of the pipeline, including how background sources are treated.

For this work, we use *Fermi*-LAT data of Cyg X-3 taken during the course of this PhD thesis, specifically between MJD 57874 and 59304 (1 May 2017 – 31 March 2021), and automatically analyzed by the pipeline. The fluxes and TSs for this period are shown in Fig. a.1. The average flux of Cyg X-3 at $\varepsilon > 100$ MeV was of $(3.5 \pm 0.1) \times 10^{-7}$ cm^{-2} s^{-1}, with the quoted error corresponding only to the statistical uncertainty of the average computation.

The main function of the pipeline is to identify flaring episodes of Cyg X-3 at HE gamma rays, so that a quick reaction is possible and MAGIC observations can be scheduled for the same day in which the pipeline results are obtained (i.e. about 1 day after the *Fermi*-LAT data were taken). We want to select those days in which the source is clearly detected (high TS) and is emitting more than it usually does (flux significantly above the average). As seen in Fig. a.2, the *Fermi*-LAT

---

[1] *Fermi*-LAT data are public and can be downloaded from the data server at `https://fermi.gsfc.nasa.gov/cgi-bin/ssc/LAT/LATDataQuery.cgi`

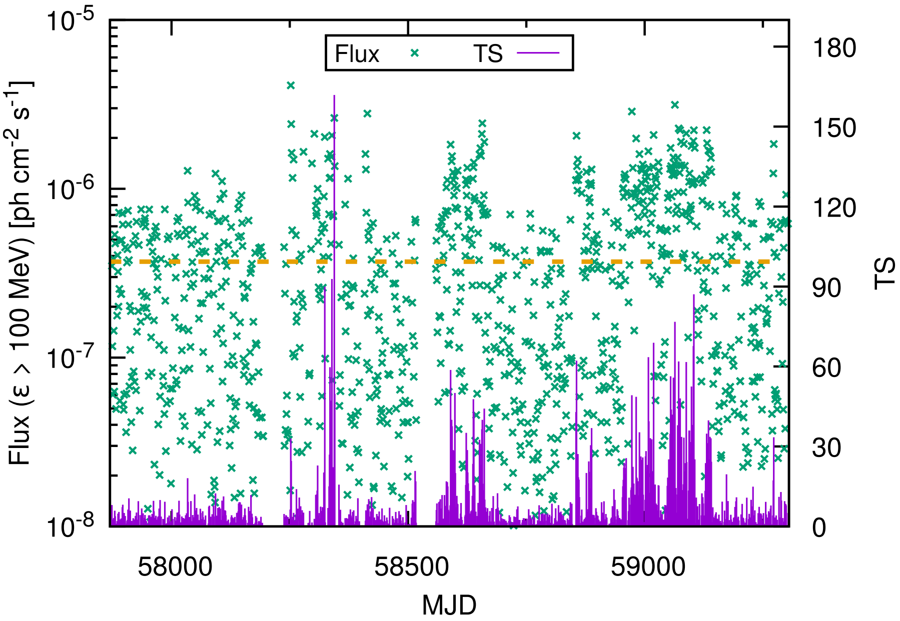

Figure a.1: Daily values of the *Fermi*-LAT integral flux and TS of Cyg X-3 between MJD 57874 and 59304. Error bars in the fluxes are not shown for visualization purposes. The dashed orange line shows the average flux over the whole period.

flux and TS have a clear positive correlation. A visual inspection of the data allows us to set a TS limit of 20, above which all fluxes are larger than the average one. This is also the case when considering the error bars, as seen in Fig. a.3, in which a zoom has been made around the top right quarter of Fig. a.2. Therefore, we adopt the strategy of setting a TS = 20 as the triggering threshold for MAGIC observations.

A.3 MAGIC OBSERVATIONS

Observations of Cyg X-3 with the MAGIC telescopes started in 2006 and have been regularly performed until nowadays. The results of the first 3 years of data (amounting to 69.2 h, 56.7 h after quality cuts) can be found in Aleksić et al. 2010. Between 2010 and 2021, a total of 170.3 h of observations were devoted to Cyg X-3, both during flaring and quiescent episodes. Out of them, we focus here on the data taken during the same period as the *Fermi*-LAT ones, i.e. between MJD 57874 and 59304. During this time, 54.3 h of data were taken, always during flaring episodes of the source. This does not necessarily mean that the *Fermi*-LAT TS was always larger than 20, since oscillations of this quantity happen within a flare (see Fig. a.1), and MAGIC data are taken ∼ 1 day later than the *Fermi*-LAT ones. After removing bad quality data (mostly due to bad weather), 40.0 h of MAGIC observations remain, covering a zenith angle range from 5 to 50 deg. The details of these observations are shown in Table a.1.

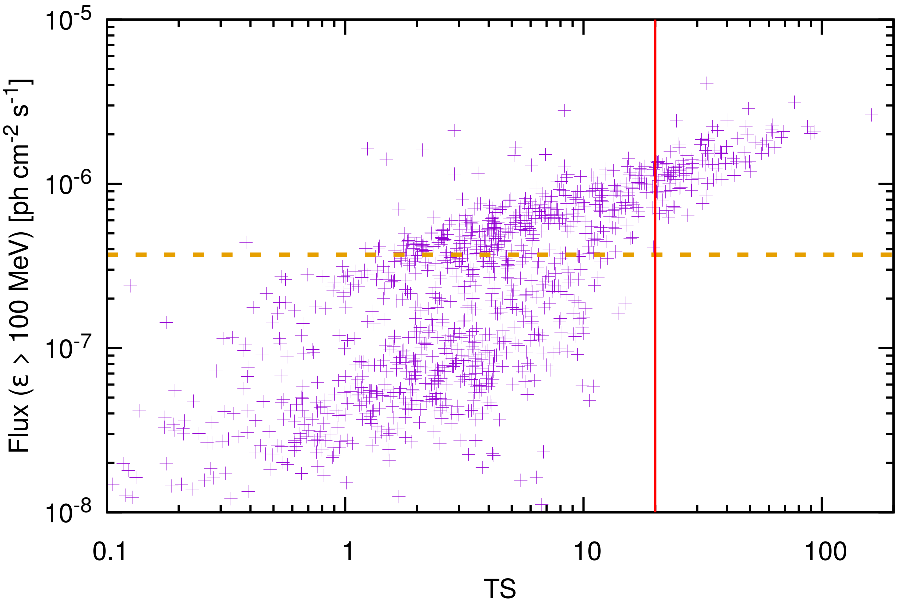

Figure a.2: *Fermi*-LAT flux as a function of the TS for Cyg X-3 between MJD 57874 and 59304. The dashed orange line shows the average flux, and the vertical red line shows the chosen TS limit above which the source is considered to be flaring and MAGIC observations may be triggered. Flux error bars are not shown for visualization purposes.

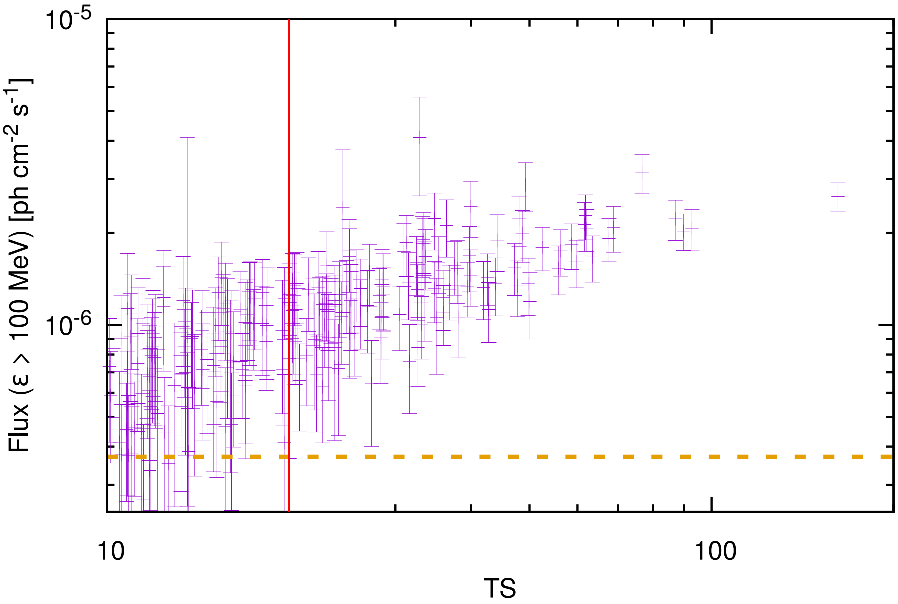

Figure a.3: Same as in Fig. a.2, but zooming in on the top-right corner. Flux error bars are included.

Table a.1: Summary of the observations of Cyg X-3 by the MAGIC telescopes, after data quality cuts, between MJD 57874 and 59304. The observation time, zenith angle median and integral flux ULs above 100 GeV are shown for each day, as well as for the total sample. The ULs are computed for a 95% C.L. and assuming a power-law spectral index of −2.6.

MJD	Time [h]	Zenith angle [deg]	UL ($\varepsilon > 100$ GeV) [10^{-11} cm^{-2} s^{-1}]
58306	1.1	23.2	1.7
58307	1.1	17.1	4.9
58341	3.0	15.6	2.9
58346	2.0	14.0	1.1
58347	1.3	13.3	0.91
58583	1.0	43.6	4.0
58639	2.1	36.4	1.7
58640	2.6	35.8	0.97
58641	1.5	26.3	1.3
58659	1.6	39.6	5.1
58660	1.5	33.8	3.1
58663	2.0	31.3	2.1
59020	1.8	15.5	3.1
59024	2.6	15.0	2.4
59056	1.8	13.9	3.0
59074	0.8	24.0	4.7
59075	0.5	19.7	3.7
59077	1.8	13.9	4.2
59100	0.7	12.8	0.25
59101	1.9	13.7	4.8
59102	2.0	13.8	2.0
59103	1.4	13.7	0.59
59106	2.0	14.5	3.1
59133	1.9	33.3	0.55
TOTAL	40.0	18.0	0.53

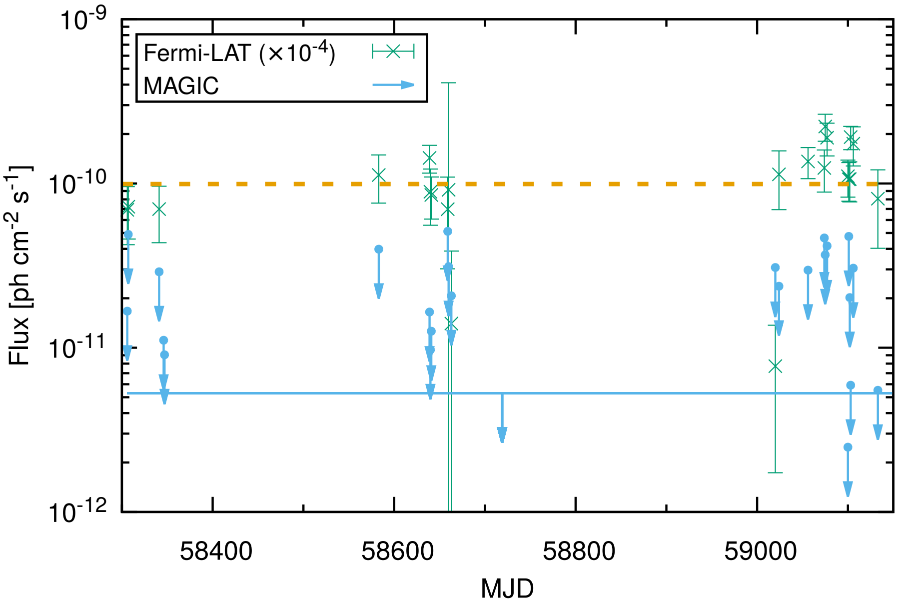

Figure a.4: Light curve with the obtained MAGIC integral flux ULs above 100 GeV stated in Table a.1 (blue arrows). The blue horizontal line at the bottom of the plot represents the UL for the whole dataset. The *Fermi*-LAT fluxes above 100 MeV on those days are also shown (green crosses, multiplied by 10^{-4} for visualization purposes), together with their average (dashed orange line).

MAGIC data are analyzed following the standard procedure described in Aleksić et al. 2016b. The analysis does not yield a significant detection of Cyg X-3, neither for a daily time binning or for the whole data set (the detection significances are always below 2σ), and only flux ULs are obtained. These ULs are computed following a maximum-likelihood ratio test, as in Rolke et al. 2005 (see also the appendix in Chapter 5). The daily and total integral flux ULs above 100 GeV are shown in Table a.1 and Fig. a.4. They are computed for a 95% C.L. and assuming a power-law spectrum with spectral index of −2.6, i.e. $dN/d\varepsilon \propto \varepsilon^{-2.6}$.

The differential flux ULs of Cyg X-3 accounting for all the data analyzed in this thesis are shown in Fig. a.5. For comparison, the results from Aleksić et al. 2010, obtained using mono data taken with a single MAGIC telescope, are also represented. That work used a total of 56.7 h of good-quality data obtained following radio and HE gamma-ray flares, and used a spectral index of −2.6 and a C.L. of 95%, as in this thesis. Even with a smaller observation time, the differential ULs obtained in this work are tighter than those reported by Aleksić et al. 2010, except for the energy bin around 600 GeV. This is consistent with the significant improvement of the MAGIC sensitivity at all energies during the $\sim$ 10-year time gap between the two data sets. This sensitivity improvement mainly (although not only) comes from the use of stereo observations, which only became possible after 2010,

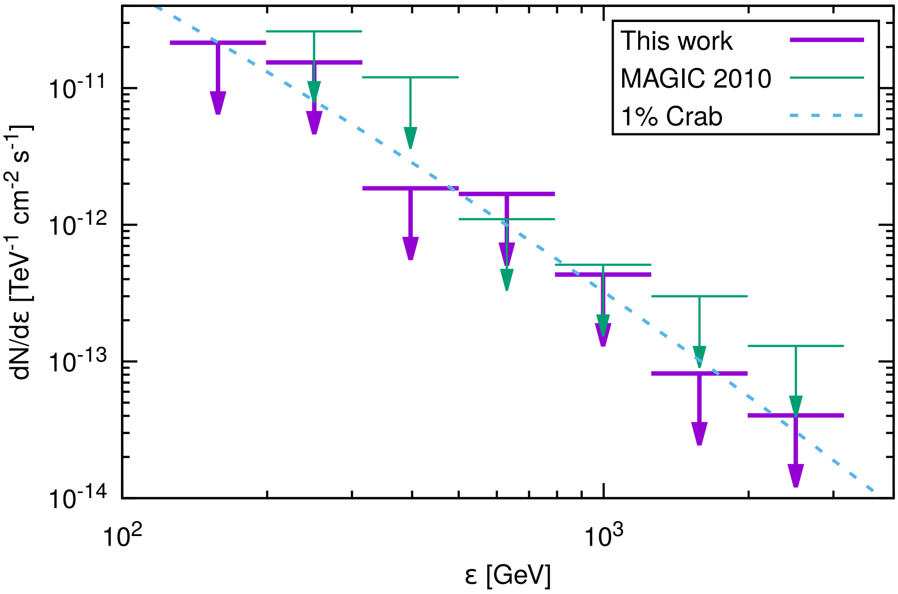

Figure a.5: Differential flux ULs of Cyg X-3 from the MAGIC data listed in Table a.1. Thick purple lines show the results from this work (for the whole data sample), while thin green lines represent the results from Aleksić et al. 2010. The dashed blue line represents 1% of the differential spectrum of the Crab Nebula.

instead of mono ones (see Aleksić et al. 2016b). In particular, given that the current sensitivity is especially better at the lowest energies, the energy threshold of the data could be lowered from 250 GeV to 100 GeV, and ULs could be given at lower energies than those reported in Aleksić et al. 2010. The looser flux UL obtained for the energy bin around 600 GeV could be explained by the variable nature of ULs owing to small statistical fluctuations in the number of signal and background events (which is inherent to how they are computed; see the appendix in Chapter 5).

LIST OF ACRONYMS

BH black hole

BH-LMXB black hole low-mass X-ray binary

CD contact discontinuity

C.L. confidence level

CO compact object

HE high-energy

HMMQ high-mass microquasar

HS hard state

IACT imaging atmospheric Cherenkov telescope

IC inverse Compton

LC light curve

NS neutron star

SED spectral energy distribution

SS soft state

TS test statistic

UL upper limit

VHE very high-energy

BIBLIOGRAPHY

Abdo, A. A. et al. (2009). “Detection of 16 Gamma-Ray Pulsars Through Blind Frequency Searches Using the Fermi LAT.” In: *Science* 325.5942, p. 840.

Abdollahi, S. et al. (2020). “Fermi Large Area Telescope Fourth Source Catalog.” In: *ApJS* 247.1, 33, p. 33.

Abeysekara, A. U. et al. (2013). “Sensitivity of the high altitude water Cherenkov detector to sources of multi-TeV gamma rays.” In: *Astroparticle Physics* 50, pp. 26–32.

Abeysekara, A. U. et al. (2018). “Very-high-energy particle acceleration powered by the jets of the microquasar SS 433.” In: *Nature* 562.7725, pp. 82–85.

Aharonian, F. et al. (2006). “The H.E.S.S. Survey of the Inner Galaxy in Very High Energy Gamma Rays.” In: *ApJ* 636.2, pp. 777–797.

Ahnen, M. L. et al. (2017). “MAGIC observations of the microquasar V404 Cygni during the 2015 outburst.” In: *MNRAS* 471.2, pp. 1688–1693.

Albert, J. et al. (2007). “Very High Energy Gamma-Ray Radiation from the Stellar Mass Black Hole Binary Cygnus X-1.” In: *ApJ* 665.1, pp. L51–L54.

Aleksić, J. et al. (2010). “Magic Constraints on γ-ray Emission from Cygnus X-3.” In: *ApJ* 721.1, pp. 843–855.

Aleksić, J. et al. (2011). “A Search for Very High Energy Gamma-Ray Emission from Scorpius X-1 with the Magic Telescopes.” In: *ApJ* 735.1, L5, p. L5.

Aleksić, J. et al. (2015). “MAGIC observations of MWC 656, the only known Be/BH system.” In: *A&A* 576, A36, A36.

Aleksić, J. et al. (2016a). “The major upgrade of the MAGIC telescopes, Part I: The hardware improvements and the commissioning of the system.” In: *Astroparticle Physics* 72, pp. 61–75.

Aleksić, J. et al. (2016b). “The major upgrade of the MAGIC telescopes, Part II: A performance study using observations of the Crab Nebula.” In: *Astroparticle Physics* 72, pp. 76–94.

Atri, P. et al. (2020). “A radio parallax to the black hole X-ray binary MAXI J1820+070.” In: *MNRAS* 493.1, pp. L81–L86.

Bai, X. et al. (2019). “The Large High Altitude Air Shower Observatory (LHAASO) Science White Paper.” In: *arXiv e-prints*, arXiv:1905.02773, arXiv:1905.02773.

Barkov, M. V. and V. Bosch-Ramon (2016). “The origin of the X-ray-emitting object moving away from PSR B1259-63.” In: *MNRAS* 456, pp. L64–L68.

Barkov, M. V. and V. Bosch-Ramon (2018). "A hydrodynamics-informed, radiation model for HESS J0632 + 057 from radio to gamma-rays." In: *MNRAS* 479, pp. 1320–1326.

Bogovalov, S. V. et al. (2008). "Modelling interaction of relativistic and non-relativistic winds in binary system PSR B1259-63/SS2883 - I. Hydrodynamical limit." In: *MNRAS* 387.1, pp. 63–72.

Bolmont, J. et al. (2014). "The camera of the fifth H.E.S.S. telescope. Part I: System description." In: *Nuclear Instruments and Methods in Physics Research A* 761, pp. 46–57.

Bosch-Ramon, V. (2009). "Studying the properties of the radio emitter in LS 5039." In: *A&A* 493.3, pp. 829–833.

Bosch-Ramon, V. (2021). "Properties of a hypothetical cold pulsar wind in LS 5039." In: *A&A* 645, A86, A86.

Bosch-Ramon, V. and M. V. Barkov (2011). "Large-scale flow dynamics and radiation in pulsar γ-ray binaries." In: *A&A* 535, A20, A20.

Bosch-Ramon, V. and M. V. Barkov (2016). "The effects of the stellar wind and orbital motion on the jets of high-mass microquasars." In: *A&A* 590, A119, A119.

Bosch-Ramon, V., M. V. Barkov, and M. Perucho (2015). "Orbital evolution of colliding star and pulsar winds in 2D and 3D: effects of dimensionality, EoS, resolution, and grid size." In: *A&A* 577, A89, A89.

Bosch-Ramon, V. and D. Khangulyan (2009). "Understanding the Very-High Emission from Microquasars." In: *Int. J. Mod. Phys. D* 18, pp. 347–387.

Bosch-Ramon, V., D. Khangulyan, and F. A. Aharonian (2008). "Non-thermal emission from secondary pairs in close TeV binary systems." In: *A&A* 482.2, pp. 397–402.

Bosch-Ramon, V. and F. M. Rieger (2012). "Exploring Particle Acceleration in Gamma-Ray Binaries." In: *Astroparticle*, pp. 219–225.

Bosch-Ramon, V. et al. (2017). "HESS J0632+057: hydrodynamics and non-thermal emission." In: *MNRAS* 471, pp. L150–L154.

Bright, J. S. et al. (2020). "An extremely powerful long-lived superluminal ejection from the black hole MAXI J1820+070." In: *Nature Astronomy* 4, pp. 697–703.

Buisson, D. J. K. et al. (2019). "MAXI J1820+070 with NuSTAR I. An increase in variability frequency but a stable reflection spectrum: coronal properties and implications for the inner disc in black hole binaries." In: *MNRAS* 490.1, pp. 1350–1362.

Cantó, J., A. C. Raga, and F. P. Wilkin (1996). "Exact, Algebraic Solutions of the Thin-Shell Two-Wind Interaction Problem." In: *ApJ* 469, p. 729.

Carciofi, A. C. (2011). "The circumstellar discs of Be stars." In: *Active OB Stars: Structure, Evolution, Mass Loss, and Critical Limits*. Ed. by C. Neiner et al. Vol. 272, pp. 325–336.

Celma, C. (2019). MA thesis. Universitat Politècnica de Catalunya.

Cerutti, B. et al. (2010). "Modeling the three-dimensional pair cascade in binaries. Application to LS 5039." In: *A&A* 519, A81, A81.

Chakraborty, S. et al. (2020). "A spectral study of the black hole X-ray binary MAXI J1820+070 with AstroSat and NuSTAR." In: *MNRAS* 498.4, pp. 5873–5884.

Cherenkov Telescope Array Consortium (2019). *Science with the Cherenkov Telescope Array*.

Colomé, J. et al. (2010). "The OAdM Robotic Observatory." In: *Advances in Astronomy* 2010, 183016, p. 183016.

Del Santo, M. and A. Segreto (2018). "The hard X-ray spectrum of MAXI J1820+070 observed by Swift/BAT." In: *The Astronomer's Telegram* 11427, p. 1.

de la Cita, V. M. et al. (2017). "Gamma rays from clumpy wind-jet interactions in high-mass microquasars." In: *A&A* 604, A39, A39.

Dermer, C. D. and R. Schlickeiser (1994). "On the Location of the Acceleration and Emission Sites in Gamma-Ray Blazars." In: *ApJS* 90, p. 945.

Drury, L. O. (1983). "An introduction to the theory of diffusive shock acceleration of energetic particles in tenuous plasmas." In: *Reports on Progress in Physics* 46, pp. 973–1027.

Dubus, G., A. Lamberts, and S. Fromang (2015). "Modelling the high-energy emission from gamma-ray binaries using numerical relativistic hydrodynamics." In: *A&A* 581, A27, A27.

Dubus, G. (2013). "Gamma-ray binaries and related systems." In: *A&A Rev.* 21, 64, p. 64.

Duchêne, G. and A. Kraus (2013). "Stellar Multiplicity." In: *ARA&A* 51.1, pp. 269–310.

Egron, E. et al. (2017). "Single-dish and VLBI observations of Cygnus X-3 during the 2016 giant flare episode." In: *MNRAS* 471.3, pp. 2703–2714.

Egron, E. et al. (2021). "Investigating the Mini and Giant Radio Flare Episodes of Cygnus X-3." In: *ApJ* 906.1, 10, p. 10.

El Mellah, I., J. O. Sundqvist, and R. Keppens (2018). "Accretion from a clumpy massive-star wind in supergiant X-ray binaries." In: *MNRAS* 475.3, pp. 3240–3252.

El Mellah, I. et al. (2019). "Formation of wind-captured disks in supergiant X-ray binaries. Consequences for Vela X-1 and Cygnus X-1." In: *A&A* 622, A189, A189.

Fabian, A. C. et al. (2020). "The soft state of the black hole transient source MAXI J1820+070: emission from the edge of the plunge region?" In: *MNRAS* 493.4, pp. 5389–5396.

Fender, R. and T. Belloni (2012). "Stellar-Mass Black Holes and Ultraluminous X-ray Sources." In: *Science* 337.6094, p. 540.

Fender, R. and T. Muñoz-Darias (2016). "The Balance of Power: Accretion and Feedback in Stellar Mass Black Holes." In: *Astrophysical Black Holes, Lecture Notes in Physics, Volume 905. ISBN 978-3-319-*

19415-8. Springer International Publishing Switzerland, 2016, p. 65. Vol. 905. Springer International Publishing Switzerland, p. 65.

Fermi LAT Collaboration et al. (2009). "Modulated High-Energy Gamma-Ray Emission from the Microquasar Cygnus X-3." In: *Science* 326, p. 1512.

Galindo, D. (2018). "Study of the extreme gamma-ray emission from Supernova Remnants and the Crab Pulsar." PhD thesis. Departament de Física Quàntica i Astrofísica, Institut de Ciències del Cosmos (ICCUB), Universitat de Barcelona (IEEC-UB).

Gandhi, P. et al. (2019). "Gaia Data Release 2 distances and peculiar velocities for Galactic black hole transients." In: *MNRAS* 485.2, pp. 2642–2655.

Gendreau, K. C., Z. Arzoumanian, and T. Okajima (2012). "The Neutron star Interior Composition ExploreR (NICER): an Explorer mission of opportunity for soft x-ray timing spectroscopy." In: *Space Telescopes and Instrumentation 2012: Ultraviolet to Gamma Ray*. Ed. by T. Takahashi, S. S. Murray, and J.-W. A. den Herder. Vol. 8443. Society of Photo-Optical Instrumentation Engineers (SPIE) Conference Series, p. 844313.

Gould, R. J. and G. P. Schréder (1967). "Opacity of the Universe to High-Energy Photons." In: *Physical Review* 155, pp. 1408–1411.

H. E. S. S. Collaboration et al. (2018). "A search for very high-energy flares from the microquasars GRS 1915+105, Circinus X-1, and V4641 Sgr using contemporaneous H.E.S.S. and RXTE observations." In: *A&A* 612, A10, A10.

Hinton, J. (2009). "Ground-based gamma-ray astronomy with Cherenkov telescopes." In: *New Journal of Physics* 11.5, 055005, p. 055005.

Inoue, S. et al. (2019). "KSP: Transients." In: *Science with the Cherenkov Telescope Array*. Ed. by B. S. Acharya et al., pp. 163–198.

Johnston, S. et al. (1992). "PSR 1259-63: A Binary Radio Pulsar with a Be Star Companion." In: *ApJ* 387, p. L37.

Kawamuro, T. et al. (2018). "MAXI/GSC detection of a probable new X-ray transient MAXI J1820+070." In: *The Astronomer's Telegram* 11399, p. 1.

Koljonen, K. I. I. and T. J. Maccarone (2017). "Gemini/GNIRS infrared spectroscopy of the Wolf-Rayet stellar wind in Cygnus X-3." In: *MNRAS* 472.2, pp. 2181–2195.

Loh, A. et al. (2016). "High-energy gamma-ray observations of the accreting black hole V404 Cygni during its 2015 June outburst." In: *MNRAS* 462.1, pp. L111–L115.

Longair, M. S. (1981). *High energy astrophysics*. Cambridge University Press.

Lorenz, E. and R. Wagner (2012). "Very-high energy gamma-ray astronomy. A 23-year success story in high-energy astroparticle physics." In: *European Physical Journal H* 37.3, pp. 459–513.

Lyne, A. G. et al. (2015). "The binary nature of PSR J2032+4127." In: *MNRAS* 451.1, pp. 581–587.

MAGIC Collaboration et al. (2017). "Search for very high-energy gamma-ray emission from the microquasar Cygnus X-1 with the MAGIC telescopes." In: *MNRAS* 472, pp. 3474–3485.

MAGIC Collaboration et al. (2018). "Constraints on particle acceleration in SS433/W50 from MAGIC and H.E.S.S. observations." In: *A&A* 612, A14, A14.

Markoff, S., H. Falcke, and R. Fender (2001). "A jet model for the broadband spectrum of XTE J1118+480. Synchrotron emission from radio to X-rays in the Low/Hard spectral state." In: *A&A* 372, pp. L25–L28.

Martí, J., J. M. Paredes, and M. Peracaula (2001). "Development of a two-sided relativistic jet in Cygnus X-3." In: *A&A* 375, pp. 476–484.

Martí, J., J. M. Paredes, and M. Peracaula (2000). "The Cygnus X-3 Radio Jets at Arcsecond Scales." In: *ApJ* 545.2, pp. 939–944.

Mattox, J. R. et al. (1996). "The Likelihood Analysis of EGRET Data." In: *ApJ* 461, p. 396.

McCollough, M. L., L. Corrales, and M. M. Dunham (2016). "Cygnus X-3: Its Little Friend's Counterpart, the Distance to Cygnus X-3, and Outflows/Jets." In: *ApJ* 830.2, L36, p. L36.

Miller-Jones, J. C. A. et al. (2004). "Time-sequenced Multi-Radio Frequency Observations of Cygnus X-3 in Flare." In: *ApJ* 600, pp. 368–389.

Miller-Jones, J. C. A. et al. (2021). "Cygnus X-1 contains a 21–solar mass black hole—Implications for massive star winds." In: *Science* 371.6533, pp. 1046–1049.

Mioduszewski, A. J. et al. (2001). "A One-sided Highly Relativistic Jet from Cygnus X-3." In: *ApJ* 553, pp. 766–775.

Mirabel, I. F. and L. F. Rodríguez (1999). "Sources of Relativistic Jets in the Galaxy." In: *ARA&A* 37, pp. 409–443.

Moe, M. and R. Di Stefano (2017). "Mind Your Ps and Qs: The Interrelation between Period (P) and Mass-ratio (Q) Distributions of Binary Stars." In: *ApJS* 230.2, 15, p. 15.

Moffat, A. F. J. (2008). "Observational overview of clumping in hot stellar winds." In: *Clumping in Hot-Star Winds*. Ed. by W.-R. Hamann, A. Feldmeier, and L. M. Oskinova, p. 17.

Moldón, J., M. Ribó, and J. M. Paredes (2012). "Periodic morphological changes in the radio structure of the gamma-ray binary LS 5039." In: *A&A* 548, A103, A103.

Molina, E. and V. Bosch-Ramon (2018). "Nonthermal emission from high-mass microquasar jets affected by orbital motion." In: *A&A* 618, A146, A146.

Molina, E. and V. Bosch-Ramon (2020). "A dynamical and radiation semi-analytical model of pulsar-star colliding winds along the orbit: Application to LS 5039." In: *A&A* 641, A84, A84.

Molina, E., S. del Palacio, and V. Bosch-Ramon (2019). "A model for high-mass microquasar jets under the influence of a strong stellar wind." In: *A&A* 629, A129, A129.

Moritani, Y. et al. (2015). "Probing the Nature of the TeV γ-Ray Binary HESS J0632+057 by Monitoring Be Disk Variability." In: *ApJ* 804.2, L32, p. L32.

Muijres, L. E. et al. (2011). "Predictions of the effect of clumping on the wind properties of O-type stars." In: *A&A* 526, A32, A32.

Muijres, L. E. et al. (2012). "Predictions for mass-loss rates and terminal wind velocities of massive O-type stars." In: *A&A* 537, A37, A37.

Nagase, F. (1989). "Accretion-powered X-ray pulsars." In: *PASJ* 41, p. 1.

Negueruela, I. et al. (2011). "Astrophysical Parameters of LS 2883 and Implications for the PSR B1259-63 Gamma-ray Binary." In: *ApJ* 732.1, L11, p. L11.

Okazaki, A. T. et al. (2011). "Hydrodynamic Interaction between the Be Star and the Pulsar in the TeV Binary PSR B1259-63/LS 2883." In: *PASJ* 63, p. 893.

Owocki, S. P. and D. H. Cohen (2006). "The Effect of Porosity on X-Ray Emission-Line Profiles from Hot-Star Winds." In: *ApJ* 648.1, pp. 565–571.

Pacholczyk, A. G. (1970). *Radio astrophysics. Nonthermal processes in galactic and extragalactic sources*. W. H. Freeman & Company.

Paczyński, B. (1971). "Evolutionary Processes in Close Binary Systems." In: *ARA&A* 9, p. 183.

Paredes, J. M. et al. (2013). "Binaries with the eyes of CTA." In: *Astroparticle Physics* 43, pp. 301–316.

Park, N. et al. (2015). "Performance of the VERITAS experiment." In: *34th International Cosmic Ray Conference (ICRC2015)*. Vol. 34. International Cosmic Ray Conference, p. 771.

Parsignault, D. R. et al. (1976). "On the stability of the period of Cygnus X-3." In: *ApJ* 209, pp. L73–L75.

Perucho, M. and V. Bosch-Ramon (2008). "On the interaction of microquasar jets with stellar winds." In: *A&A* 482, pp. 917–927.

Perucho, M. and V. Bosch-Ramon (2012). "3D simulations of microquasar jets in clumpy stellar winds." In: *A&A* 539, A57, A57.

Perucho, M., V. Bosch-Ramon, and D. Khangulyan (2010). "3D simulations of wind-jet interaction in massive X-ray binaries." In: *A&A* 512, L4, p. L4.

Piano, G. et al. (2017). "High-energy Gamma-Ray Activity from V404 Cygni Detected by AGILE during the 2015 June Outburst." In: *ApJ* 839.2, 84, p. 84.

Porter, J. M. and T. Rivinius (2003). "Classical Be Stars." In: *PASP* 115.812, pp. 1153–1170.

Reig, P. (2011). "Be/X-ray binaries." In: *Ap&SS* 332.1, pp. 1–29.

Remillard, R. A. and J. E. McClintock (2006). "X-Ray Properties of Black-Hole Binaries." In: *ARA&A* 44.1, pp. 49–92.

Rodi, J. et al. (2021). "A Broadband View on Microquasar MAXI J1820+070 during the 2018 Outburst." In: *ApJ* 910.1, 21, p. 21.

Roldan, P. and P. Lecoq (2021). "Quality control and preparation of the PWO crystals for the electromagnetic calorimeter of CMS." In:

Rolke, W. A., A. M. López, and J. Conrad (2005). "Limits and confidence intervals in the presence of nuisance parameters." In: *Nuclear Instruments and Methods in Physics Research A* 551.2-3, pp. 493–503.

Romero, G. E. et al. (2017). "Relativistic Jets in Active Galactic Nuclei and Microquasars." In: *Space Sci. Rev.* 207.1-4, pp. 5–61.

Roques, J.-P. and E. Jourdain (2019). "On the High-energy Emissions of Compact Objects Observed with INTEGRAL SPI: Event Selection Impact on Source Spectra and Scientific Results for the Bright Sources Crab Nebula, GS 2023+338 and MAXI J1820+070." In: *ApJ* 870.2, 92, p. 92.

Sánchez-Sierras, J. and T. Muñoz-Darias (2020). "Near-infrared emission lines trace the state-independent accretion disc wind of the black hole transient MAXI J1820+070." In: *A&A* 640, L3, p. L3.

Shakura, N. I. and R. A. Sunyaev (1973). "Black holes in binary systems. Observational appearance." In: *A&A* 500, pp. 33–51.

Shidatsu, M. et al. (2019). "X-Ray and Optical Monitoring of State Transitions in MAXI J1820+070." In: *ApJ* 874.2, 183, p. 183.

Stirling, A. M. et al. (2001). "A relativistic jet from Cygnus X-1 in the low/hard X-ray state." In: *MNRAS* 327, pp. 1273–1278.

Takahashi, T. et al. (2009). "Study of the Spectral and Temporal Characteristics of X-Ray Emission of the Gamma-Ray Binary LS 5039 with Suzaku." In: *ApJ* 697.1, pp. 592–600.

Tavani, M. et al. (2009a). "Extreme particle acceleration in the microquasar CygnusX-3." In: *Nature* 462.7273, pp. 620–623.

Tavani, M. et al. (2009b). "Extreme particle acceleration in the microquasar CygnusX-3." In: *Nature* 462.7273, pp. 620–623.

Tetarenko, A. J. et al. (2021). "Measuring fundamental jet properties with multi-wavelength fast timing of the black hole X-ray binary MAXI J1820+070." In: *MNRAS*.

Torres, M. A. P. et al. (2019). "Dynamical Confirmation of a Black Hole in MAXI J1820+070." In: *ApJ* 882.2, L21, p. L21.

Torres, M. A. P. et al. (2020). "The Binary Mass Ratio in the Black Hole Transient MAXI J1820+070." In: *ApJ* 893.2, L37, p. L37.

Tucker, M. A. et al. (2018). "ASASSN-18ey: The Rise of a New Black Hole X-Ray Binary." In: *ApJL* 867, L9, p. L9.

Usov, V. V. (1992). "Stellar Wind Collision and X-Ray Generation in Massive Binaries." In: *ApJ* 389, p. 635.

Veledina, A. et al. (2019). "Evolving optical polarisation of the black hole X-ray binary MAXI J1820+070." In: *A&A* 623, A75, A75.

Watson, A. A. (2011). "The discovery of Cherenkov radiation and its use in the detection of extensive air showers." In: *Nuclear Physics B Proceedings Supplements* 212, pp. 13–19.

Weekes, T. C. et al. (2002). “VERITAS: the Very Energetic Radiation Imaging Telescope Array System.” In: *Astroparticle Physics* 17.2, pp. 221–243.

Wilks, S. S. (1938). “The Large-Sample Distribution of the Likelihood Ratio for Testing Composite Hypotheses.” In: *Ann. Math. Statist.* 9.1, pp. 60–62.

Winkler, C. et al. (2003). “The INTEGRAL mission.” In: *A&A* 411, pp. L1–L6.

Yoon, D. and S. Heinz (2015). “Global Simulations of the Interaction of Microquasar Jets with a Stellar Wind in High-mass X-ray Binaries.” In: *ApJ* 801, 55, p. 55.

Yoon, D., A. A. Zdziarski, and S. Heinz (2016). “Formation of recollimation shocks in jets of high-mass X-ray binaries.” In: *MNRAS* 456, pp. 3638–3644.

Zabalza, V. (2011). “The keV-TeV connection in gamma-ray binaries.” PhD thesis. Departament d’Astronomia i Meteorologia, Institut de Ciències del Cosmos (ICC), Universitat de Barcelona (IEEC-UB).

Zabalza, V. et al. (2013). “Unraveling the high-energy emission components of gamma-ray binaries.” In: *A&A* 551, A17, A17.

Zanin, R. et al. (2016). “Gamma rays detected from Cygnus X-1 with likely jet origin.” In: *A&A* 596, A55, A55.

Zdziarski, A. A., J. Mikolajewska, and K. Belczynski (2013). “Cyg X-3: a low-mass black hole or a neutron star.” In: *MNRAS* 429, pp. L104–L108.

Zdziarski, A. A. et al. (2018). “A comprehensive study of high-energy gamma-ray and radio emission from Cyg X-3.” In: *MNRAS* 479, pp. 4399–4415.

Zdziarski, A. A. et al. (2021). “Accretion Geometry in the Hard State of the Black Hole X-Ray Binary MAXI J1820+070.” In: *ApJ* 909.1, L9, p. L9.

The bibliography above refers to citations in Chapter 1, the individual introductions of Chapters 2, 3 and 4, Chapters 5 and 6, and Appendix a. Citations of the individual publications are listed within the corresponding manuscript.

COLOPHON

The MAGIC Collaboration is acknowledged for allowing the use of proprietary observational data. MAGIC results presented in this thesis have not undergone the internal review procedure of MAGIC publications.

This document was typeset using the typographical look-and-feel `classicthesis` developed by André Miede and Ivo Pletikosić. The style was inspired by Robert Bringhurst's seminal book on typography *The Elements of Typographic Style*. The `classicthesis` template is available for both LaTeX and LyX at `https://bitbucket.org/amiede/classicthesis/`.

Final Version as of June 28, 2021 (classicthesis v4.6).

ACKNOWLEDGMENT OF FUNDING

The author acknowledges financial support from the Spanish Ministerio de Ciencia e Innovación (MICINN) through grant BES-2016-076342. This thesis is also supported by MICINN under grants FPA2015-69210-C6-2-R, AYA2016-76012-C3-1-P, FPA2017-82729-C6-2-R, PID2019-105510GB-C31 annd PID2019-104114RB-C33, with partial support by the European Regional Development Fund (ERDF/FEDER); and by the Generalitat de Catalunya through grants 2014SGR86 and 2017SGR643. The author also acknowledges support by the Spanish Unidad de Excelencia "María de Maeztu" MDM-2014-0369 and CEX2019-000918-M.